The Role of Phase Combinations on the Corrosion and Passivity Behaviour of High Strength Steels

Master Thesis

The Role of Phase Combinations on the Corrosion and Passivity Behaviour of High Strength Steels

Master Thesis

Thesis

submitted to the

Delft University of Technology

in partial fulfillment of the requirements for the degree of

Master of Science in Materials Science and Engineering

by

Can Özkan

September 2020, Delft



Keywords: corrosion, passivity, steel, microstructure, phase

Supervisors: Dr. Yaiza Gonzalez-Garcia

Aytaç Yılmaz

Co-readers: Dr. Jilt Sietsma

Dr. Peyman Taheri

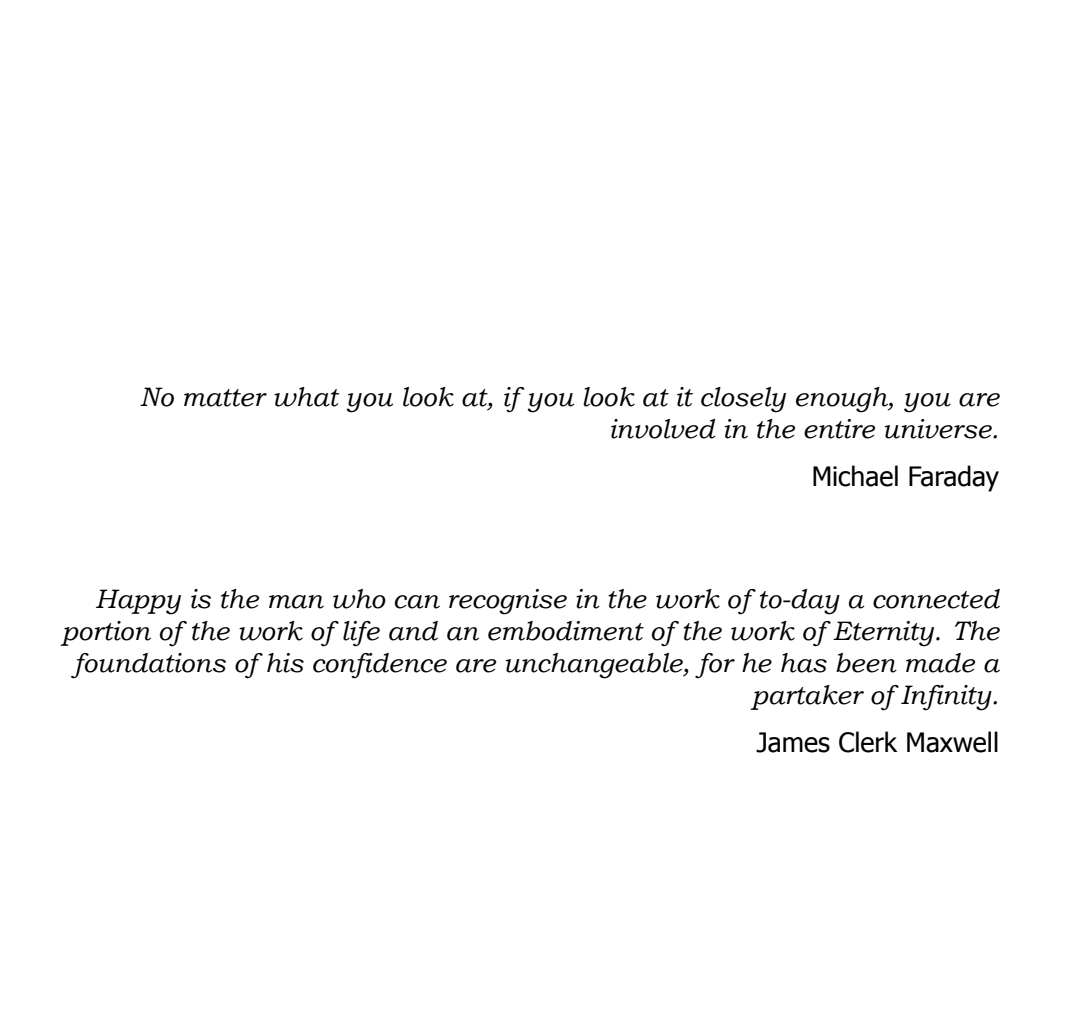
Dr. Jie Zhou

Can Özkan: The Role of Phase Combinations on the Corrosion and Passivity Behaviour of High Strength Steels (2020)

This work is licensed under a Creative Commons Attribution 4.0 International License. To view a copy of this license, visit

http://creativecommons.org/licenses/by/4.0/.

An electronic version of this dissertation is available at http://repository.tudelft.nl/.



Acknowledgements

I would like to express my deep gratitude to Prof. Dr. Yaiza Gonzalez-Garcia for her patient guidance and constant support during the trying times of COVID-19. Your support and adaptability made the experience an adventure rather than a calamity, thank you.

I would also like to thank soon to be Dr. Aytaç Yılmaz, for his day-to-day guidance and continuous feedback. Your assistance was invaluable.

I would also like to extend my gratitude to Prof. Dr. Maria J. Santofimia-Navarro for her assistance in designing the heat treatments of the microstructures, Konstantina Traka for her insights about the corrosion simulations, and to Sander van Asperen and Agnieszka Kooijman Banaszak for their unwavering support in the mechanical and electrochemical laboratories.

Finally, I would like to thank my parents for their constant support throughout my studies. I wouldn't be here without you.

Abstract

Literature reports a great deal of contradictory results concerning the effect of microstructure on the corrosion and passivity behaviour of advanced high strength steels. The difficulty in identifying the controlling cause of corrosion results from the inability of disentangling the coupled effects of individual microstructural features in a scientifically rigorous manner, thereby attributing the core behaviour to the wrong sources.

The aim of this thesis is to isolate and identify the effect of phases on the electrochemical response of high strength steels. To this end, a combined computational and experimental approach is taken. This work starts by analysing the connection between heat treatment, microstructure, and the resulting corrosion properties. After clarification of this interdependence, a finite element electrochemical model illuminates the corrosion behaviour of idealised two phase ferrite-martensite and ferrite-pearlite systems for different phase volume fraction combinations. The results from the simulations quide the microstructure creation for electrochemical experiments, where employed heat treatments result in ferrite-martensite and ferrite-pearlite microstructures with similar ferrite volume fractions. Potentiodynamic polarisation and electrochemical impedance spectroscopy (EIS) experiments in 0.1M and $0.01MH_2SO_4$ solutions; potentiostatic polarisation, EIS and Mott-Schottky analysis in 0.1M NaOH solutions reveal the corrosion response and passive film barrier properties of the microstructures. Results demonstrate a clear phase dependency for both active and passive conditions, and are further discussed in light of microstructural features of secondary martensite and pearlite phases.

Nomenclature

HSLAHigh strength low alloy Ferrite-martensite FMFPFerrite-pearlite Gibbs free energy [I/mol] G Н Enthalpy []/mol] TTemperature [K] Entropy [J/molK] S number of elementary charges n F Faraday's constant = 96,485 [C/mol] \mathcal{C} Coulomb, where $1C = 6.24x10^{18}$ electrons Ampere [C/s] Α Ε Electromotive force []/mol] R Gas constant = 8.3145 [I/molK]Reduced bulk molecule concentration [mol] C_{Red} Oxidised bulk molecule concentration [mol] C_{Ox} Reaction rate $\lceil mol/m^2s \rceil$ ν Current density $\lceil A/m^2 \rceil$ j Equilibrium potential [V] E_{ea} Exchange current density $\lceil A/m^2 \rceil$ j_0 Overpotential [V] η Anodic charge transfer coefficient α_a Cathodic charge transfer coefficient α_c Molar Mass [kg/mol] а Material density $[kg/m^3]$ ρ

xii Abstract

| DP | Dual phase |
|------------|--|
| TRIP | Transformation induced plasticity |
| Q&P | Quench and partitioning |
| Q&T | Quench and tempering |
| PDE | Partial differential equations |
| N_i | <i>i</i> th species ionic flux density $[mol/m^2s]$ |
| D_i | i th species diffusion coefficient $[m^2/s]$ |
| ∇ | Gradient operator |
| c_i | i th species concentration $[mol/m^3]$ |
| z_i | ith species number of electrons involved in the reaction per ion |
| φ | Electrostatic potential [V] |
| $ec{v}$ | Solvent velocity $[m/s]$ |
| R_i | <i>i</i> th species chemical reaction rate $[mol/m^3s]$ |
| i_l | Electrode-electrolyte surface current $[A/m^2]$ |
| σ_l | Electrolyte conductivity [S/m] |
| OCP | Open circuit potential |
| EIS | Electrochemical Impedance Spectroscopy |
| AC | Alternating current |
| BCC | Body-centred cubic |
| FCC | Face-centred cubic |

Contents

| A | ckno | wledgements | vii |
|----|-------|--|------|
| Α1 | bstra | ct | ix |
| N | omer | ıclature | хi |
| Li | st of | Figures | хv |
| Li | st of | Tables | xix |
| 1 | Bac | kground | 1 |
| | | Corrosion | . 1 |
| | 1.2 | Corrosion Electrochemistry | . 1 |
| | | 1.2.1 Thermodynamics | |
| | | 1.2.2 Kinetics | . 4 |
| | 1.3 | Main Types of Corrosion | . 6 |
| | 1.4 | High Strength Steels - Significance of Metallurgy and Process- | |
| | | ing | . 7 |
| | | 1.4.1 Heat Treatment and Thermomechanical Processes | |
| | | 1.4.2 Microstructure | |
| | 1.5 | Effect of Microstructure on Corrosion of High Strength Steels | |
| | | 1.5.1 Grain Structure | |
| | | 1.5.2 Phase Constituents | |
| | | 1.5.3 Passivation and Oxide Layer Properties | |
| | | 1.5.4 Chemical Composition | |
| | | 1.5.5 Evaluation and Comparison | |
| | 1.6 | Research Approach and Thesis Focus | |
| 2 | | lelling | 35 |
| | | Modelling Approach | |
| | | Theory | |
| | 2.3 | Implementation | . 38 |
| 3 | _ | erimental Procedure | 45 |
| | 3.1 | Microstructure Characterisation | |
| | | 3.1.1 Material | |
| | | 3.1.2 Dilatometry | |
| | | 3.1.3 Sample Preparation | |
| | | 3.1.4 Investigation of the Microstructure | . 48 |

xiv Contents

| | 3.2 | 3.2.1 3.2.2 3.2.3 | Sample Preparation | . 4 | 18 19 19 |
|---|------|-------------------------|---|-----|----------------|
| 4 | Res | ults ar | nd Discussion | 5 | 53 |
| | 4.1 | | ation | | 53 |
| | | 4.1.1 | The Behaviour of Ferrite-Martensite and Ferrite-Pearlite | | |
| | | 412 | Microstructure Phase Volume Fraction Relationship | | |
| | 4.2 | | imental | | |
| | | | Microstructure Characterisation | | |
| | | | Electrochemical Measurements: Active Behaviour | | |
| | | | Electrochemical Measurements: Passive Behaviour Phase Dependency of Corrosion and Passivity | | |
| 5 | Con | | ns and Recommendations | | 31 |
| • | | | usions | _ | _ |
| | | | nmendations | | |
| | Refe | rences | 8 | . 8 | 35 |
| A | Pola | risati | on Data | 9 | 3 |
| В | Mod | lel Inp | out Parameters | 9 | 7 |
| C | Sim | ulated | Potentiodynamic Polarisation Plots | 9 | 9 |
| | C.1 | | e-Martensite Microstructure Simulated | | |
| | 0.0 | | tiodynamic Polarisation Plots | . 1 | 00 |
| | C.2 | | e-Pearlite Microstructure Simulated tiodynamic Polarisation Plots | 1 | Λ 5 |
| | | TOTELL | uouynamici olai isalloli fiolo | . 1 | σ |

List of Figures

| 1.1 | Double layer formed at the electrode-electrolyte interface. | 2 |
|------|--|-----|
| 1.2 | Pourbaix diagram for $H_2O - Fe$ system. | 4 |
| 1.3 | Factors controlling the galvanic corrosion. | 6 |
| 1.4 | A model iron-carbon phase diagram displaying the breadth of ther- | |
| | modynamically stable phases for different compositions and temper- | |
| | atures | 8 |
| 1.5 | Illustration of variety of microstructures that can be obtained by | |
| | isothermal transformation of austenite. | 9 |
| 1.6 | Steel microstructures produced as a result of different heat treatments. | 11 |
| 1.7 | Three dimensional crystallographic orientation models of {100}, {101} | |
| | and {111} | 15 |
| 1.8 | Electrochemical behaviour of ferrite-martensite dual phase steel in | |
| | 0.1M sulphuric acid solution. | 19 |
| 1.9 | Schematic representing the microstructure of Q&T and Q&P structures. | 21 |
| | Dual phase steel oxide structure schematic. | 23 |
| | Schematic representation of corrosion mechanism and oxide forma- | |
| | tion of pearlitic and bainitic steels. | 26 |
| 1 12 | Grain orientation dependence of oxide composition. | 27 |
| | Anisotropic growth mechanism of Fe/Fe_3O_4 interface. | 28 |
| | A collection of corrosion potential and corrosion current data acquired | |
| 1.1. | from the polarisation experiments carried out in the 3.5 wt.% NaCl | |
| | environment | 32 |
| | CHVIIOIIIICIC | 32 |
| 2.1 | 2D model geometry and example simulation for 50% ferrite 50% | |
| | martensite potentiodynamic polarisation. | 39 |
| 2.2 | Example free corrosion simulations for OCP determination. | 40 |
| 2.3 | A 3D simulation with hexagonal geometry and periodic boundaries | . • |
| | with 100 μm grains | 41 |
| 2.4 | A 3D simulation with hexagonal geometry and periodic boundaries | |
| | with $10 \ \mu m$ grains. | 41 |
| 2.5 | A 3D simulation with hexagonal geometry and non-periodic insulated | |
| 2.5 | boundaries with $10 \ \mu m$ grains | 41 |
| 2.6 | Geometry and boundary conditions for the 3D simulation set. | 42 |
| 2.0 | decirredly and boundary conditions for the 3D simulation set | 72 |
| 3.1 | Initial microstructure of DP1000 steel after etching it with OPS and | |
| | 2% Nital etchant. | 46 |
| 3.2 | Graphical summary of the employed heat treatments. | 47 |
| 3.3 | An example completed sample ready for electrochemical experiments. | 49 |
| | | |

xvi List of Figures

| 3.4 | Electrochemical cell setup. | 50 |
|------|--|------------|
| 4.1 | Simulated potentiodynamic polarisation curve for the 50% ferrite 50% martensite microstructure. | 54 |
| 4.2 | Simulated potentiodynamic polarisation curve for the 50% ferrite 50% pearlite microstructure. | 54 |
| 4.3 | Simulated corrosion current density values for various volume fractions of ferrite-martensite microstructure. | 55 |
| 4.4 | Simulated corrosion current density values for various volume fractions of ferrite-pearlite microstructure. | 55 |
| 4.5 | The effect of volume fraction on the corrosion current density of simulated ferrite-martensite and ferrite-pearlite microstructures. | 57 |
| 4.6 | Evans diagram that shows the relationship between current and potential for a galvanic interaction between two different structures. | 58 |
| 4.7 | Time and temperature evolution with time for different heat treatment routes. | 61 |
| 4.8 | Dilatometric curves for dual phase ferrite-martensite (FM) and ferrite-pearlite (FP) microstructures. | 62 |
| 4.9 | Optical and SEM images taken from ferrite-martensite and ferrite-pearlite dual phase microstructures. | 63 |
| 4.10 | OCP values of ferrite-martensite (FM) and ferrite-pearlite (FP) microstructures in 0.1M (pH 1.0) and 0.01M (pH 1.9) sulphuric acid environments. | 65 |
| 4.11 | Nyquist (a) and Bode (b) plots of dual phase ferrite-martensite and ferrite-pearlite microstructures obtained with EIS in $0.1M\ H_2SO_4$ (pH 1.0) environment. | 66 |
| 4.12 | Nyquist (a) and Bode (b) plots of dual phase ferrite-martensite and ferrite-pearlite microstructures obtained with EIS in $0.01MH_2SO_4$ (pH 1.9) environment. | 67 |
| 4.13 | Equivalent circuit proposed for modelling the electrochemical response of dual phase ferrite-martensite and ferrite-pearlite microstructures in sulphuric acid environment. | 68 |
| 4.14 | Potentiodynamic polarisation plots of dual phase ferrite-martensite and ferrite-pearlite microstructures in (a) 0.1M (pH 1.0), (b) 0.01M | |
| 4.15 | (pH 1.9) sulphuric acid environments. OCP values of ferrite-martensite (FM) and ferrite-pearlite (FP) microstructures in 0.1M sodium hydroxide (pH 12.6) environment. | 70 72 |
| 4.16 | Twin logarithmic time-current density plots of ferrite-martensite and ferrite-pearlite microstructures during potentiostatic polarisation at 0.2 V in 0.1M NaOH (pH 12.6) environment. | 72 |
| 4.17 | Nyquist (a) and Bode (b) plots of dual phase ferrite-martensite and ferrite-pearlite microstructures obtained with EIS in 0.1M <i>NaOH</i> (pH 12.6) environment. | 74 |
| | 12.0) CHAROLINICHE | <i>,</i> T |

List of Figures xvii

| 4.18 | of dual phase ferrite-martensite and ferrite-pearlite microstructures | |
|------------|---|-----|
| | in alkaline sodium hydroxide environment | 75 |
| 4.19 | Mott–Schottky plots for the passive film formed on dual phase ferrite- | , , |
| | martensite and ferrite-pearlite microstructures in 0.1M (pH 12.6) NaOH | |
| | solutions | 76 |
| 4.20 | Space charge region (SCR) and Helmholtz (HL) double layers at the | |
| | semiconductor-electrolyte interface | 76 |
| C 4 | | |
| C.1 | Simulated potentiodynamic polarisation curve for the 10% ferrite 90% martensite microstructure. | 100 |
| C.2 | Simulated potentiodynamic polarisation curve for the 20% ferrite | 100 |
| C.Z | 80% martensite microstructure | 101 |
| C.3 | Simulated potentiodynamic polarisation curve for the 30% ferrite | 101 |
| C.S | 70% martensite microstructure | 101 |
| C.4 | Simulated potentiodynamic polarisation curve for the 40% ferrite | |
| | 60% martensite microstructure. | 102 |
| C.5 | Simulated potentiodynamic polarisation curve for the 50% ferrite | |
| | 50% martensite microstructure | 102 |
| C.6 | Simulated potentiodynamic polarisation curve for the 60% ferrite | |
| | 40% martensite microstructure | 103 |
| C.7 | Simulated potentiodynamic polarisation curve for the 70% ferrite | |
| | 30% martensite microstructure | 103 |
| C.8 | Simulated potentiodynamic polarisation curve for the 80% ferrite | |
| C O | 20% martensite microstructure. | 104 |
| C.9 | Simulated potentiodynamic polarisation curve for the 90% ferrite 10% martensite microstructure. | 104 |
| C 10 | Simulated potentiodynamic polarisation curve for the 10% ferrite | 104 |
| C.10 | 90% pearlite microstructure | 105 |
| C.11 | Simulated potentiodynamic polarisation curve for the 20% ferrite | 103 |
| 0.11 | 80% pearlite microstructure | 106 |
| C.12 | Simulated potentiodynamic polarisation curve for the 30% ferrite | |
| | 70% pearlite microstructure | 106 |
| C.13 | Simulated potentiodynamic polarisation curve for the 40% ferrite | |
| | 60% pearlite microstructure | 107 |
| C.14 | Simulated potentiodynamic polarisation curve for the 50% ferrite | |
| | 50% pearlite microstructure | 107 |
| C.15 | Simulated potentiodynamic polarisation curve for the 60% ferrite | |
| 0.46 | 40% pearlite microstructure. | 108 |
| C.16 | Simulated potentiodynamic polarisation curve for the 70% ferrite | 100 |
| C 17 | 30% pearlite microstructure. | 108 |
| C.1/ | Simulated potentiodynamic polarisation curve for the 80% ferrite 20% pearlite microstructure. | 109 |
| C 18 | Simulated potentiodynamic polarisation curve for the 90% ferrite | 109 |
| C.10 | 10% pearlite microstructure | 100 |
| | 10 /0 pearlice illicrostructure. | 103 |

List of Tables

| 2.1 | Provisional simulation summary for subsequent volume fraction analysis. | 43 |
|-----------------------------------|---|----------|
| 3.1 3.2 | Chemical composition (wt.%) of DP1000 steel samples. Critical temperatures for the subsequent heat treatments of DP1000 | 45 |
| J.2 | dual phase steel. | 46 |
| 4.1 | Vickers microhardness measurements of individual phase constituents for ferrite-martensite and ferrite-pearlite microstructures at 0.01 HV scale. | 64 |
| 4.2 | The fitting values of the equivalent circuit components for ferrite-martensite (FM) and ferrite-pearlite (FP) microstructures in 0.1M (pH 1.0) sulphuric acid environment. | 69 |
| 4.3 | The fitting values of the equivalent circuit components for ferrite-martensite (FM) and ferrite-pearlite (FP) microstructures in 0.01M (pH 1.9) sulphuric acid environment. | 69 |
| 4.44.5 | Corrosion current density (j_{corr}) and corrosion potential (E_{corr}) values of ferrite-martensite (FM) and ferrite-pearlite (FP) microstructures calculated from the potentiodynamic polarisation experiments. | 71 |
| 4.3 | The fitting values of the equivalent circuit components for ferrite-martensite (FM) and ferrite-pearlite (FP) microstructures in 0.1M (pH 12.6) sodium hydroxide environment. | 75 |
| A.1 | Polarisation data collected from the literature | 94 |
| B.1 B.2 | Input parameters for the ferrite-martensite microstructure simulation. Input parameters for the ferrite-pearlite microstructure simulation. | 98 98 |

1

Background

1.1. Corrosion

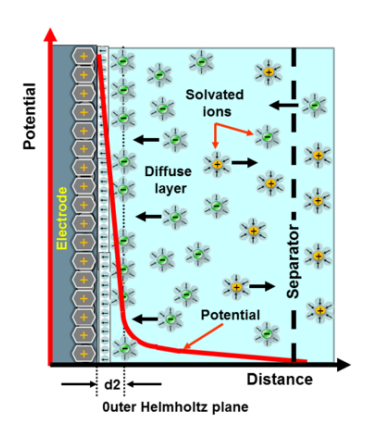
The advent of ever-new technological products such as Tesla's Cybertruck and SpaceX's Starship require new material solutions, as seen by the new custom-developed stainless steel alloy to be used in both structures. While mechanical properties are often under the spotlight for such projects, corrosion behaviour is often neglected or poorly understood.

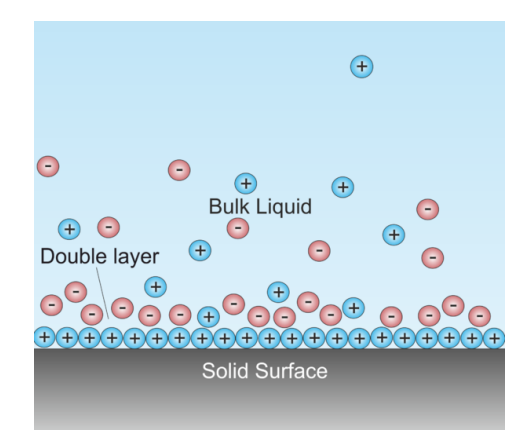
Corrosion is the reversal of metals to more thermodynamically stable states such as oxides, hydroxides, salts or carbonates [1]. The interaction of the metal with the surrounding environment is a relatively slow process that causes metals to degrade. It is the underlying reason of highly important and expensive problems - corrosion costs the world US2.5\$ trillion or 3.4% of the global GDP [2].

The influence of corrosion on high strength low alloy (HSLA) steels is especially important. Superior mechanical properties offered by HSLA steels are often the result of a multi-phase microstructure resulting from a delicate balance between thermodynamic and kinetic processes [3]. The creation of prescribed microstructures incorporates processes such as altering grain sizes, changing phase fractions, creation of inclusions, modifying dislocation densities, and manipulating crystallographic orientations. The mechanical design of such bespoke microstructures clearly has an effect on the electrochemical properties. In some cases the better mechanical design results in earlier failure by deteriorating the corrosion protection of the material and prevents the alloy from reaching its full potential. For this reason, a focus on corrosion and passivation behaviour for HSLA steels is needed.

1.2. Corrosion Electrochemistry

Electrochemical corrosion requires the presence of an electrolyte and electrodes with different electrochemical potentials. The electrochemical potential is induced as a result of the electrolyte-electrode interface interaction. An electrical double layer is formed at the interface that produces an electrostatic potential. Figure





(a) Potential distribution in a Helmholtz double-layer [4]. (b) Diagram of the electrical double layer [5].

Figure 1.1: Double layer formed at the electrode-electrolyte interface.

1.1 demonstrates this double layer. The properties of the double layer control the corrosion processes.

Due to the potential difference of the electrodes, a cathodic and an anodic area is generated on the electrode surfaces. Anodic areas donate electrons and cathodic areas receive them. Conservation of charge requires electroneutrality. To keep the electroneutrality, two partial electrochemical reactions are needed; for example: dissolution of iron in acidic electrolyte due to the oxidation of iron in the anodic areas coupled with the evolution of hydrogen due to the reduction of protons in the cathodic areas.

$$Fe \to Fe^{2+} + 2e^{-}$$
 (1.1)

$$2H^+ + 2e^- \to H_2$$
 (1.2)

For corroding metal structures, this potential difference may be introduced in different ways. Microstructural features such as second phases, metal impurities, grain boundaries and crystallographic orientation give rise to potential differences at the micrometer scale. Concentration differences of certain species such as oxygen in the electrolyte cause differential aeration, which in turn initiate corrosion even in the same microstructure. In a similar fashion, identical metals exposed to different temperatures at different parts give rise to corrosion. Therefore, understanding the metal that acts as the electrode and its relation with the environment is extremely important.

To identify this relationship, two main features of the corrosion cell must be described, thermodynamics and kinetics. Corrosion is controlled both by the thermodynamics and kinetics of the electrode-electrolyte system. The decrease in Gibbs free energy provides the driving force while the kinetics impact the rate of the reaction.

1.2.1. Thermodynamics

Thermodynamics of the corrosion process determine the theoretical corrosion tendency of metals. In a couple with different electrochemical potentials, metal with the more negative electrochemical potential takes up the role of anode and dissolves.

The underlying reason behind the corrosion phenomena is the decrease in total energy. The total free energy decrease during corrosion, causing a spontaneous reaction.

Change in Gibbs free energy represents maximum useful work under constant temperature and pressure. The decrease in the Gibbs free energy during a corrosion reaction is equal to the electrical work available to the system.

$$G = H + TS \tag{1.3}$$

$$\Delta G = nF\Delta E \tag{1.4}$$

where G is Gibbs free energy, H enthalpy, T temperature, S entropy; and n number of elementary charge involved in reactions, F Faraday's constant, E electromotive force. The difference in the electromotive force series for different materials establishes the propensity for galvanic interactions between them, acting as the driving force for corrosion.

Nernst Equation and Pourbaix Diagrams

The concentration of oxidising and reducing species change during the reaction, and that causes electrochemical potential to also change. For non-standard conditions, Nernst equation (Eq. 1.5) is used to relate the potential of an electrochemical reaction to the standard electrode potential. Nernst equation links electrode potential to the bulk concentration of participant species [6].

$$E = E^0 - \frac{RT}{nF} ln(\frac{C_{Red}}{C_{Ox}})$$
 (1.5)

where R is gas constant, C_{Red} and C_{Ox} reduced and oxidised bulk molecule concentrations respectively.

Electrode potential changes depend on many factors apart from bulk molecule concentrations. Nature of the metal impact electrode potential by whole volts while the chemical nature of the electrolyte has an effect between tenths to whole volts. Surface state of the oxide films, adsorbed gases and mechanical stress also have an effect, albeit more limited [7].

Nernst equation can be utilised to create Pourbaix diagrams that show the stable species in a certain pH and temperature, acting as a map in finding the equilibrium states. It aids in highlighting regions where corrosion exacerbates. It also indicates the dominant cathodic reaction for a certain pH and potential.

Pourbaix diagram for iron is displayed in figure 1.2. Corrosion of iron happens where iron dissolves into iron ions, this is also known as the "active" zone. Zones where iron oxides are thermodynamically stable is known as the "passive" zone,

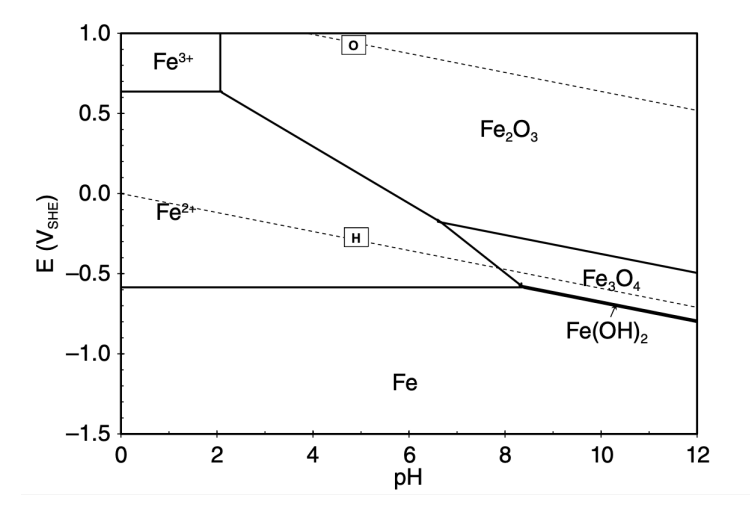


Figure 1.2: Pourbaix diagram for H_2O-Fe system $(T=25^{\circ}C, [Fe^{2+}]=10ppm, Fe[^{3+}]=10^{-6}mol/L, pH_2=pO_2=100kPa)$ [8].

depending on its electronic and ionic conductivity the oxide layer decreases the corrosion rate. In the zones where iron element is the thermodynamically stable form, iron is immune from corrosion.

1.2.2. Kinetics

Thermodynamics do not give information about the corrosion rate. For this, the kinetics of electrochemical reactions must be analysed in light of Faraday's law.

Faraday's law (Eq. 1.6) defines the relationship between the current and the amount of product formed, the passage of 96,485C causes one equivalent of reaction [6].

$$\nu = \frac{j}{nF} \tag{1.6}$$

where ν is the reaction rate of a involved species, j current density, n number of elementary charge(electrons) involved in the process and F Faraday's constant. The amount of material produced at or extracted from an an electrode is directly related to the amount of charge involved in the process, and hence it is directly related to the current passing through the system.

Butler-Volmer Model of Electrode Kinetics

In general, for an electrochemical reaction of $O + ne \rightleftharpoons R$, where dissolved oxidised species O is reduced into R, the rates of processes are governed by the mass transfer, electron transfer at the electrode surface, chemical reaction rate that precedes or follows the electron transfer step, and other surface reactions such as adsorption [6].

In the case of low current and adequate electrolyte circulation, mass transport is not the governing factor in determining the reaction rate. Concentration of ions at the surface of the electrode is the same as in the bulk electrolyte. Instead, interfacial reaction dynamics control the overall process.

Electrode immersed in an electrolyte experiences charge transfer at the interface until the electrochemical potentials on both side of the interface are equal. At the equilibrium potential E_{eq} , oxidation and reduction reactions balance each other out, resulting in zero net current. In that moment, anodic current is balanced by the cathodic current, and their difference give the net current density j.

$$j = |j_{anodic}| - |j_{cathodic}| = 0 (1.7)$$

When the net current is zero, the current that flows across the interface as anodic or cathodic current is the exchange current density j_0 . Exchange current density is an extremely important parameter that controls the rate of the corrosion reactions.

$$j_0 = |j_{anodic}| = |j_{cathodic}| \tag{1.8}$$

However, determination of the exchange current density is a problem since it is an intrinsic parameter of the system. To solve this issue, an external potential can be used to probe the electrochemical system.

The electrochemical cell can be polarised by applying external potential to induce some net current in the system. The difference between the applied potential E and the equilibrium potential E_{eq} is known as the overpotential η .

$$\eta = E - E_{eq} \tag{1.9}$$

Electrochemical polarisation allows controlling the energy of electrons and hence generates a cathodic or anodic net current. Modelling the relationship between overpotential and induced current reveals the electrode behaviour and permits discovery of the exchange current, which is normally impossible to measure experimentally.

Overpotential-current relationship is used to derive a mathematical model from mixed potential theory. The result is the famous Butler-Volmer formulation of the electrode kinetics.

$$j = j_0 \left\{ e^{\frac{\alpha_\alpha n F \eta}{RT}} - e^{-\frac{\alpha_C n F \eta}{RT}} \right\}$$
 (1.10)

where α_a and α_c are anodic and cathodic charge transfer coefficients.

Butler-Volmer relationship is one of the most important and fundamental relationships in electrode kinetics. It plays an important role in the corrosion electrochemistry by quantifying the behaviour of the electrode for unimolecular electrochemical reactions. The analysed exchange current density corresponds to the corrosion current density, which can be related to the physical corrosion rate by Faraday's law:

6 1. Background

$$r = \frac{aj_0}{\rho nF} \tag{1.11}$$

where a is molar mass and ρ is the material density.

1.3. Main Types of Corrosion

Complex nature of corrosion results in different types of corrosion processes. The most common encountered forms are succintly explained in this section.

Galvanic Corrosion

A galvanic cell is a cell where reactions occur spontaneously at two electrodes when they are connected by a conductor [6]. Dissimilar metals with different electrochemical potentials act as galvanic cells and the more anodic one corrodes when coupled together. The potential difference between the two drives preferential corrosion of one or the other. This type of preferential corrosion is known as galvanic corrosion. Factors controlling the galvanic corrosion is shown in figure 1.3.

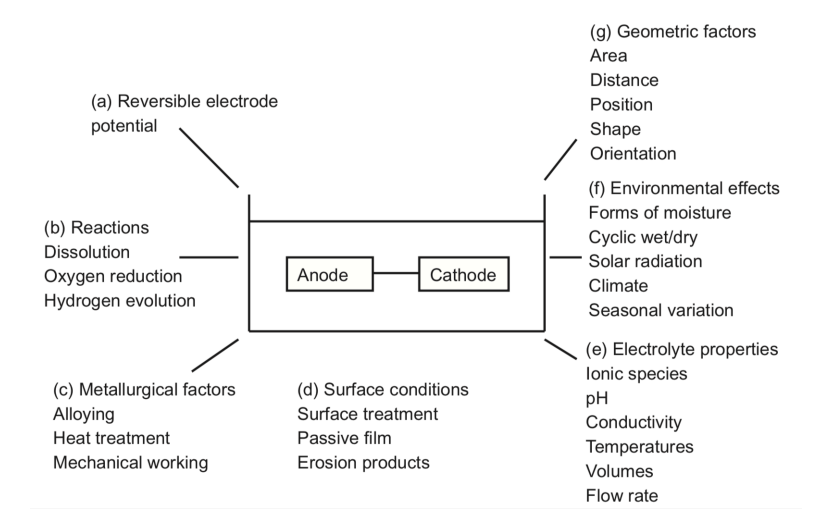


Figure 1.3: Factors controlling the galvanic corrosion [1].

Microgalvanic corrosion is important for multi-phase microstructures and dual phase steels. This is mentioned in a more detailed manner in section 1.5.

Uniform Corrosion

Uniform corrosion is one of the most common types of corrosion which occurs with the equal distribution of anode and cathode zones at the surface. Corrosion occurs more or less evenly, or rather uniformly, across the surface of the metal. It occurs in compositionally uniform metals like cast irons and steels and results in an even surface depletion, as seen in atmospheric corrosion of many metals. Unlike galvanic

corrosion, there are no fixed anodic and cathodic zones. This lack of preferential dissolution makes other features such as local microstructure control the corrosion rate more significantly.

Crevice Corrosion

Crevice corrosion occurs when an aggressive electrolyte penetrates into a narrow crevice. The crevice leads to a separation of anodic and cathodic area due to the concentration differences. Concentration difference of dissolved ions in the crevice causes anodic and cathodic regions to form and initiate corrosion. It is not the focus of this thesis.

Pitting Corrosion

Pits are small holes that go deep into the metal that cause structural failures with minimal overall metal dissolution. Pitting is a form of localised corrosion that can potentially result in catastrophic failures. It is harder to predict and detect than other corrosion forms. Localised attack of pitting corrosion is typical on metals that form corrosion resistant passive layers. The passive film results in a concentration difference of dissolved ions between the inner and outer parts of the pit similar to the case of crevice corrosion, and allocate anodic and cathodic zones in and around the pit. Although a really important type of corrosion for commercial alloys like stainless steels, pitting is not the focus of this thesis since low carbon steels tend to corrode more uniformly rather than develop critical pits.

1.4. High Strength Steels - Significance of Metallurgy and Processing

Versatility offered by the different properties of allotropic forms of iron - austenite and ferrite - is one of the most remarkable features of steels, and the underlying reason why steel is such a fundamental engineering material. An important consequence of this allotropy is the exceptional difference of carbon diffusivities between two forms of steel, resulting in partitioning of the carbon to where it is more soluble and enabling the formation of structures with different mechanical and chemical properties [9].

The variations arise from three thermodynamically stable phases: ferrite, austenite and (metastable) cementite. The breadth of the possible thermodynamically stable phases of iron-carbon system is presented in figure 1.4. Even in such a relatively simple binary alloy system, the abundance of phases allow development of a wide range of structures. The thermodynamics of the plain iron-carbon system is influenced further by the addition of alloying elements such as manganese, nickel and chromium.

The complexity is increased to a greater extent by the kinetic processes caused by thermomechanical treatments such as different cooling rates and isothermal annealing of the steel samples. The resultant microstructures have varying phase constituents (pearlite, martensite, bainite etc.), morphologies and volume fractions.

Nucleation and grain growth of these various phases are controlled not only

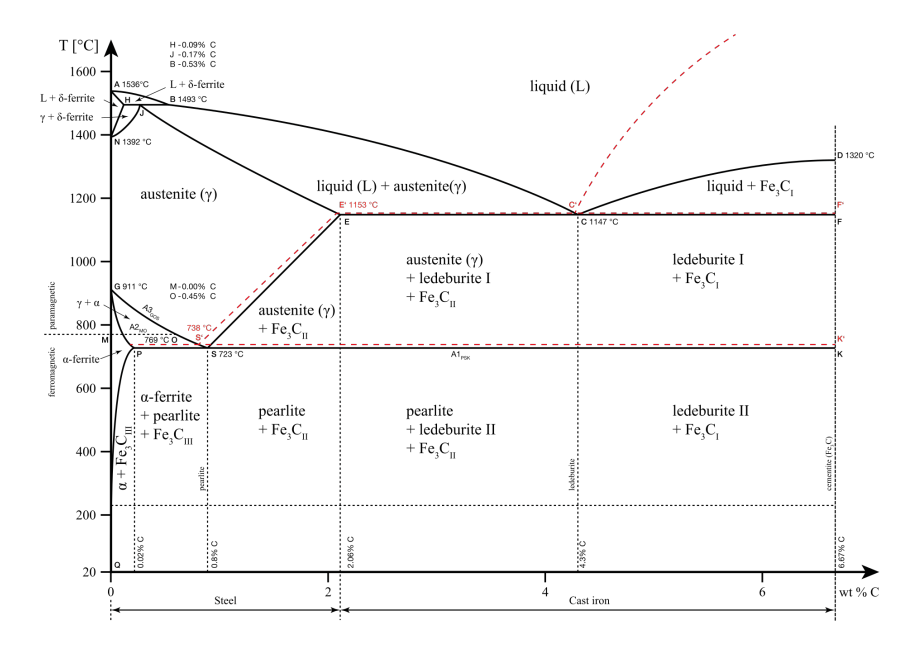


Figure 1.4: A model iron-carbon phase diagram displaying the breadth of thermodynamically stable phases for different compositions and temperatures [10].

by the individual phase and morphology but also by additional alloying elements. Precipitates and dispersoids control grain size by mechanisms such as hard impingement of the grain boundaries while overlapping diffusion fields give rise to soft impingement [11].

Meanwhile dislocation density and crystallographic orientation are altered significantly in preceding stages (interaction with precipitates, high strain caused by martensitic transformations, among others) and can be modified further by processes such as cold deformation.

The resulting electrochemical properties of the material is directly affected from the interaction of such microstructural features, which are determined by the thermomechanical treatments. These processes have a direct impact on the corrosion behaviour, and routinely change multiple corrosion impacting parameters (e.g. change in grain size and dislocation density during an annealing treatment) simultaneously in a single heat treatment step. In literature it is seen that the research done is predominantly disorganised, where the whole picture of the microstructure is not supplied to the reader. Technical constraints, for example the lack of heating/cooling rates in the microstructure creation step, prevent the reproducibility of the experiments. Such limitations make the understanding on corrosion phenomenon difficult. For this reason, the production methods and treatment procedures have to be understood sufficiently before analysing the corrosion response of the steel.

1.4.1. Heat Treatment and Thermomechanical Processes

The microstructural possibilities that can be achieved by proper heat treatment of steels enable materials scientists to create bespoke microstructures for desired applications. Besides the importance of chemistry and thermodynamics of the material as shown in the phase diagram in figure 1.4, the nuances in kinetics influence the microstructure significantly. A good example can be seen in figure 1.5, which shows the variety of microstructures that can be formed with isothermal transformations from austenite. Both the phase fractions and properties can be adjusted by careful control of steel chemistry and thermal/mechanical processes.

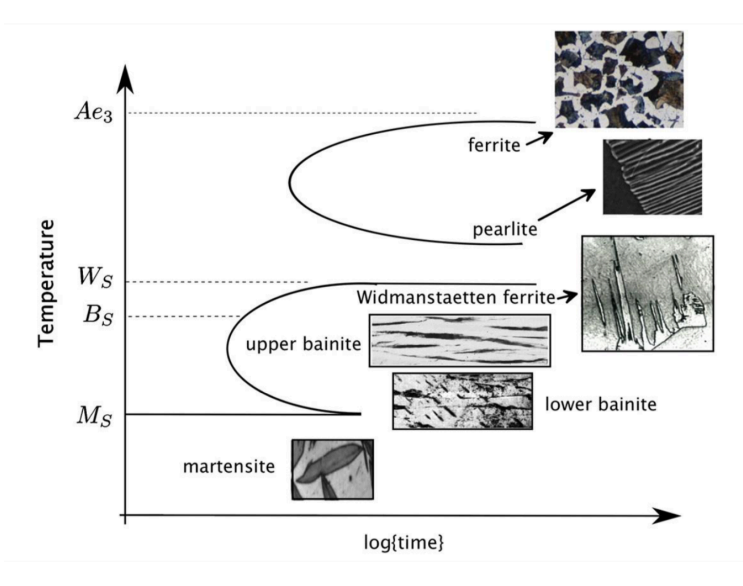


Figure 1.5: Illustration of variety of microstructures that can be obtained by isothermal transformation of austenite [9].

Corrosion resistance is considerably modified by the processing route and the resulting microstructure. In this section, the treatments regularly used in corrosion research is examined to understand the connection between physical processes and corrosion phenomena more clearly.

Normalising

Normalising is heating steel to 100 °C above the Ac_3 temperature and air cooling it through the austenite transformation. Ferrite and austenite grains are refined in the process, resulting in a relatively fine uniform ferrite-pearlite dual phase structure [9].

In a particular study, normalising treatment has formed finer pearlite and ferrite grains than both annealing and hot rolling processes [12]. Heat treatment of normalised samples to the intercritical temperatures is seen to form a microstructure of polyhedral ferrite surrounded by martensite network, also called chain martensite [13].

Annealing

Annealing is austenising the steel at a fairly high temperature and slowly cooling it, resulting in a coarse pearlite structure [9].

Annealing can impact the texture of the steel. It is seen that annealing of the polycrystalline pure iron enables $\{101\}$ and $\{111\}$ grain orientations to dominate the microstructure [14].

Intercritical Annealing

Intercritical annealing is heating the steel between the temperatures of Ae_1 and Ae_3 to give rise to partial austenite transformation [9]. It is usually combined with a rapid cooling procedure like water quenching to transform the microstructure into a martensite-ferrite dual phase structure. An increase in the intercritical annealing temperature leads to a higher volume fraction of martensite in the final structure [15].

Intercritical annealing temperature controls the carbon concentration of austenite [16]. Sarkar et al. [13] recognised no significant change in microstructural morphology of phase constituents for intercritical annealing at 735°C in comparison with intercritical annealing at 775°C. Thus it was hypothesised that microstructures before the intercritical annealing process is most critical in determining the final phase constituent distribution and morphology.

Tempering

Tempering is heating the steel below Ae_1 temperature that results in the modification of the grain sizes, carbide sizes and residual stresses [17]. It allows interstitial carbon to diffuse away from the lattice of metastable structures to form carbides or secondary/tertiary phases.

Tempering low carbon steel for a short time had no significant effect on corrosion response [18], however tempering of martensite resulted in decreased pitting corrosion resistance [19].

Hot/Cold Rolling

Hot rolling procedure involves plastically deforming continuously cast segments of steel with a roller around 1000°C, typically resulting in a coarser microstructure because of the slower cooling rate [9]. Dual phase steels can be manufactured by means of hot rolling under the austenite region [20].

If the rolling process is executed at room temperature it is referenced as cold rolling. Even though its not a thermal process it is widely used to increase the dislocation density and change the orientation of crystals. More severe versions of grain deformation also create a finer microstructure.

1.4.2. Microstructure

Microstructural features of commonly seen phases in corrosion research is briefly outlined in this section. To elucidate the discussion, optical microscopy and SEM images of mentioned microstructures are provided in figure 1.6.

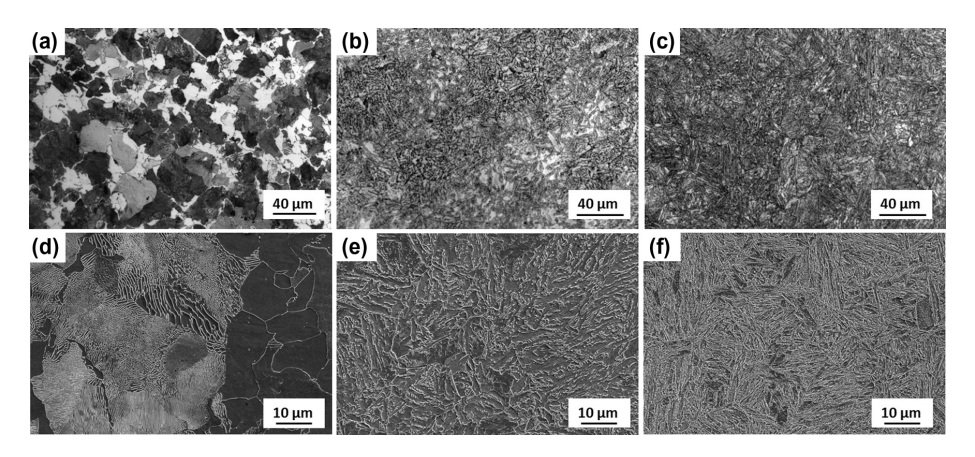


Figure 1.6: Steel microstructures produced as a result of different heat treatments. (a,d) ferrite-pearlite, (b,e) bainite, (c,f) tempered martensite microstructures investigated by (a-c) optical microscopy, (d-f) SEM [21].

Ferrite Ferrite is the body-centred cubic (BCC) phase of iron that is stable at room temperature. It transforms into austenite at A_3 temperature or above 900°C for pure iron. It has a considerably low carbon solubility. In combination with cementite as alternating layers, it is detected as lamellar pearlite in many forms of steel. The morphology of ferrite can change considerably depending on the cooling rate and chemical composition.

Austenite Austenite is the face-centred cubic (FCC) phase of iron that is stable at elevated temperatures. The transformation kinetics of austenite into ferrite is the core reason of multitude of different metastable phases distinguished in steels. The transformation is accompanied by 1-3% volume change which can cause residual stresses [9]. Carbon solubility of austenite is substantially higher than ferrite and this difference can lead to various phenomena that change microstructure drastically, as seen in martensitic transformation.

Cementite Cementite is a thermodynamically metastable carbide with the chemical formula Fe_3C . It is found dispersed in the steel matrix, and commonly formed as a product of the diffusion of supersaturated phases.

Pearlite Pearlite is a common microstructure with substantial strength and ductility, due to its ductile ferrite phase and hard cementite phase. It is the lamellar mixture of ferrite and cementite that contains 0.76 wt.% carbon, which is the result of the eutectoid transformation of the steel at 727 °C [9]. It forms when the kinetics of the transformation is sluggish and cooling rate slow. A pearlite colony is a bi-crystal structure controlled by the cooperative diffusional growth of ferrite and cementite. Lamellae fineness and colony size determine pearlite's final properties.

Martensite Martensite is a body-centred tetragonal microstructure supersaturated with interstitial carbon. It is a very hard and brittle phase. It has a very high dislocation density and is the result of a displacive transformation. Rapid cooling rates that prevent diffusion result in the martensite microstructure. Its chemical composition is identical to the parent austenite phase. The morphology consists of thin plates or laths [9].

Bainite Bainite is a microstructure that is formed by fine ferrite plate clusters with cementite particles [9]. It has a high dislocation density. Unlike pearlite, carbide distribution is non-lamellar and grain structure is usually finer. It is formed when austenite to ferrite transformation is restrained by alloying elements [22].

Acicular ferrite is a disorganised intragranularly nucleated bainite [9]. During experiments with a certain steel composition, the dominating microstructure was martensite, acicular ferrite and polygonal ferrite for cooling rates of 50°C/s, 20°C/s and 0.1°C/s respectively [23].

1.5. Effect of Microstructure on Corrosion of High Strength Steels

Corrosion behaviour of steel is the combined result of the individual features of the microstructure. An electrochemical system is created as a result of the interaction between the steel and the environment. Microstructure modifies the corrosion resistance by changing the thermodynamics and kinetics of this electrochemical system. Iron dissolution reactions and oxide formation mechanisms on top of the metal substrate are impacted by various microstructural features such as:

- grain boundaries interfacial area of grains,
- chemical composition,
- behaviour of interstitial and subtitutional alloying elements (partitioning, non-homogeneous distribution in the microstructure, etc.)
- emergence of galvanic pairs between different constituents of the microstructure,
- residual stresses,
- different properties of passive films,
- crystal orientations,

and the combination of these features gives the corrosion response of the steel. In most cases these effects are coupled with each other and the underlying cause of the resulting behaviour is not clear. Therefore, a thorough understanding of the impact of diverse microstructural features is essential.

In this section, the effect of microstructure on the corrosion behaviour is summarised. It is known that low alloy steels have comparatively weaker passive layers

and prone to uniform corrosion [24]. Because of the uniform corrosion tendency, pitting phenomenon is of secondary importance - unlike stainless steels' case - and hence is not the focus of this review. This review does not cover highly alloyed steels such as TWIP and stainless steels as the high alloying content starts to dominate the corrosion behaviour. The influence of plastic [25, 26] and elastic [27] deformation on corrosion is also not taken into consideration thoroughly even though it is particularly important, for example in oil and gas industries.

The focus of this section is the importance of individual microstructural features and the resulting behaviour that arise from their coupling. Where it is possible, contributions of different features are isolated and contradictory results found in literature are attempted to be explained. First, the effect of grain structure is discussed. Then, the interaction that arises from different electrochemical properties of diverse phases is underlined. After discussing the role of the oxide layer that arises as a result of the corrosion process, an overview of alloying element contributions is presented. The goal is to reveal the microstructure dependency of the complex corrosion phenomena.

1.5.1. Grain Structure

Grain structure controls the corrosion behaviour by governing the microstructural features at and below the grain scale. At the grain scale, the size and morphology of the grains influence the electrochemical behaviour due to the change in interfacial areas. At the sub grain scale, the grain features such as dislocation density impact the behaviour of the system by controlling residual stresses. Crystallographic orientation of the grains affect the corrosion mechanisms.

The overall trend is that smaller, acicular grains with excessive residual stresses have increased surface reactivities that result in inferior active corrosion resistance but superior passive layer properties. This is consistent with the idealised behaviour hypothesised in the review of Ralston and Birbilis [28]. Crystallographic orientation of the steel clearly impacts the dissolution and oxide build-up reactions but more work is required.

Grain Size

Microgalvanic anode and cathode areas form in the microstructure to initiate corrosion. Dissolution of iron occurs in the anodic areas and reduction reactions take place in the cathodic areas. In the presence of different microstructural features, galvanic areas are assigned according to their electrochemical activities. For a multiphase structure, anodic and cathodic areas can be assigned to individual phases.

The significance of interfacial area between the anode and the cathode phases has been highlighted in recent research. Finer structures (smaller grain sizes) with increased interfacial areas corresponded to higher corrosion rates [13, 18, 22, 29–31]. This is not only due to the facilitated interaction between anodic and cathodic zones but also because of the general increase in more active grain boundary areas. Grain boundaries introduce more active lattice mismatches and additionally allow previously forbidden states of the electronic band structure of the oxide layer formed on top of the substrate steel [32]. The resultant finer microstructure has a higher

ionic and/or electronic conductivity as well as higher surface reactivity.

It must also be pointed out that altering the grain size can also cause other parameters to change. Grain size modification is potentially coupled with many different microstructural features such as residual stresses and morphology among others. For this reason, it is hard to isolate its effect. Literature contains contradictory results, possibly because the outcomes are attributed to the wrong microstructural features.

A peculiar behaviour that may be the result of the previously mentioned complex effect of grain size alteration is seen in the case of pearlite. In the research of Katiyar et al. [33], the corrosion resistance of coarse, medium and fine pearlite steel samples increased with decreasing grain size but decreased slightly with the very fine grain sample. This result contradicts the straightforward explanation of the grain size effect. This is explained via the corrosion process becoming more uniform with finer pearlite lamellae, as explained further in section 1.5.2.

The study of Yu et al. [34] found that corrosion rate decreases with an increase in cooling rate for ferritic steels and correlated it with increased fineness of the structure and increased percentage of low-angle grain boundaries. This is counterintuitive, as an increase in corrosion rate is expected with increased refinement of the microstructure. The dominating effect could be the result of other microstructural features aside from the grain size, such as inclusions and crystallographic orientation.

Morphology

Phase morphology directly determines the interfacial area between phases and influence the interaction between grains, and in the presence of galvanic corrosion, anodic and cathodic areas. Spheroid morphologies have lower surface area than pointy or needle-like structures. A morphology of fine needles or lamellae enhance the surface area, increasing the interaction between microgalvanic cells and consequently accelerating galvanic corrosion [12].

A ferrite-martensite microstructure comparison of bulk martensite with fibrous martensite in weak acidic environment demonstrated higher corrosion tendency and lower corrosion rate of bulk martensite, which had a decreased interfacial area than fibrous martensite [35]. Higher interfacial area provided by a fine fibrous ferrite-martensite structure resulted in higher corrosion currents [36], while spheroid-like island martensite morphology is found to be more corrosion resistant on account of the lower surface area to volume ratio [13].

A denser oxide with lesser defects grows on acicular ferrite morphology than polygonal ferrite and martensite [23]. Field emission scanning electron microscope investigations revealed the surface corrosion products of polygonal ferrite and martensite to be highly porous and relatively loose, while acicular ferrite surface was compact and complete. It can be inferred that the morphology of the metal determines the physical barrier properties of the oxide layer and alter the protectiveness of the film considerably.

Residual Stresses

Residual stresses aggravate corrosion by creating more active microstructures. The modification in surface energy can influence the chemical reactions by facilitating atomic mass transport [27]. The reduced activation energy by an increase in dislocation density accelerates the corrosion rate [16]. The combined effect of finer grains and higher dislocation density increased corrosion rate of a pearlite specimen by a factor of 3 after plastic deformation [26].

Martensitic transformation generates residual stresses due to introduced dislocations and the deformation caused by the change into a body centred tetragonal lattice structure. The distorted microstructure is deleterious for corrosion resistance [12]. It is argued that the captive carbon and residual stresses change the electrochemical properties of the matrix and decreases the overpotential for the hydrogen evolution reaction [37]. Carbon diffusing into the dislocation zones on the surface create locally cathodic zones, further enhancing galvanic corrosion by increasing the total cathodic area of the microstructure [24].

The dislocation density of the ferrite matrix in a ferrite-martensite dual phase steel also increases as a result of the volume expansion from austenite to martensite phase [20]. It is reasonable to think that this further causes an increase in the activity of the ferrite phase.

Residual stresses on locally corroding pearlite for a ferrite-pearlite weathering steel is claimed to be the main cause behind faster corrosion [38]. Volume expansion caused by the corrosion products generates local stresses which promote defects, accelerating the corrosion process.

Crystallographic Orientation

The crystallographic orientation has been found to influence the corrosion behaviour of pure metals such as copper [39, 40] and iron [14, 41]. Schreiber et al. [14] and Fushimi et al. [41] reviewed the literature on pure iron and saw that the data on the dissolution rate of low index $\{100\}$, $\{101\}$ and $\{111\}$ planes varied widely. The behaviour is found to be highly sensitive to the environment and corrosion mechanisms.

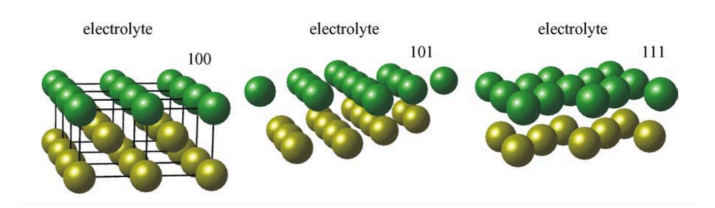


Figure 1.7: Three dimensional crystallographic orientation models of $\{100\}$, $\{101\}$ and $\{111\}$ [14]. Horizontal packing density of $\{111\}$ is the largest, $\{100\}$ has the shortest distance to the next layer.

The experiments carried out by Schreiber et al. [14] in acetate buffer solution (pH 6.0) showed that pure iron dissolves fastest on the laterally most densely packed plane {111}, and oxide formation is easier on the more loosely packed {100} orientation. The distribution of different packing directions in space is shown

in figure 1.7. For $\{100\}$ orientation, the surface is closer to the next iron layer than $\{111\}$. It is argued that this allows stronger bonding of the layers, slowing down the dissolution reaction. Even though $\{111\}$ layer has the larger atomic packing density in the horizontal direction, the larger distance to the next layer results in weaker binding. The more compact structure of the layering stabilises the surface against corrosion. On the other hand, Fushimi et al. [41] noticed a different behaviour at sulphuric acid (pH 1) solution. The decrease in corrosion activity in the order of $\{100\}$, $\{111\}$ and $\{101\}$ is explained not by the surface energy or work function but by the behaviour of d-orbital electrons.

Research on pure iron lays the foundation to understand the grain orientation relation of HSLA steels. The electrochemical behaviour of steels is affected by the packing structure and grain orientation, however introduction of alloying elements and other external factors make it harder to isolate the precise contribution of crystallographic orientation. Relevant works have appeared in the literature, but studies regarding the effect of grain orientation on active corrosion behaviour is inadequate.

Similar research studied relevant effects, such as the work of Shen et al. [31] where anisoptry of a pearlite is studied by investigating the orientation distribution of cementite. The phases with an orientation that led to finer surface structures created a more uniform distribution of galvanic areas and generated higher residual stresses, resulting in faster corrosion.

Misorientation of grains with regard to each other is found to be impacting corrosion behaviour. For the corrosion properties of polycrystalline copper, the orientation of neighbouring grains is shown to be more important than the self-orientation of the grain and low angle grain boundaries are found to be more stable than high angle grain boundaries [39]. Steel is accepted to show the same behaviour [42]. In support of this hypothesis, the experiments of Yu et al. [34] showed a correlation between an increase in low angle grain boundary percentage and an increase in the corrosion resistance. Increased presence of randomly distributed low angle grain boundaries is proposed to reduce intergranular corrosion [42].

A peculiar behaviour is recognised by Si [43], the dissolution of ferrite in a dual phase steel specimen is found be non-uniform - some small grains had dissolved faster than the larger ones. This could be related to the crystallographic orientation; smaller grains with larger misorientation angle differences from the matrix could be the main reason for faster dissolution.

It is clear that crystallographic orientation is an important factor in corrosion of steels. More work is needed to gain a thorough understanding of the isolated effect for the steel specimens.

1.5.2. Phase Constituents

Electrochemical properties of phase constituents greatly impact the corrosion behaviour. Contributions of phase properties, combined behaviour of phases in multiphase microstructures and inclusions are analysed in this section.

Phase Properties

Ferrite Ferrite is the more active phase in most of the thermodynamical conditions. It tends to dissolve and oxidise by giving away its electrons. In every paper analysed for this review it played the role of the anode when coupled with a different phase.

Austenite Austenite has a high tendency to corrode, especially due to its metastable nature at room temperature [44]. For a neutral environment, austenite preferentially corrodes rather than martensite [45]. Galvanic coupling effect of austenitemartensite is lower due to the similar carbon content of the phases.

Cementite Cementite has a lower corrosion tendency than ferrite in neutral pH conditions [46]. When coupled with ferrite it acts as additional cathodic area, increasing the galvanic effect and exacerbating total corrosion.

Bainite Corrosion tendency and rate of bainite is lower than ferrite in neutral pH environment [47]. Low carbon bainitic steels are recently used in weathering steels as a replacement for ferrite-pearlite microstructure [38]. Although the corrosion rate is still smaller, polarisation experiments done in 0.6M NaCl show bainitic microstructure to be less noble than the pearlitic one for the same steel [48].

A different behaviour is recognised by Onyeji et al. [22]. The bainitic microstructure with dispersed acicular ferrite developed a sludge-like porous corrosion product which led to the spallation of the oxide layer. This resulted in a higher corrosion rate than ferrite-pearlite microstructure. It is unclear whether the bainite microstructure is the main source behind this behaviour, as it is also reported that higher chromium and carbon content has generated chromium carbides that has increased the cathodic area.

Localised corrosion of a bainite sample under elastic loading conditions was found to be superior than dual phase steel samples [27].

Martensite Due to its carbon content, martensite has a more noble corrosion potential than ferrite [12], however it corrodes three times as fast as ferrite [37]. The disordered lower density of the martensite surface increases the surface energy [49] which contributes in higher cathodic activity. In a similar manner, higher surface energy increases the iron dissolution reaction [37]. Consequently, martensite dissolves faster than ferrite if it is the anode, and facilitates the cathodic reactions if it is the cathode.

Guo et al. [23] obtained contradictory results, the corrosion potential of martensite is found to be lower than acicular and polygonal ferrite. This may be due to the unexplored effect of the rest of the microstructure.

Research of Kadowaki et al. [19] determined the pitting resistance of as-quenched martensite to be better than tempered martensite. It is argued that increased interstitial carbon content decreases the martensite activity, therefore higher interstitial carbon content of as-quenched martensite leads to improved pitting resistance.

Behaviour of Phase Combinations

Pearlite Steels Galvanic corrosion occurs for pearlite steel where cementite acts as the cathode and ferrite the anode. The galvanic coupling between ferrite and cementite enhances the corrosion of ferrite and consequently increases the corrosion rate [23]. High cementite volume fraction facilitates corrosion by increasing the cathodic area [48].

The preferential dissolution of ferrite results in cementite accumulation and this buildup further accelerates galvanic corrosion [20, 50]. In comparison with structures like bainite where carbides are distributed in the matrix more uniformly, separation of anode and cathode zones as in the lamellar structure of pearlite is proposed to increase the cathodic area on the surface and therefore induce greater corrosion [48].

Researchers [12, 33] proposed that finer pearlite lamellae result in a more homogeneous distribution of the pearlite that minimise corrosion development. The formation of well-distributed microgalvanic cells becomes more probable with the finer pearlite colony, making the corrosion process more uniform. This also results in a more active corrosion potential, increase in interfacial area between cementite and ferrite makes the microstructure thermodynamically more active as expected. The carbide phase is closer to the ferrite phase in a finer microstructure, permitting it to act as a barrier against corrosion [12]. However, after a critical point the fineness of the lamellae leads to the entanglement of the alternate lamellae, increasing the interfacial area and short-circuiting the microgalvanic cells [33]. Corrosion susceptibility of the interfaces between pearlite colonies is also related to the increased entanglement and increased exposure of the anodic ferrite regions [33]. It is argued that the prior austenite grain size can be utilised to limit the interaction and result in a more corrosion resistant steel. The optimum pearlite colony and lamellae size is key in controlling the corrosion phenomena.

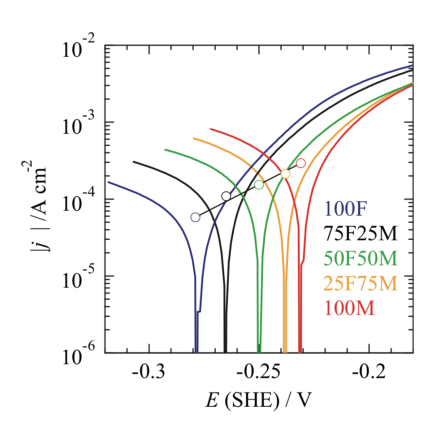
The lower corrosion rate of acicular ferrite is explained by Guo et al. [23] with a similar argument, the uniform distribution of phases puts the anode and cathode areas near each other, minimising the corrosion rate.

Undissolved cementite platelets in the presence of galvanic corrosion act as anchoring points for oxide layer, improving the adherence of the oxide layer to the metal substrate [22]. This could be the reason behind the encountered lower corrosion current for pearlite than dual phase specimens [15]. Additionally, lower amount of $\mathcal{C}l^-$ ions are detected on the surface of pearlite. The difference in adsorbed $\mathcal{C}l^-$ could cause pitting in dual phase steels while pearlite stays intact.

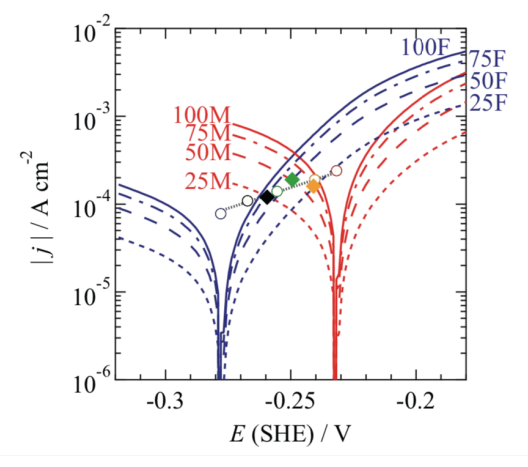
Dual Phase Steels Dual phase (DP) steels consist of one ductile and one hard phase, establishing a formable but strong structure suitable for critical applications in many areas such as construction [16] and automotive industries [9].

It is shown that corrosion of dual phase steel is determined by the competition between the self corrosion of phases and galvanic corrosion, for instance by the occurrence of microgalvanic cells where martensite acts as the cathode and ferrite the anode [12, 16, 37]. Fushimi et al. [37] noticed a more significant corrosion of ferrite phase than martensite phase when analysing 50% ferrite - 50% martensite

steel in 0.1M sulphuric acid solution, demonstrating the occurrence of both nonuniform galvanic corrosion coupled with general self-corrosion. Experiments with 100% ferrite and 100% martensite demonstrated self-corrosion of martensite to be three times faster than self corrosion of ferrite. By keeping the carbon concentration in the ferrite and martensite phases constant when changing the phase composition, the effect of volume fraction is isolated. The behaviour of different phase fractions can be seen in figure 1.8a. It is seen that the corrosion tendency decreases and corrosion rate increases as the martensite content is increased. This behaviour is also reported widely in literature [13, 15, 16, 30, 36].



(a) Dynamic polarisation curves for dual phase steels with different volume fractions. White circles: corrosion current and potential determined by Tafel extrapolation.



(b) Evans diagram calculated from the polarisation curves of 100% ferrite and 100 % martensite respectively. Solid circles: corrosion current and potential determined from crossing anodic branch of the ferrite with cathodic branch of the martensite for various phase compositions.

Figure 1.8: Electrochemical behaviour of ferrite-martensite dual phase steel in 0.1M sulphuric acid solution: (a) polarisation curves, (b) Evans diagram [37].

Careful analysis shows that the relationship between galvanic corrosion rate and and martensite volume fraction is not linear. Increase in the martensite volume fraction exacerbated the corrosion owing to the increased cathode to anode area ratio [13, 36] and increased residual stresses developed by the martensitic transformation [12, 51]. With more cathodic area and faster self-corrosion of martensite phase, it would be sensible to expect faster corrosion with higher martensite volume fraction. However, as seen in figure 1.8b, corrosion current does not increase as high as it should for equal ferrite-martensite volume fraction. This is because the Evans diagram shows the perfect galvanic coupling behaviour; there must be a competition between self-corrosion and galvanic corrosion of the phases that reduces the effect of galvanic corrosion and decreases the overall corrosion rate. The decrease of corrosion rate with further increase in martensite volume fraction highlights the competition between galvanic corrosion and self-corrosion mechanisms.

Kumar et al. [20] have demonstrated that ferrite-martensite dual phase steel

with equal volume fraction corrodes faster than ferrite-pearlite steel which in turn corrodes faster than ferrite - 30% martensite steel. On the other hand, Bhagavathi et al. [52] have reported faster corrosion of ferrite-pearlite steel, meanwhile Ramirez-Arteaga et al. [53] have reported decreasing corrosion rate with increasing martensite volume fraction. The contradictory behaviour most likely arises from not taking into account the non-linear martensite volume fraction effect on the corrosion behaviour and overlooking the other dominant changes in the microstructure. This erratic behaviour further underlines the importance of understanding individual microstructural features of HSLA steels.

Ferrite-bainite DP steels show a similar behaviour to ferrite-martensite DP steel where ferrite is the anode and bainite the cathode [47, 48]. Dissolution starts at the ferrite grain boundary and inside the ferrite grains; ferrite phase is determined to have higher activity and dissolution rate [47].

Retained austenite acts as the anode and martensite the cathode for austenite-martensite DP steels. Unlike other dual phase microstructures, corrosion is not dominated by galvanic effects as both phases have similar carbon contents and electrochemical potentials [45]. Experiments showed significant pitting for austenite phases while martensite phases corroded more slowly.

TRIP Steels Transformation induced plasticity (TRIP) steels utilise the transformation of retained austenite into martensite during the plastic deformation to generate a strong and ductile structure [9].

Specific literature on corrosion behaviour of TRIP steels is not sufficient. Zhang et al. [54] examined the impact of alloying elements on corrosion resistance of TRIP steels. A conventional C-Mn-Si TRIP steel with inferior corrosion properties than a conventional weathering steel is improved by the addition of Al, Cu, Cr, Mo. The influence of plastic deformation on TRIP steels is investigated by Mandel et al. [25]. Plastic deformation is found to enhance electrochemical activity of the oxide layer and change the pitting behaviour. Park et al. [55] reported better pitting resistance of ferrite-bainite-retained austenite TRIP steel than the pitting resistance of ferrite-martensite DP steel [55]. The reason behind better corrosion properties of TRIP steel is argued to be the lower inclusion density and corrosion resistant Al_2O_3 inclusion content.

It is seen that the investigations that focus on multi-phase steels except DP steels are not towards illuminating the mechanics of the microstructure but more on finding out the effect of minor compositional changes. Further research to understand the fundamental electrochemical phenomena is required.

Q&P Steels Q&P stands for "quenching and partitioning" process. Quenching austenite below martensite start temperature followed by a partitioning heat treatment process enriches retained austenite and allows the formation of a carbon rich stabilised austenite at ambient temperature [56].

Galvanic corrosion enhances iron dissolution in Q&P steels as it is also a multiphase structure. Corrosion response of the microstructure is shown in figure 1.9. Retained austenite acts as the cathode and carbon depleted martensite as the an-

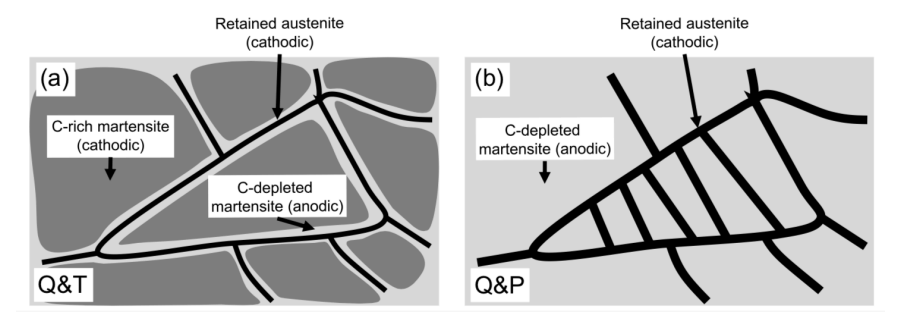


Figure 1.9: Schematic representing the microstructure of (a) Q&T and (b) Q&P structures. Black lines depict austenite, dark grey areas depict carbon rich cathodic martensite, grey areas depict martensite [24].

ode. Carbon solved in martensite after a tempering process (O&T) alter the potential to be more cathodic, but in the vicinity of retained austenite carbon atoms of martensite diffuse into austenite with the tempering process, dropping the potential of boundary martensite and making near-austenite martensite zones more anodic. As a result of the different concentration of carbon atoms, martensitic areas close to the retained austenite become more anodic compared to the other parts of the grain. Retained austenite is also cathodic to the carbon depleted martensite in this state. In the partitioning process, the diffusion of carbon into the austenite is fully realised and carbon concentration is stable in a single martensite grain. Total cathodic area is reduced in the resulting O&P state but the potential difference between the phases becomes much higher after the completion of partitioning. High dispersion of retained austenite and higher electrochemical potential difference of O&P results in enhanced galvanic coupling in comparison to O&T. Additionally, increased carbon in the retained austenite of Q&P diffuse into dislocation zones, creating locally cathodic features. Consequently, the corrosion rate for quench and partitioning treatment becomes significantly higher than guench and tempering treatment for an acidic environment [24].

Compositional Differences The effect of chemical composition difference seen in Q&P steels is also seen in DP steels. Concentration of alloying elements such as manganese and silicon are different in different phases. It is reported that manganese concentration increases while silicon concentration decreases from retained ferrite to epitaxial ferrite to martensite [57]. Salamci et al. [16] reported a decrease in corrosion rate and tendency for DP steels that contain epitaxial ferrite. It is argued that the intensity of the galvanic coupling is reduced by the introduction of epitaxial ferrite between retained ferrite and martensite. Epitaxial ferrite acts as a buffer zone because of its intermediate chemical composition. The potential gradient between different phases smoothens out due to the less intense jumps in compositional differences.

22 1. Background

1

Inclusions

The understanding of the effect of nonmetallic inclusions such as MnS is not only important for the pitting corrosion of stainless steels but also for the analysis of the corrosion of HSLA steel specimens. Corrosion behaviour of the steel can be improved with proper control of the type, size and distribution of the inclusions.

 MnS inclusions act as additional cathodic areas in low alloy steels, reinforcing the local dissolution of the matrix [50]. MnS , CaS , MgS and SiO_2 inclusions are shown to impact local corrosion resistance of low carbon steels in aqueous environments and among them inclusions containing calcium and sulphur are shown to be the most dangerous [51].

The cathodic carbide areas such as cementite protruding from the surface is proposed to cause severe oxygen evolution, thereby increasing the corrosion rate [46]. Carbides distributed in the matrix dominate the total area in time with the progressively dissolving anodic phase, which further accelerates the corrosion rate [23].

High content of oxide inclusions increase the conductivity of the passive oxide layer considerably and therefore decrease the corrosion resistance of passivated steels [51].

Larger inclusions increase the pit initiation likelihood. It is known that inclusions larger than μm range have low pitting corrosion resistance [55]. A lower density of inclusions with a diameter greater than 1 μm results in better pitting corrosion properties.

1.5.3. Passivation and Oxide Layer Properties

Corrosive species in the environment oxidise the surface of the metal. An oxide layer starts to develop as the product of electrochemical reactions between the metal and the environment while a cathodic reaction proceeds in a different area to keep the charge neutrality. Passive oxide layer forms a protective film that limits corrosion by diminishing ion and/or electron transfer.

Structure of the Oxide Layer

The structure and composition of the oxide layer is one of the main factors that determine the corrosion resistance. The structure of the oxide layer decreases corrosion rate by preventing corrosive species from penetrating inside and keeping the contact between the metal and environment to a minimum. Homogeneity and porosity of the oxide layer combined with its electrochemical properties have a huge impact on the corrosion behaviour. Compactness of the oxide layer is one of the main factors that determine the corrosion protection [23]. Irregular and open structures permit easier access of corrosive species such as oxygen to the substrate under the protective oxide film [48].

The passive film of pure iron demonstrates n-type semiconductor properties. It consists of either a bi-layered structure with inner Fe_3O_4 and outer γ/α - Fe_2O_3 or a similar spinel structure. The electronic resistance of bulk Fe_2O_3 is significantly larger than Fe_3O_4 (a difference in the range of 10^{10} Ω m for γ - Fe_2O_3 [58] and 10^{16} Ω m for α - Fe_2O_3 [59]), in spite of its higher defect concentration. The charge

transfer resistance is determined by the electronic transfer rather than the ionic transfer [58].

Pure iron serves as the template for understanding the oxide behaviour of HSLA steels. Addition of carbon and other alloying elements to the system modifies the thermodynamics and electrochemical reactions. As a result, different artefacts are examined according to the produced phase and other microstructural features.

Different forms of iron oxide-hydroxide are obtained as rust products in the oxide layer such as magnetite (Fe_3O_4) , maghemite $(\gamma-Fe_2O_3)$, hematite $(\alpha-Fe_2O_3)$, lepidocrocite $(\gamma-FeOOH)$, goethite $(\alpha-FeOOH)$ and feroxyhyte($\delta-FeOOH$) [48, 54, 60]. The physical and chemical properties of these compounds are known for a long time [61], but their role in the corrosion of HSLA steels is still not clearly evident.

Oxide layer of steels is formed mainly out of a mixture of Fe_3O_4 , Fe_2O_3 and FeOOH [54]. Relatively higher Fe_2O_3 component in the oxide layer is correlated with a more protective oxide properties [48, 58–60].

 α -Fe00H is more stable and less soluble than γ -Fe00H owing to the higher stability of its bonding configuration [48]. It is also able to suppress the penetration of Cl^- [54]. Formation of β -Fe00H is favoured in the presence of chlorine and it is a harmful oxide component [60].

Comparison of Oxide Layers of Different Phases The oxide film of pearlite is found to be thicker and more inferior than the oxide layer of pure ferrite. Pearlite has a higher electronic/ionic conductivity. Higher conductivity arises from the significant amount of carbon in the oxide introduced through the addition of cementite and the resultant finer grain microstructure. $FeCO_3$ forms in the oxide as a result of the underlying cementite substrate which decreases charge transfer resistance. Pearlite-ferrite boundary is highly active, most likely due to the uneven alloying element distribution such as manganese in the pearlite substrate. The introduction of mismatches and additional energy states with the grain boundaries make the structure more active overall. As a result, pearlite phase has poorer passive layer structure than pure ferrite [32].

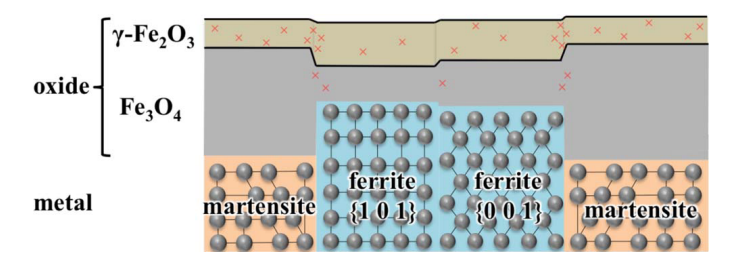


Figure 1.10: Dual phase steel oxide structure schematic [49]. Martensite forms a thicker more defective oxide film with a larger fraction of Fe_3O_4 , which deteriorates the protective properties of the martensite oxide layer.

The oxide structure of a dual phase carbon steel is represented graphically in figure 1.10. The oxide film of martensite is relatively more stable and more conductive than that of ferrite. Substantial lattice mismatches of the martensite introduces

large number of defects, creating a thicker porous oxide. It is believed that distorted surface of martensite facilitates Fe_3O_4 formation, increasing Fe_3O_4 fraction and in turn increasing the electrical conductivity of the whole film. Defect concentration of the oxide layer of martensite is comparable with the case of 50% martensite - 50% ferrite microstructure; defective oxide film is attributed to the misorientation introduced by the grain boundaries. As a result, it is seen that a considerably more conductive thicker oxide film is formed on martensite phase and martensite-ferrite composition has properties in between martensite and ferrite structure. The passivity of a ferrite-martensite DP steel is proposed to be limited by the passive properties of the martensite phase [49].

In the conditions where Fe^{+3} formation is favourable, the oxide layer of ferrite contains a higher amount of oxygen vacancies than the martensite, facilitating chloride penetration into the film to initiate pitting [51]. This causes the passive oxide layer formed on the ferrite at a slightly basic environment (pH 6.0) to be less protective for pitting corrosion than the oxide layer of the martensite.

The passive oxide layer of bainitic steels formed in 0.6M NaCl is compact and nonporous, resulting in better corrosion protection than pearlite [48]. Ferrite-bainite microstructure showed higher passive corrosion resistance in a slightly basic environment (pH 6.0) than ferrite-pearlite and martensite microstructures, despite having a high residual stress as a result of high dislocation density and carbon supersaturation [51]. Uniformity of the oxide layer of bainite is thought to be the underlying reason behind pitting prevention.

The oxide scale on bainitic steel is composed of a dense inner and a loose outer layer. The major phases in both layers are Fe_3O_4 and γ - Fe_2O_3 . As the corrosion progresses Fe_3O_4 percentage decreases and γ - Fe_2O_3 percentage increases. Increased γ - Fe_2O_3 content in the inner layer is believed to be the source of the higher density of the inner layer. Higher amounts of γ - Fe_2O_3 is suggested to represent a more inactive oxide layer while Fe_3O_4 is proposed to indicate a more active rust layer [60].

Oxide Layer Growth

Advanced theoretical models to understand the oxide layer growth are developed in literature [62]. Instead of a similar theoretical analysis, a qualitative overview of oxide growth is provided in this review to describe the main differences between various microstructures of HSLA steels.

The bi-layered oxide formation of polycrystalline iron starts with the production of Fe_3O_4 . Afterwards, Fe_2O_3 layer start to develop on top of the Fe_3O_4 layer, passivating the surface with its improved charge transfer resistance. Aging of the oxide from ferrous to ferric oxides leads to an improvement in the crystallinity of the oxide layer [63]. Consequently, the initial growth rate of Fe_3O_4 and surface coverage rate of Fe_2O_3 control the final oxide properties [59].

The primary reduction/oxidation reactions occurring on the steel surface are:

$$Fe \to Fe^{2+} + 2e^{-}$$
 (1.12)

$$2H^+ + 2e^- \to H_2 \tag{1.13}$$

$$4H^{+} + O_2 + 4e^{-} \rightarrow 2H_2O \tag{1.14}$$

$$O_2 + 2H_2O + 4e^- \rightarrow 4OH^-$$
 (1.15)

where equation 1.12 the anodic reaction and equation 1.13 the acidic oxygen deprived, equation 1.14 the acidic oxygen rich, equation 1.15 the neutral environment cathodic reactions.

Fundamental reduction/oxidation reactions are coupled with auxiliary reactions which result in the creation of oxide and hydroxide layers [12, 23]. Utilising the dissolved iron, hydroxide layers are created:

$$Fe^{2+} + 20H^{-} \rightarrow Fe(OH)_{2}$$
 (1.16)

$$4Fe(OH)_2 + O_2 + 2H_2O \rightarrow 4Fe(OH)_3$$
 (1.17)

$$Fe(OH)_3 \to FeOOH + H_2O$$
 (1.18)

The hydroxide can be oxidised to form Fe_2O_3 :

$$4Fe(OH)_2 + O_2 \rightarrow 2Fe_2O_3 + 4H_2O$$
 (1.19)

 γ -FeOOH forms first, then transform into α -FeOOH and Fe₃O₄ [54, 60]:

$$Fe^{2+} + 8FeOOH + 2e^{-} \rightarrow 3Fe_3O_4 + 4H_2O$$
 (1.20)

 Fe_2O_3 can also be reduced into Fe_3O_4 , which dissolves chemically in acidic environment [58]:

$$2Fe_2O_3 + 4H^+ + 2e^- \rightarrow Fe_3O_4 + Fe^{2+} + 2H_2O$$
 (1.21)

Interaction between the environment and microstructure dictates the potential, kinetics and available corrosive species. Final composition of the oxide layer will be determined by these parameters.

Corrosion Mechanism and Oxide Growth Model of Pearlite and Bainite Oxide layer growth is influenced by the microstructure, morphology of the constituent phases as well as the corrosion mechanism as represented visually for pearlite and bainite microstructures in figure 1.11. Pearlite phase is arranged in alternating cementite and ferrite lamellae while bainite has a more uniform morphology with evenly dispersed carbides. Ferrite acts as the anode in both microstructures. Therefore, besides self-corrosion of the phases, a micro-galvanic corrosion of the phases simultaneously occur. As the corrosion progresses in pearlite, ferrite

regions corrode more and form deeper valleys. This is due to the more aggressive attack suffered through the lamellar morphology - single anodic ferrite lamella experiences harsher attack due to two surrounding cathodic cementite lamellae. For bainite, dispersed cementite regions form a large number of finer, more evenly distributed microgalvanic cells, resulting in a shallower corrosion. The difference in cathodic area due to the characteristic morphology controls the corrosion rate [48].

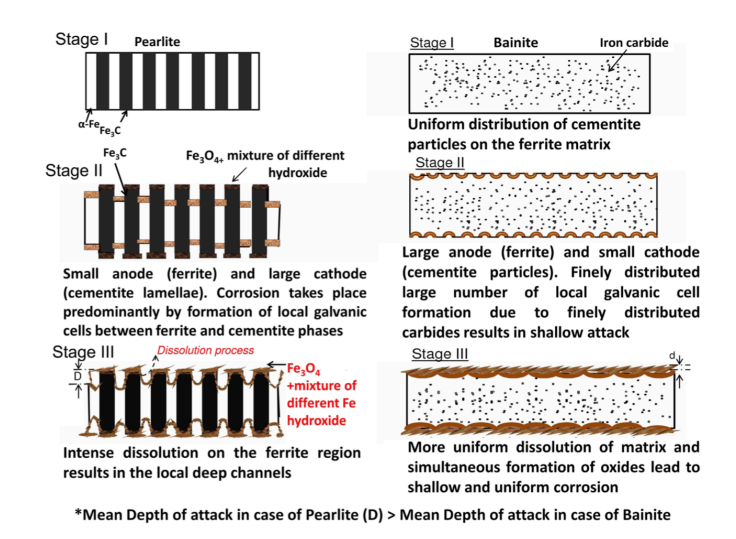


Figure 1.11: Schematic representation of corrosion mechanism and oxide formation of pearlitic and bainitic steels [48].

As the corrosion progresses oxide layers form on top of the substrate. Depending on the composition of the steel and environment, different layers of rust products form on the steel. Deeper mean depth of attack leads to a more disorderly growth which results in a film that is more prone to spalling and corrosive species penetration. Pearlite grows a porous oxide layer that give rise to craters and pits. The more uniform corrosion surface of bainite allows a denser and more compact oxide layer. This produces a more protective oxide layer growth, decreasing corrosion rate [48].

Crystallographic Orientation Dependence of the Oxide Layer

Takatabake et al. [58] observed that the composition of the oxide layer of pure iron in acidic environment depends on the substrate orientation. Fe_3O_4 fraction increased in the order of $\{100\}$, $\{111\}$ and $\{101\}$. Fe_3O_4 shows weaker protective properties than γ - Fe_2O_3 , therefore $\{101\}$ orientation with the highest γ - Fe_2O_3 fraction showed the most protective surface properties. Crystallographic orientation of the substrate determined the oxide fractions as represented graphically in figure 1.12 and controlled the protectiveness of the oxide layer.

Takatabake et al. [59] showed that for an oxide layer of polycrystalline iron formed out of outer α - Fe_2O_3 and inner Fe_3O_4 , Fe_3O_4 fraction and the donor density

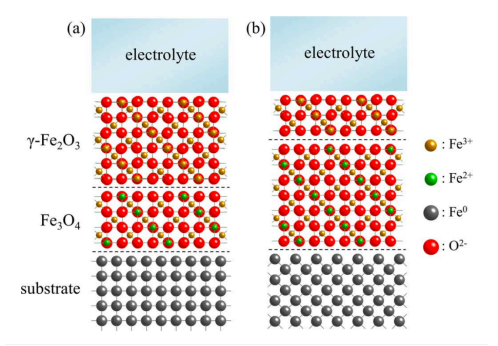


Figure 1.12: Grain orientation dependence of oxide composition assuming a bi-layer structure, (a) {101} and (b) {001} single grain surfaces [58]. Oxide composition is directly affected by the crystallographic orientation of the substrate layer.

increased in the order of $\{101\}$, $\{111\}$ and $\{100\}$. Oxide layer thickness is also recognised to be dependent on crystallographic orientation. Thickness became larger in the order of $\{101\}$, $\{111\}$ and $\{100\}$. $\{100\}$ had the thickest and most defective oxide. Inner oxide layer thickness is observed to be strongly dependent on the substrate orientation but little correlation is seen with the outer oxide layer.

Final thickness and defect concentration is directly related to the growth geometry of the oxide layer. The geometry of the substrate-oxide and oxide-oxide interfaces results in anisotropic growth of the oxide. Figure 1.13 represents the oxide growth mechanisms for different grain orientations. α - Fe_2O_3 preferentially grows on the {111} plane, as shown with an arrow in figure 1.13. Relatively flat Fe_3O_4 surface of {101} plane is rapidly covered by α - Fe_2O_3 , forming a thin and compact oxide layer with smallest thickness. For {111} and {100} orientations partially lateral growth of oxides induces compressive residual stresses into the oxide layer, creating a thicker, more defective oxide layer [59]. Thickness, defect density and composition of the oxide is determined by the crystallographic orientation of the substrate and successively controlled the corrosion behaviour.

Grain orientation dependence is further studied by Takatabake et al. [63] for a polycrystalline iron oxide composed of outer γ - Fe_2O_3 and inner Fe_3O_4 . In contrast with their own previous research, inconsistencies between charge transfer resistance, defect densities and grain orientation dependence are observed. There was little difference in the thickness of the oxide formed for $\{100\}$, $\{111\}$ and $\{101\}$. Composition of the oxide layer is found to be independent of the substrate orientation. It is clear that there is a grain dependency during the oxide growth, therefore this behaviour suggests that passive film formation is a complex phenomenon that is dependent on the changes in both electronic and ionic conduction during the film growth.

Grain dependence of the electrochemical behaviour of pure iron is important in understanding the fundamentals of the passive layer growth during the corrosion of HSLA steels. Pure iron's complex and sensitive behaviour puts practical limitations on the investigation of the effect of crystallographic orientation for steels, in which

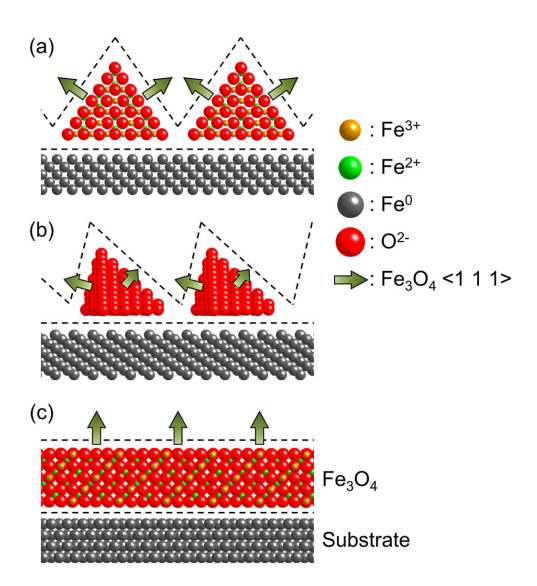


Figure 1.13: Anisotropic growth mechanism of Fe/Fe_3O_4 interface. Grain orientation of the substrate iron: (a) {100}, (b) {111}, and (c) {101}. Arrows represent the preferential growth direction of α - Fe_2O_3 [59].

microstructural factors affect each other. Further work is clearly needed to understand the grain orientation dependence of steels. The behaviour of pure iron lays the foundation for understanding the essential role of crystallographic orientation in oxide growth intricacies.

1.5.4. Chemical Composition

Individual assessment of the effect of chemical composition is most complex, as the change in any alloying element also impacts various aspects of microstructural features. The different composition can cause the formation of additional less noble inclusions (as seen in section 1.5.2) and they in turn can speed up the galvanic corrosion by increasing the cathodic area. Alloying elements can also make a certain structure more noble, for example by standing in the interstitial sites of the crystal, and decreasing the tendency to corrode by increasing the corrosion potential as seen in the case of martensitic structures. Artifacts like these make it difficult to isolate the precise individual effect of alloying elements.

An example of this complexity can be given from the recent research of Gerengi et al. [64]. They proposed that small differences in the chemical composition of dual phase 600 and 800 steels can vividly alter the rate of corrosion. A 50% increase in the corrosion rate is detected with less than 1 wt.% change in the alloying elements. The adjustment is most likely accompanied by a change in the microstructural features like morphology and volume fraction of the phases, albeit no information is provided.

Chemical composition has direct (such as the modification of electrochemical activity) and indirect (such as the change in phase transformation temperatures

successively altering final phase fractions) impact on the corrosion of the microstructure. An extensive analysis is beyond the scope of this review due to its complexity. Relatively important elements that have an important effect on corrosion are presented here.

Carbon Content

Understanding the behaviour of carbon in HSLA steel is critical to clarify the corrosion phenomena. The morphology of carbides and carbon content are important factors in the corrosion behaviour.

Carbon content has direct impact on precipitation and volume fraction of phases. An increase in the carbon content also increases the volume fraction of martensite in DP steel [37] and pearlite in ferrite-pearlite microstructure [22]. Lower carbon content of ultra-low carbon bainitic steel is correlated with better corrosion performance by reduced produced cementite amount and minimal increase in the strain energy [42]. Decrease of cementite often lead to the reduction of corrosion rate by decreasing the cathodic area fraction.

High carbon content is regarded as harmful to the corrosion resistance because of its direct contribution to the cathodic area formation by increasing the volume fraction of cathodic phases (such as an increase in martensite fraction) and precipitates (such as carbides) [22, 29]. Carbon atoms that diffuse into dislocations can potentially lead to cementite decomposition [26] and act as additional cathodic surfaces [24]. Adherence of the passive film is also affected by the carbon content [65].

Contrary to the prevalent notion that corrosion rate increases with increased carbon content, Guo et al. [38] proposed that carbon content up to a certain point is actually useful against corrosion. Carbon-rich phases distributed in homogeneous microstructures like bainite act as anchor points and improve the bonding between the oxide and the substrate, decreasing spalling and resulting in reduced corrosion rate.

Kadowaki et al. [19] demonstrated that interstitial carbon hinders pit initiation and propagation. Ferrite is more active and more prone to pitting corrosion than martensite. The better pitting corrosion of martensite is due to the higher interstitial carbon content of the microstructure.

Additional Alloying Elements

Alloying elements are known to have a substantial impact on the microstructure, as seen in the considerable effect solid solution hardening has on the mechanical properties of the alloy. Alloying impacts corrosion phenomena as well. For instance, micro-alloying with chromium increases the stability of retained austenite and reduces the grain boundary attack, decreasing the corrosion rate [44]. The role of most important elements are briefly mentioned in this section.

Oxide Layer Micro-alloying with elements such as copper, phosphorus, chromium, nickel and silicon aid in the densification of the oxide layer and reduce corrosive environment interaction with the substrate steel [38, 48, 60]. Chromium and molybdenum improve corrosion resistance by acting in favour of passivity [22]. Dissolved

molybdenum is adsorbed on the oxide surface as MoO_4^{2-} and suppress the chlorine penetration, rendering oxide film more stable and hindering pitting [54]. Acetate anion is argued to promote the protective film formation [51]. Chromium, copper and nickel ions are proposed to be improving film properties by acting as heterogeneous nucleation sites for finer oxide and hydroxide formation [48].

A compact and continuous δ -Fe00H layer forms in the presence of copper that offers protection against water and oxygen penetration. Presence of chromium aids the formation of α -Fe00H, which in combination with δ -Fe00H is thought to be the underlying reason of the dense protective layer formed on bainite in neutral pH conditions [48].

Meanwhile exposure to chlorine is claimed to engender β -Fe00H formation which enhances the corrosion susceptibility [48].

It is reported that nickel, chromium, titanium, copper and phosphorus facilitates γ - Fe_2O_3 formation in the inner oxide layer by creation of smaller Fe_3O_4 grains [60].

The passivation range was found to decrease and eventually disappear with increasing sulphur content, leading to poorer passivation [51].

Boronising process improves the oxide layer properties of DP steels significantly by introducing a boride layer which slows down anodic dissolution [15].

Pitting Chloride ions are known to have a substantial effect on pitting. Despite having only a minor influence at the beginning of the passivation process they are detrimental at the subsequent film growth stages [51].

For ferrite-pearlite steels, the pit initiation is examined to start on ferrite as a result of the sulphur-like alloying element segregation [19]. This results in poorer pitting resistance than single phase structures such as ferrite and martensite.

Grain Size Niobium, titanium and vanadium are good grain refiners [22]. An indirect effect of grain refiners is the larger resulting interfacial area, which can potentially aggravate corrosion. Grain boundary areas are more energetic and also could possibly increase the interaction between anodic-cathodic zones.

Partitioning of Elements Partitioning can change the electrochemical potential of phases due to the different elemental concentrations. Severe partitioning of manganese between ferrite and martensite results in larger difference in the chemical composition of the phases, creating a larger difference in electrochemical potential and possibly result in accelerated galvanic corrosion [30].

The segregation of alloying elements into grain boundaries with high disorder in the vicinity can cause intergranular corrosion. Carbon, manganese, sulphur and phosphorus are dangerous elements for intergranular corrosion [51].

1.5.5. Evaluation and Comparison

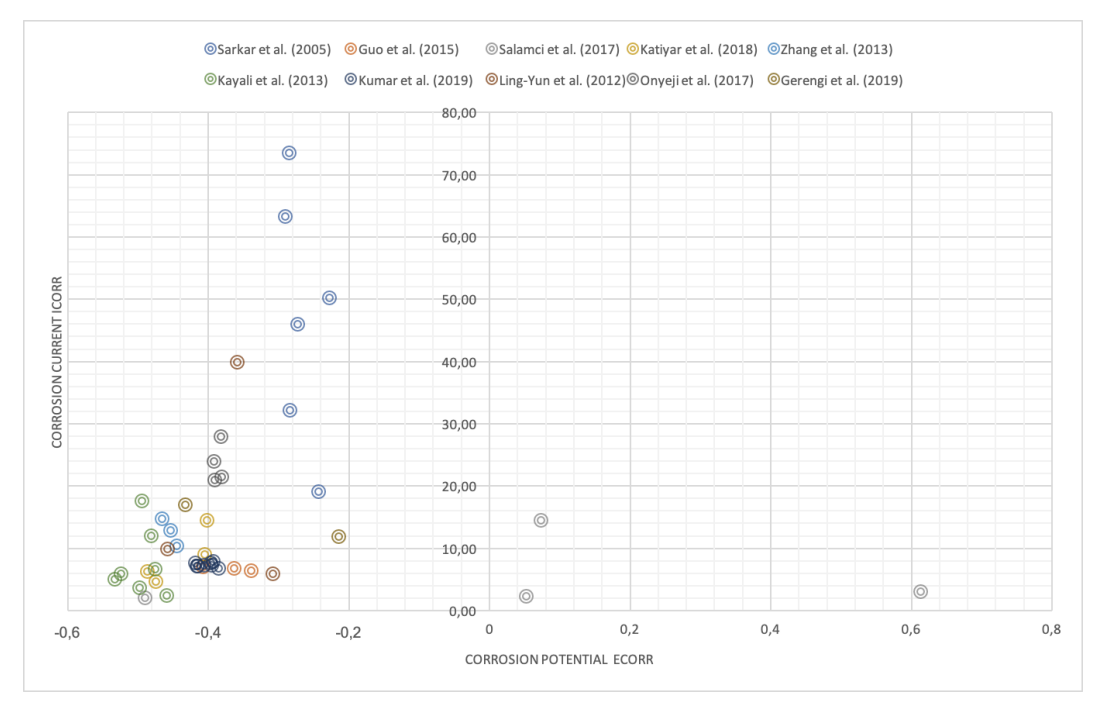
In the previous section, individual microstructural behaviours and effects on corrosion resistance are attempted to be explained. It is seen that there is a wide difference of opinion in literature on the effects of microstructural features. That arises from the intrinsic nature of the phenomena. When dealing with heat treatments

and thermomechanical processes and the resulting microstructures, not individual features but a whole array of properties change. Literature usually attributes the outcomes of corrosion experiments to specific features, neglecting or disregarding the effects of others.

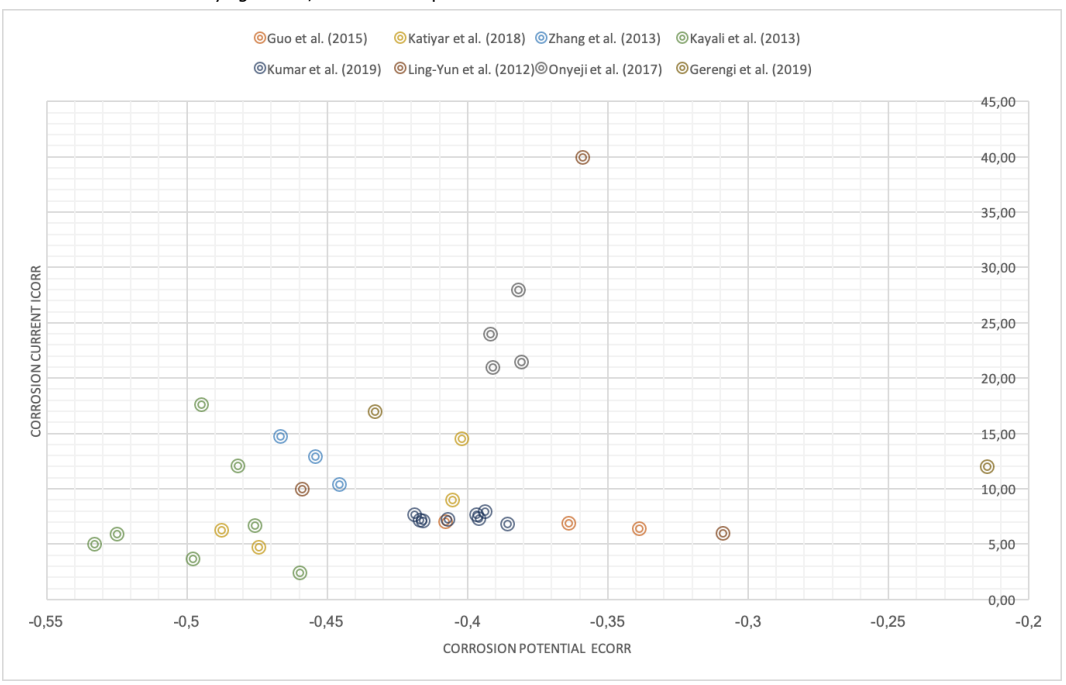
For instance during a grain refinement process, a decrease in average grain size is naturally accompanied by an increase in grain boundary area, but if the structure is a multi-phase structure that has dedicated anode and cathode phases, the fraction of interphase interfaces to grain boundaries could be important. Due to the experimental limitations this has not taken into account in the papers analysed for this review. With a decrease in grain size, low-angle grain boundary fraction will also change together with corrosion response, as misorientation of the grains also impacts the corrosion resistance. The amount of segregation of impurities will most likely change with different grain size, changing the electrochemical state between boundaries and grains themselves. In the same vein, depending on the procedure residual stresses will change which will modify the work function of the external oxide layer and may increase the defect concentration. If there is external load during a refinement process, oxide layer may increase in defect density even further by the contribution of plastic deformation and introduced crystallographic texture. Depending on the kinetics and thermodynamics of different phases during the refinement procedure, volume fractions of the phase constituents may also change together with size and distributions of inclusions, resulting in a new anode/cathode area distribution. The combination of such microstructural features makes it substantially hard to decouple the entangled individual effects on corrosion behaviour; with every thermal process, there will be many significant microstructural changes that result in distinct corrosion behaviour.

To take a step back from the individual analysis of microstructural features, an overall comparison of literature is undertaken to discern an emerging trend. The polarisation data from samples that show an active corrosion behaviour is collected in table A.1. A summary of the microstructure details, volume fraction of constituent phases, carbon content, electrochemical test environment, corrosion potential and corrosion current is provided. Alloying elements also have a considerable effect on corrosion behaviour and are not included in the table as the composition varies widely. This is one of the main limitations, it is not scientifically rigorous to compare different chemical compositions. Assuming the contribution of micro-alloying won't be the dominant effect in determining the corrosion response, it is still hard to compare the specimens from different papers. There are too many free parameters, either because of the differences in experimental setup or the previously mentioned effect of coupled microstructural features. To see the distribution of data and to generate a sense of magnitude of this ambiguity, the corrosion potential and corrosion current data of polarisation experiments carried out in the same 3.5 wt.% NaCl environment is taken from table A.1 and plotted as a scatter graph in figure 1.14.

Figure 1.14a shows that there is a large scattering of the data, both for corrosion potential and corrosion current. Data tended to cluster in one area but some data points spread noticeably. Overall difference in corrosion potential is examined to be



(a) Notice the wide spread in i_{corr} and E_{corr} . The span of the data of Sarkar et al. [13] and Salamci et al. [16] may indicate a different underlying source, such as an experimental artefact.



(b) A focused version of figure 1.14a. The outliers are taken out to make the underlying relationship more visible.

Figure 1.14: A collection of corrosion potential and corrosion current data acquired from the polarisation experiments carried out in the 3.5 wt.% NaCl environment.

more than 1 V and the difference in corrosion current is detected to be more than 70 $\mu A/cm^2$. These numbers are too large to be the product of the microstructure. It must be related to the experimental setup or an external parameter.

This highlights the necessity for a more formal, streamlined corrosion research system. The most utilised techniques in reviewed literature were weight loss methods, polarisation experiments and electrochemical impedance spectroscopy. However, most of the time researchers did not supply information on the specifics of how they carried out the experiments. For instance, corrosion potential of martensite-ferrite samples in a pH 8.4 boric acid-borate solution is different whether the potential is measured directly after polish or measured after galvanostatic reduction [49]. Most of the cases, such details are not provided. Cases such as these introduce ambiguity into research, and make a rigorous cross-comparison between individual studies unattainable.

Figure 1.14b shows a more focused account of the polarisation data by removing the outliers. In this case the spread of data is much narrower, corrosion potential differs less than 0.35 V while corrosion current differs less than 40 $\mu A/cm^2$. These results show more promise of displaying the effect of the microstructure. Still, clustering of the data of individual papers contrary to the wider overall spread in results, emphasises the requirement of a more formal corrosion testing procedure.

The examination of the data used to plot figure 1.14b from table A.1 shows the difficulty of comparing different microstructures. Volume fractions, phase constituents, phase morphology, chemical composition change at the same time, as well as the experimental specifics between different papers. This eliminates instances with straightforward comparisons such as clearly understanding the effect of martensite volume fraction, and furthermore produces inconsistencies.

To have a better understanding of individual effect of microstructural features, special attention must be paid to have one or least amount of free parameters changing with the modification of the microstructure. It is very important for future corrosion research to create methods to study individual microstructure features separately and standardise corrosion research to enable the accurate comparison of data. It is hoped that this will lead to a deeper understanding of the effect of microstructure on corrosion behaviour of HSLA steels.

1.6. Research Approach and Thesis Focus

The aim of this thesis is to demonstrate the effect of different phase constituents on the electrochemical response of high strength steels. Literature often reports contradictory results about the effect of microstructure on the corrosion behaviour. This arises from the complex coupling between different microstructural features. For example, when one changes the volume fraction, often other properties of the microstructure change such as the dislocation density and the carbon concentration of the individual phases. This complex behaviour make the isolation of distinct contribution of the microstructural features difficult.

To untangle this complex behaviour, a computational and an experimental approach is taken. On the computational side, the electrochemical corrosion behaviour of a two phase structure is modelled with a finite element model. The difference be-

34 1. Background

1

tween idealised behaviour of the model and experimental results from the literature is highlighted to display the features of the microstructure that control the corrosion behaviour. On the experimental side, a selection of different microstructures are prepared with different heat treatments. Out of these, a ferrite-martensite (FM) and a ferrite-pearlite (FP) dual phase microstructure with equal ferrite volume fraction are selected for further electrochemical analysis. The electrochemical analysis took place in acidic (H_2SO_4) and basic (NaOH) electrolytes to measure to corrosion response in both active and passive conditions. The demonstration of phase-environment interaction for microstructures with different phase combinations underlines the impact of phase constituents on the corrosion behaviour.

2

Modelling

Mathematical modelling and computational simulations are important tools in aiding the understanding of many different physical and chemical phenomena. These tools can be used to explore the mist that surrounds the corrosion behaviour as well.

The use of computational models in corrosion research is not a rare sight. Models that incorporate finite element analysis, phase field modelling and others have been utilised in various corrosion investigations. On macro scale, galvanic corrosion has been investigated using adaptive level-set method [66, 67] and finite element analysis [68, 69] to give insight about the evolution of the corrosion surface. On micro scale, various aspects of localised corrosion have been investigated in great detail. Micro-galvanic corrosion between different phases has been modelled as a random assignment of anodic and cathodic regions [70, 71], simulated using a level-set method [72] and the resulting corrosion product deposition mechanism have been examined by simulations [73]. Anodic dissolution of intermetallic particles has been analysed with respect to the particle size [74]. Pitting initiation is studied by simulation of polarisation curves and surface morphology [75]; the effect of pit size and pH [76] and the effect of crystallographic orientation on pitting [77, 78] are studied through finite element analysis. Multiscale corrosion modelling has been used to incorporate different size scales together [79]. Analytical electrochemical techniques such as potentiodynamic polarisation [71, 75] and scanning electrochemical microscopy [80] have also been recreated digitally.

Modelling corrosion requires a method of solving partial differential equations (PDE) that describe the electrochemical behaviour. Finite element analysis is a general method that is perfectly suited in solving those PDEs to start designing a basic corrosion model. For this reason, and the physical nature of the problem that couples electrochemistry, diffusion and other physical fields with increasing model complexity, COMSOL Multiphysics is utilised in creation of corrosion models in this thesis.

The aim of creating a finite element simulation is to demonstrate the microgalvanic coupling between ferrite and secondary martensite/pearlite phases by 36 2. Modelling

changing ferrite volume fractions. This will demonstrate the idealised isolated effect of the volume fraction on corrosion behaviour for different phase combinations.

2.1. Modelling Approach

The model is intended to simulate the behaviour of a multi-phase microstructure. Experimental creation of microstructures with precise volume fractions is problematic - many different factors couple together during heat treatments to generate the end result. There might be inherent limitations as well, for example overall carbon content of the steel will limit the formed pearlite after heat treatments. For this end, creating simplified digital microstructures is highly rewarding in exploring the micro-galvanic corrosion behaviour.

The creation of digital microstructures with different volume fractions is particularly difficult, as in the real world grains with different sizes, crystallographic orientations and geometric positions coexist together. To simplify this problem, focus is given on the dual phase microstructure. The impact of different crystallographic orientation and grain boundaries is not explicitly modelled due to the implicit assumption that our electrochemical input values will carry the weights of these factors in them as well. Model is designed to be formed of a cathode and an anode area, with periodic boundary conditions that imitates the grains repeating one after another. Model details are illustrated more explicitly in section 2.3.

Electrochemical parameters are taken from the polarisation curves of Fushimi et al. [37] for ferrite-martensite microstructure and from the experiments of Aytaç Yılmaz of TU Delft for the ferrite-pearlite microstructure. Fully ferrite, martensite and pearlite microstructures are used as input for phases. For ferrite-martensite microstructure, polarisation results for in between volume fractions are used to calibrate the model and check its accuracy. The behaviour of ferrite-pearlite microstructure is interpolated accordingly.

2.2. Theory

An electrochemical system is made up of two main components: electrode and electrolyte. Electrode conveys the current by transfer of electrons and the electrolyte mainly carries current by transport of charged chemical species; electrolyte's electrical conductivity is orders of magnitude lower than the electrical conductivity of the electrode. At the electrode-electrolyte interface, electrical current of the electrode is transformed into the ionic current of the electrolyte with respect to the overall charge conservation.

A system of two electrodes with different electron affinities, in the case of corrosion electrochemistry this could be two different phases of the same metal, creates a circuit when the electrodes are in contact with an electrolyte. This forms an electrochemical cell. Of the two electrodes, anodic and cathodic roles are assigned according to the electron affinities and a flow of current is formed: electrical current from the cathode to the anode and an ionic current by the transport of ions at the electrolyte from anode to the cathode.

Corrosion modelling requires careful analysis of the state of electrochemical re-

2

actions. Two main types of reactions are required to be considered: heterogenous electrochemical reactions at the electrode-electrolyte interface and homogenous chemical reactions that take place in the electrolyte. Heterogenous reactions can be introduced through boundary conditions at the metal interface. Homogenous reactions can be introduced through the knowledge of possible reactions in solution and their reaction rates. Ohmic loss caused by the electrolyte, electrode kinetics and mass transfer are all important parts of the problem. The coupled nature of different physics make this a complex multiphysics problem.

The mass transport of charge carriers in the electrolyte is given by the Nernst-Planck relation:

$$N_i = -D_i \nabla c_i - z_i F \frac{D_i}{RT} c_i \nabla \varphi + c_i \vec{v}$$
 (2.1)

where N_i is the ionic flux density, D_i the diffusion coefficient, ∇ the gradient operator, c_i the concentration of the ith species, z_i the number of electrons involved in the reaction per ion, F Faraday's constant, R gas constant, T temperature, φ the electrostatic potential and \vec{v} the solvent velocity. The first, second and third terms of the equation respectively represent the diffusion, migration and convection mode of charge transport. The change of concentration of a charged species i with time is:

$$\frac{\partial c_i}{\partial t} = -\nabla N_i + R_i \tag{2.2}$$

where R_i is the chemical reaction rate.

Electroneutrality condition:

$$\sum_{i} z_i c_i = 0 \tag{2.3}$$

is used to determine the electric potential in Nernst-Planck equations, where current flow is given by:

$$i_l = \sum_i z_i F N_i \tag{2.4}$$

where i_l is the current flow through the electrode-electrolyte surface. If the composition of the electrolyte can assumed to be constant and charged ions are not depleted around the electrode, this further simplifies to:

$$i_l = -\sigma_l \nabla \varphi_l \tag{2.5}$$

where σ_l is the conductivity of the electrolyte. As long as it stays constant, the above derivation is a valid approximation.

The material balance combined with the kinetics and thermodynamics constraints such as Faraday, Nernst and Butler-Volmer equations succintly summarised in section 1.2 forms the backbone of the electrochemical model of corrosion. To implement the galvanic corrosion, it is realised that galvanic corrosion is practically equivalent to a short circuit of two electrodes with different electron affinities. The potential of both electrodes have to be the same in order to create this short circuit.

38 2. Modelling

2.3. Implementation

The combined multiphysics problem of corrosion was solved iteratively with the finite element modelling through COMSOL Multiphysics. The aim was to examine the effect of volume fraction. For this end, the dual phase structure was selected to be analysed due to it's widespread usage in the industry.

Experimental analysis of the volume fraction of phases is not a simple endeavour. Same phases can contain different amounts of carbon and dislocation densities may also be different. Intermetallics can initiate pitting, morphology and size of the grains may be different from each other. Therefore even though two phases may be the same, the difference in overall microstructure will generate different corrosion responses. To get rid of this complexity, two distinct zones are defined in this simulation: an anodic and a cathodic zone with persistent electrochemical properties. At first this may be seen as a drawback of the model, as it gets rid of much of the complexities and nuances of real life, but in fact it allows isolated analysis of the volume fraction. In this simulation, changing volume fractions do not cause other complexities (e.g. decreasing volume fraction of martensite resulting in an increase in the dissolved carbon in the martensite phase) to arise. It allows a clear analysis of the volume fraction. The difference between the results of the simulation and experiments can be analysed to further illuminate the effect of other changing features of the microstructure, enabling the discovery of the dominant force in the corrosion behaviour.

To this end, a simple approach was chosen. An anodic and a cathodic zone and the micro-galvanic interaction between them was the focus of the model. The corrosion was driven by the potential difference between the phases and resulted in different corrosion responses because of their different corrosion kinetics. The input parameters were the pure phases taken from the literature and previous experiments done at TU Delft: 100% ferrite, martensite and pearlite.

Model Geometry and Boundary Conditions

Model geometry and an example simulation result is shown in figure 2.1. 2D geometry was chosen to decrease the simulation time but more importantly to allow setting up microstructures with different volume fractions. There is no general solution for changing the volume fraction in 3D case, a model geometry has to be created from actual microscopic images for every target volume fraction, which brings its own biases into the picture as the arrangement of grains and their different sizes will also be affecting the corrosion behaviour. Idealised 2D picture allows identifying the effect of volume fraction alone.

To make the simulation more realistic, left and right edges were assigned with periodic boundary conditions:

$$\varphi_{left} = \varphi_{right} \tag{2.6}$$

$$\hat{n} \cdot (\sigma \nabla \varphi)_{left} = -\hat{n} \cdot (\sigma \nabla \varphi)_{right} \tag{2.7}$$

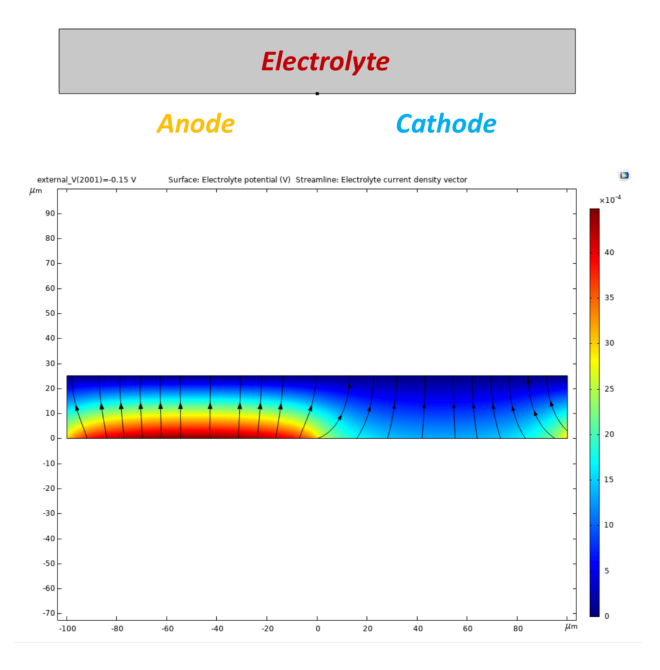


Figure 2.1: 2D model geometry and example simulation for 50% ferrite 50% martensite potentiodynamic polarisation.

which virtually make the simulation act as if left part of the geometry continues from the right part. Any current that leaves the system from the left enters from the right.

Equations 2.6 and 2.7 force the lateral edge boundary condition that the potentials for left and right boundaries are the same, and the current flow normal to the left boundary is opposite of the right. This is the case for both the electrode and the electrolyte boundaries.

Two different style of simulations required different boundary conditions. During *free corrosion* simulations upper boundary is insulated:

$$\hat{n} \cdot i = 0 \tag{2.8}$$

resulting in zero normal current density in upper boundary. This was done to replicate the open circuit potential (OCP) determination. After determination of OCP, a *potentiodynamic polarisation* is simulated by varying the potential at the bottom boundary, the working electrode. This creates a virtual counter electrode at the upper boundary.

OCP example can be seen in figure 2.2, polarisation example in figure 2.1. Corrosion potential and OCP were found to be virtually identical, therefore from now on only polarisation simulations are taken into consideration.

40 2. Modelling

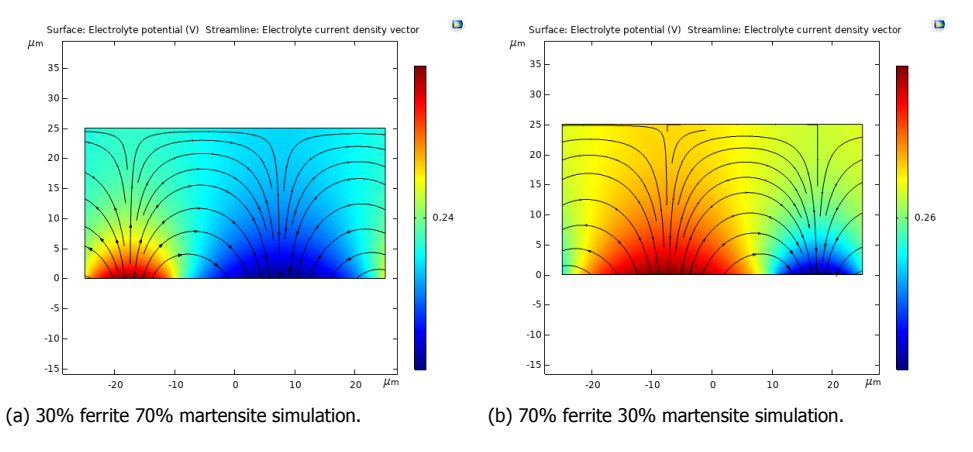


Figure 2.2: Example free corrosion simulations for OCP determination.

Input Parameters and Reactions

Fushimi et al. [37] mentions that in their experiments the dimensions of the working electrode probe used for potentiodynamic polarisation sweep was 50 μm by 50 μm . This probe is replicated by appropriately setting up the simulation geometry. Accordingly, simulation dimension was chosen as 50 μm in length, 25 μm designated for the anodic area and 25 μm designated for the cathodic area. The depth of the simulation is fixed to be 50 μm . Height of the electrolyte was chosen to be half the length of the simulation. Electrolyte conductivity was defined to be isotropic and a suitable value to simulate 0.1M sulphuric acid solution was selected. Two electrode reactions were considered for each electrode. Electrode reactions were set to be the iron dissolution reaction and the hydrogen evolution reaction. Their kinetic expressions were defined to be anodic and cathodic Tafel equations.

Two set of input parameters were used in the described model. One was to simulate the ferrite-martensite microstructure and the other was to simulate ferrite-pearlite microstructure. Input for the ferrite-martensite microstructure was taken from the paper of Fushimi et al. [37]. Input for the ferrite-pearlite was taken from the previous electrochemical experiments done by Aytaç Yılmaz. The electrochemical inputs consisted of the corrosion current density, corrosion potential, anodic and cathodic Tafel slopes of the pure ferrite and martensite cases for the ferrite-martensite model, and pure ferrite and pearlite cases for the ferrite-pearlite model. The parameters for both these cases are shown in appendix B.

The data of Fushimi et al. [37] was used to calibrate and check the model, as in-between experimental values for 25% ferrite 75% martensite, 50% ferrite 50% martensite and 75% ferrite 25% martensite were also known.

3D Model

A 3D model was also generated to compare and contrast the 2D and 3D model. The design idea was similar to the 2D case with same input parameters, reactions and boundary conditions. Only difference between the two cases was that instead

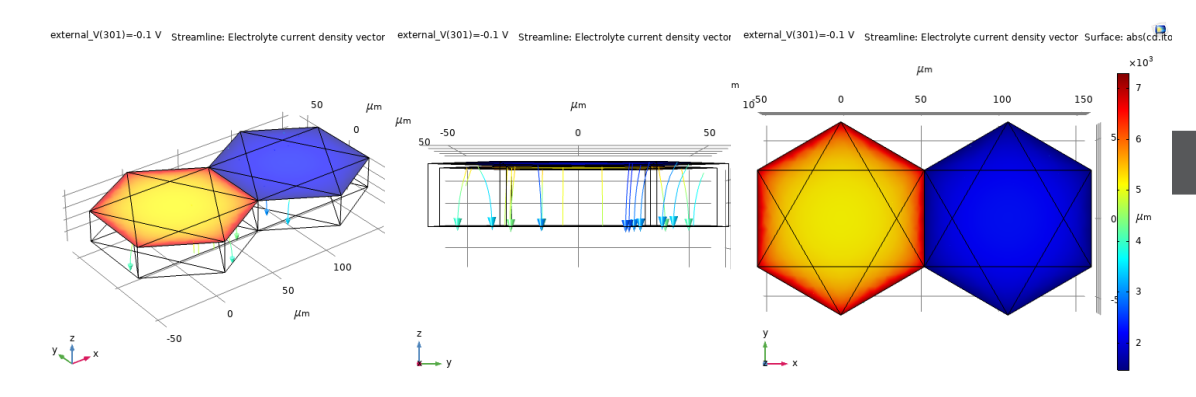


Figure 2.3: A 3D simulation with hexagonal geometry and periodic boundaries with 100 μm grains.

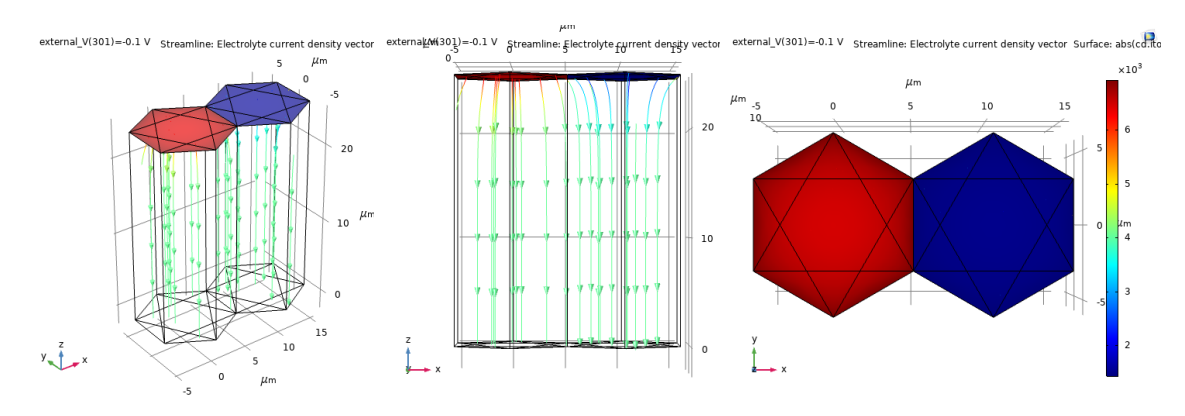


Figure 2.4: A 3D simulation with hexagonal geometry and periodic boundaries with 10 μm grains.

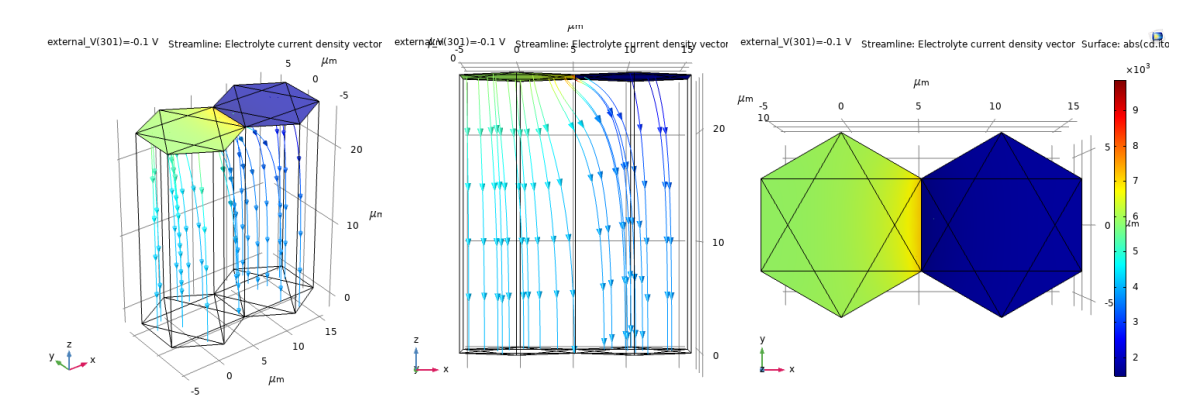
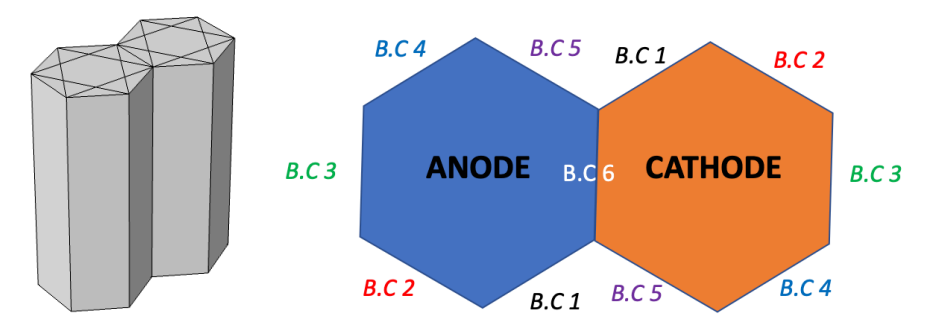


Figure 2.5: A 3D simulation with hexagonal geometry and non-periodic insulated boundaries with 10 μm grains.

42 2. Modelling



(b) Periodic boundary conditions in 3D.

(a) 3D model geometry.

Figure 2.6: Geometry and boundary conditions for the 3D simulation set.

of linear lamellar grains of the 2D case, two hexagonal grains in 3D were used to represent ideal grain surfaces. In the 2D case, the depth is constant, and the microstructure geometry is a lamellar structure that spans indefinitely. Anode lamellae are surrounded by cathode lamellae. In the 3D case, the microstructure geometry consists of hexagonals bordering other hexagonals. The model geometry and periodic boundary condition set up is shown in figure 2.6.

Top layer represents the electrode surface and the hexagonal column the electrolyte surface. Periodic boundary conditions were applied the same way as it is done for the 2D case, but instead of the two lateral boundaries hexagonal geometry provides 5 outer (B.C 1-5) boundaries and 1 inner/shared(B.C 6) boundary. Boundaries from opposite edges were selected as shown in figure 2.6b and imposed to have same potential and opposite current flows as done in 2D simulations. This creates a microstructure where anode is surrounded by cathodes all around and cathode is surrounded by anodes all around. This virtually generates a worst-case scenario as all boundaries are forced to be anode-cathode boundaries.

To test the non-periodic condition another simulation set was also created by insulating external boundaries (B.C 1-5) with no current flow condition. The difference between the two cases showed that less current density is observed in non-periodic conditions. That makes sense as it produces a less realistic case where all boundaries of the grains but one is insulated.

An overview of 3D simulations are demonstrated in figures 2.3, 2.4 and 2.5. The change in behaviour between periodic and non-periodic boundary conditions becomes clear when figures 2.4 and 2.5 is compared. For the non-periodic simulation, micro-galvanic interactions and resulting current flow is apparent only in the shared boundary of grains. For the periodic boundary conditions, the activity of every grain boundary is visible. Comparison of grain sizes reveal that larger grains tend to have more difference between the centre of the grain and the boundaries. This makes sense as grain boundary areas would be interacting and the microgalvanic behaviour would be manifested more dominantly.

Table 2.1: Provisional simulation summary for subsequent volume fraction analysis.

| Simulation Style | Changes From Simulation Set 1 | Average Current Density |
|------------------|--|-------------------------|
| 2 | Electrolyte conductivity is changed from 5 to 3 S/m. | Decreases |
| 3 | Electrolyte height has reduced to one fourth of its original value. | Increases |
| 4 | Electrolyte height has doubled to its original value. | Virtually no change |
| 5 | Doubled the simulation length and electrolyte height. | Decreases |
| 6 | Doubled the simulation length to simulate a larger grain with a grain size of 50 micrometers. | Decreases |
| 7 | Halved the simulation length to simulate a smaller grain with a grain size of 10 micrometers. | Increases |
| 8 | Doubled the simulation length to simulate a larger grain with a grain size of 100 micrometers. | Decreases |
| 9 | 3D simulation with non periodic B.C. that represents 10 micrometer grains. | Increases |
| 10 | 3D simulation with periodic B.C. that represents 10 micrometer grains. | Increases |
| 11 | 3D simulation with periodic B.C. that represents 20 micrometer grains. | Increases |
| 12 | 3D simulation with periodic B.C. that represents 100 micrometer grains. | Increases |

Simulation Summary

According to the conditions mentioned in this section, a set of simulations with different setups were created. They were studied to identify the most suitable conditions to analyse the effect the volume fraction. *Simulation 1* is the final selected conditions that use the parameters in appendix B. Succeeding volume fraction analysis for different microstructures were done in that style. Other trial simulations and the trend in average current density is summarised in table 2.1. Maximum change in current densities between the simulation styles were established to be less than 1%. Therefore the use of 2D simulation with current conditions is determined to be suitable for subsequent analysis.

Comparison of different simulation sets show that even in this simplified picture, smaller grain sizes result in increased corrosion. As the grain sizes decreased, both in 2D and 3D simulation sets, the current density increased. Although the change is small, it must be noticed that this analysis is based on the solution of electrochemical equations only. The model disregards the contribution of electrochemical properties of grain boundaries that exacerbates corrosion. Electrolyte height had almost no effect, and the decrease in conductivity limited corrosion. Analysis of 3D hexagonal geometries have shown that in this micrometer scale the difference between 2D and 3D is not discernible.

Experimental Procedure

Careful testing and reflection is key in illuminating any scientific phenomena. To analyse the effect of phase combinations on the corrosion behaviour of high strength steels, analysis of individual phases and their interaction is key.

For this investigation, a model alloy with a dual phase microstructure is aimed to be created. By keeping the common phase volume fraction constant with controlled heat treatments, a ferrite-martensite and a ferrite-pearlite microstructure with same ferrite volume fractions were generated. After the microstructure creation, various electrochemical experiments were carried out to investigate the active corrosion response and passive layer properties of these microstructures. The details of these experiments and the microstructure creation process are elaborated on this chapter.

3.1. Microstructure Characterisation

3.1.1. Material

After comparing various commercially used steels, TATA Steel IJmuiden produced DP1000 was chosen as a base to start the microstructural design. DP1000 was selected because of its low alloyed chemical composition that permits dual phase microstructure formation. The composition was also appropriate for eliminating the effect of inclusions such as MnS on electrochemical experiments. The chemical composition of DP1000 is presented in table 3.1. As-received 2 mm thick steel sheets that were laser-cut to 5 x 10 mm² samples were the starting point for the rest of the experiments. Initial sample microstructure of ferrite and martensite phases is displayed in figure 3.1.

Table 3.1: Chemical composition (wt.%) of DP1000 steel samples.

| С | Si | Mn | P | S | Al | Cr | Cu | Мо | N | Ni | Sn | Ti | Ca | V | В |
|-------|-------|-------|-------|-------|-------|-------|-------|-------|---|-------|-------|-------|-------|-------|---|
| 0.141 | 0.051 | 2.149 | 0.013 | 0.014 | 0.041 | 0.576 | 0.012 | 0.004 | - | 0.021 | 0.001 | 0.032 | 0.022 | 0.007 | - |

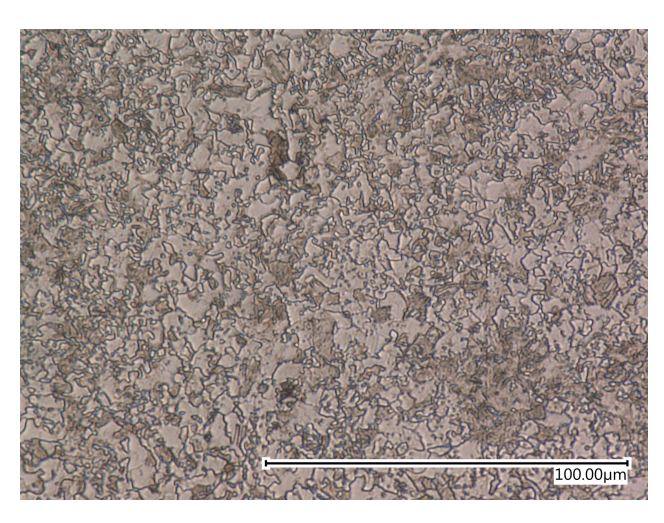


Figure 3.1: Initial microstructure of DP1000 steel after etching it with OPS and 2% Nital etchant. White regions are ferrite and grey regions are martensite phases.

3.1.2. Dilatometry

A Bähr DIL 805 A/D dilatometer was utilised to perform various heat treatments. To monitor the temperature and to control the heat processes that the sample undergoes, a platinum thermocouple was attached to the sample via a spot weld. Precision heating was achieved with the help of an induction coil and precision cooling was achieved with the help of helium gas flushed into the vacuum chamber.

The heat treatments were designed to produce dual phase microstructures with different volume fractions and phase combinations. Prior to the selection of actual heat treatments, initial DP1000 microstructure was annealed up to 1000 °C for 10 minutes and quenched rapidly to determine the Ac_1 , Ac_3 , M_s and M_f temperatures. This was repeated for 3 different samples to ensure reproducibility. For a specified heating rate austenite transformation starts at Ac_1 and finishes at Ac_3 ; for a specified cooling rate martensite transformation starts at M_s and finishes at M_s . These temperatures depend on the kinetics of the heating/cooling processes and they are important in designing the subsequent heat treatments. They are presented in table 3.2.

Table 3.2: Critical temperatures for the subsequent heat treatments of DP1000 dual phase steel.

| Ac_1 | Ac_3 | M_{S} | M_f |
|--------|--------|---------|--------|
| 720 °C | 840 °C | 400 °C | 140 °C |

The overall heat treatment summary can be seen in figure 3.2. The applied heat treatments were similar to the ones employed by Fushimi et al. [37], which resulted in ferrite-martensite dual phase microstructures with 50% ferrite volume fraction. The heat treatments were initiated by full austenisation of the initial microstructure

at 1000 °C for 30 minutes. Afterwards, samples were step quenched to an intercritical heat treatment temperature and annealed for 15 minutes. For the last step, samples were either directly quenched after the intercritical annealing procedure or held isothermally at sub- Ac_1 temperatures for up to 2 hours.

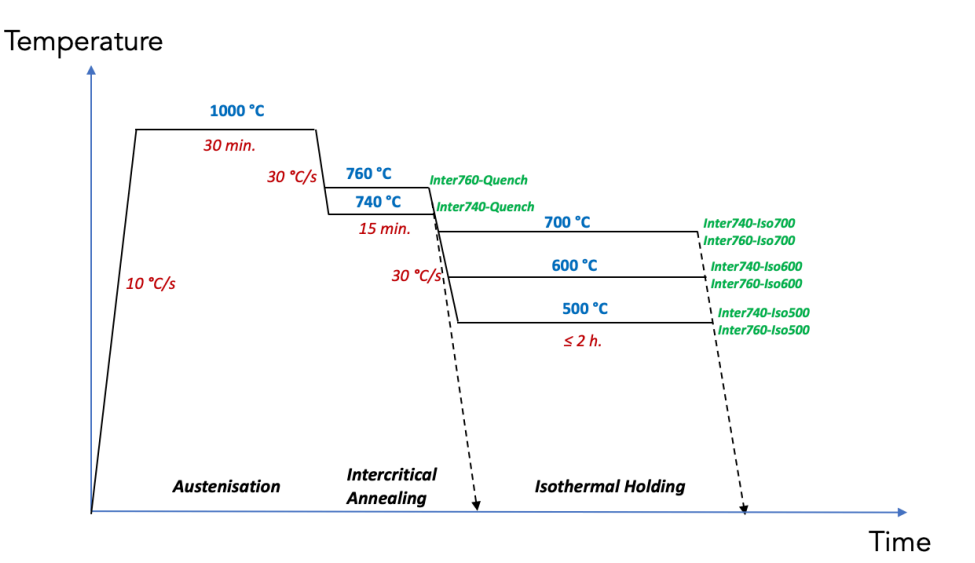


Figure 3.2: Graphical summary of the employed heat treatments. *Inter* prefix is used to denote the intercritical annealing, *Iso* prefix is used to denote the isothermal holding heat treatment steps. Successive numbers indicate the temperature of the applied heat treatment step.

The dual phase microstructure was generated through intercritical heat treatments between Ac_1 and Ac_3 temperatures. In this temperature range, part of the austenite stabilises into ferrite. Since the austenite only partially transforms into ferrite, rest of the austenite phase can be transformed into other phases with subsequent heat treatments.

The intercritical transformation temperatures were chosen as close to the Ac_1 , 740 °C and 760 °C, as the pearlite transformation is harder in a chemical composition with such low carbon percentage. It was seen through time-dilatation transformation plateau that the transformation in the intercritical annealing step was complete under 15 minutes, therefore chosen duration was adequate for the stabilisation of the ferrite-austenite structure. Isothermal holding treatments up to 2 hours were employed to enable the formation of a thermodynamically stable phase such as pearlite. The isothermal heat treatments were stopped when the transformations to the final microstructures were complete.

3.1.3. Sample Preparation

The microstructures obtained from different heat treatments were prepared for microscopy and hardness examinations. For further microstructure characterisation, the samples were first embedded in a Struers ClaroCit epoxy resin and cured for

 $1\$ hour under $2\$ bar pressure. After the epoxy was hardened, the samples were ground with moist SiC sanding paper from $80\$ to $4000\$ grit. The samples were subsequently polished using a Struers DiaDuo-2 fine diamond suspension with $3\$ and $1\$ µm particle sizes. Finally, the samples were ultrasonically cleaned in a bath with ethanol for $10\$ minutes after polishing, and dried with compressed air. The samples were etched with a 2% nital etchant solution to reveal the microstructure. Etching time changed between $15\$ seconds to $1\$ minute depending on the microstructure.

3.1.4. Investigation of the Microstructure

The microstructures of different heat treatments were analysed with microscopy and hardness measurements.

Optical Microscopy and SEM

A Keyence VHX-500 optical microscope was used to characterise the overall microstructure from the optical micrographs. The features of the secondary phases were analysed in more detail with a Jeol JSM-IT100 scanning electron microscope. The phase constituents and volume fractions of respective phases were determined through the micrographs. ImageJ software was used for calculating the volume fraction of the phase composition.

Vickers Microhardness

Vickers microhardness measurements were employed for the microstructural analysis of the phases. A series of hardness tests were exercised at the HV 0.01 scale. At this scale, the force was low enough to test the hardness of individual phases. Measurements were repeated 3 times for each phase constituent. A Struers DuraScan 70 microhardness tester and Ecos Workflow software were used to carry out the hardness measurements.

3.2. Electrochemical Analysis

Out of the 8 prepared samples resulting from different heat treatments, 2 was selected for further electrochemical analysis: a ferrite-martensite (FM) and a ferrite-pearlite (FP) sample. These samples had similar volume fractions of 50% but consisted of different phase combinations. The samples with similar ferrite volume fractions were compared so that the effect of cathode fraction on the corrosion behaviour would be minimised and the dominating effect would be the contribution of the phase combinations.

3.2.1. Sample Preparation

Type-K chromel-alumel micro thermocouple was spot welded on the surface of the samples. This was prepared so that the circuit will be complete during the electrochemical experiments. The thermocouple wire allowed the sample to maintain electrical contact with the potentiostat as the working electrode. Embedding, grinding and polishing steps used for the microstructure characterisation were repeated to obtain a mirror-like polished surface ready for electrochemical experiments. The steel-resin boundaries were coated with a thin layer of insulating Electrolube BLR

lacquer to prevent possible crevice corrosion during the experiments. The sample preparation steps were repeated between electrochemical tests. An example completed sample is shown in figure 3.3.



Figure 3.3: An example completed sample ready for electrochemical experiments.

3.2.2. Electrochemical Setup

A Biologic VSP-300 potentiostat was used in combination with a three electrode electrochemical cell setup for the electrochemical experiments. The setup utilised stainless steel mesh as the counter electrode, the sample as the working electrode and Ag/AgCl (saturated KCl) as the reference electrode. EC-lab v11.33 software was used for controlling and analysing the electrochemical measurements. The setup was placed in a Faraday cage before initiation of electrochemical tests to shield it from external electromagnetic noise. Experiments were conducted at room temperature. The electrochemical setup is displayed in figure 3.4.

3.2.3. Active Behaviour Experiments

Electrochemical experiments were carried out in an acidic electrolyte to assess the role of ferrite-martensite and ferrite-pearlite microstructures on the active corrosion behaviour. Deaerated H_2SO_4 solution was selected as the test environment due to the absence of $\mathcal{C}l^-$ ions in the solution that initiate pitting corrosion. A 0.1M H_2SO_4 pH 1.0 solution was prepared with Milli-Q ultrapure water. To see the effect of the environment, the prepared solution is diluted to one tenth of its original concentration after first round of experiments. The pH of the diluted H_2SO_4 solution was measured to be 1.9.

The deaeration of the solutions was achieved through nitrogen bubbling. The solutions were poured into a beaker and were covered with a Parafilm M laboratory

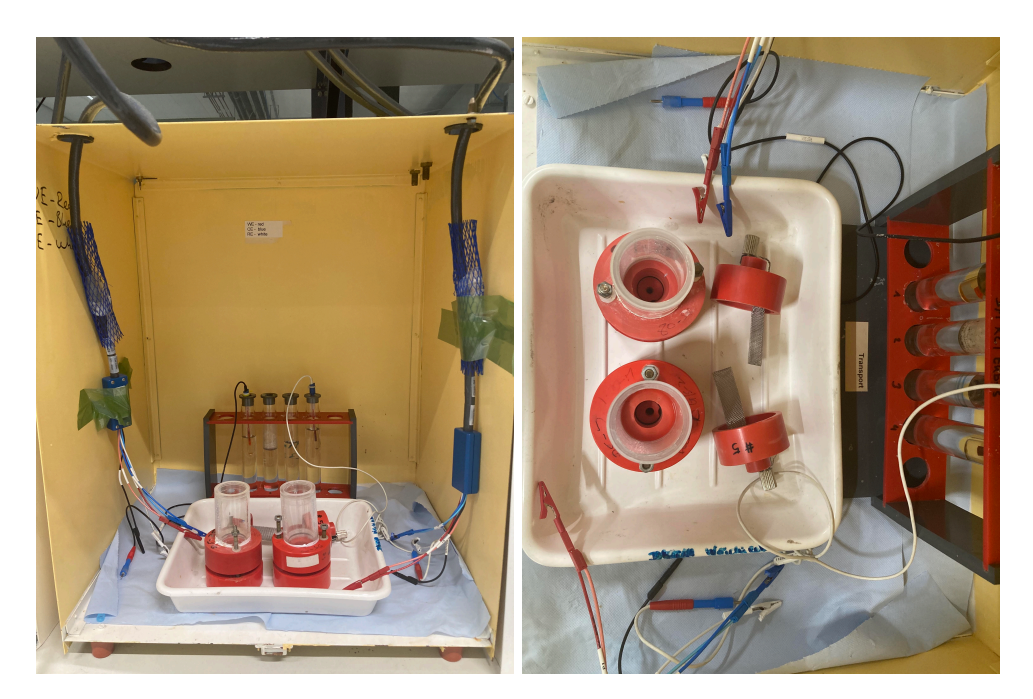


Figure 3.4: Electrochemical cell setup.

film. Subsequently, solution was deareated through bubbling it with nitrogen for 1 hour before the electrochemical experiments.

Corrosion experiments were initiated by measuring the open circuit potential, then the corrosion resistance was measured with electrochemical impedance spectroscopy, and finally corrosion response of the samples were analysed through potentiodynamic polarisation. All electrochemical tests were repeated 3 times in each environment to verify the reproducibility of the experiment results.

Open Circuit Potential

Open circuit potential (OCP) of the samples were recorded for 1 hour. The potentials had stabilised in this period.

Electrochemical Impedance Spectroscopy

With the samples at OCP, electrochemical impedance spectroscopy (EIS) was utilised to measure the different active electrochemical responses of the ferrite-martensite and ferrite-pearlite microstructures. EIS measurements were carried out by exerting an alternating current (AC) perturbation in the frequency range of 10 mHz to 30 kHz with a 10 mV peak-to-peak amplitude.

The Zview 3.5h software is used to fit the experimental EIS data into equivalent electrical circuits for a quantitative comparison of microstructures.

Potentiodynamic Polarisation

Potentiodynamic polarisation was employed to determine the effect of ferrite-martensite and ferrite-pearlite microstructures on the corrosion response on the system. The samples were polarised in a potential range between -0.25 V to 0.25 V with respect to the OCP. The chosen scan rate was 0.167 mV/s.

Corrosion potentials were determined from the polarisation plots as the potential values where the current densities approach to a minimum. Corrosion current densities were calculated through drawing Tafel tangents from the more linear parts of the polarisation curves, \pm 50 mV from the corrosion potentials.

3.2.4. Passive Behaviour Experiments

Electrochemical experiments were carried out in an alkaline electrolyte to assess the barrier properties of the passive oxide layers of ferrite-martensite and ferrite-pearlite microstructures. The chosen environment was an aerated NaOH solution, which was widely used in literature to create passive films on steels. A 0.1M NaOH solution was prepared with Sigma-Aldrich NaOH pellets and Milli-Q ultrapure water. The pH of the solution was measured to be 12.6.

Passivity experiments were initiated by measuring the open circuit potential, then a passive oxide layer was created through potentiostatic polarisation, subsequently electrochemical impedance spectroscopy was utilised to measure the corrosion resistance of the created oxide layer, and finally capacitance measurements of the passive oxide layer were employed. All electrochemical tests were repeated 3 times to verify the reproducibility of the experiment results.

Open Circuit Potential

Open circuit potential (OCP) of the samples were recorded for 1 hour. The potentials had stabilised in this period.

Potentiostatic Polarisation

After the OCP measurements, a passive oxide layer was created on the samples by applying potentiostatic polarisation at 0.2 V for 6 hours.

Electrochemical Impedance Spectroscopy

The corrosion resistances of the developed oxide layers were analysed through electrochemical impedance spectroscopy (EIS). EIS measurements were carried out by exerting an alternating current (AC) perturbation in the frequency range of 10 mHz to 30 kHz with a 10 mV peak-to-peak amplitude.

The Zview 3.5h software is used to fit the experimental EIS data into equivalent electrical circuits for a quantitative comparison of microstructures.

Capacitance Measurements

Capacitance measurements (Mott-Schottky analysis) were conducted to study the effect of ferrite-martensite and ferrite-pearlite microstructures on the defectivities of the passive oxide layer. Capacitance measurements were carried out by applying an AC perturbation at a fixed frequency of 1 kHz with 10 mV peak-to-peak amplitude. A potential range of 0.6 V to -1.0 V was swept with a potential step size of 50 mV.

Results and Discussion

Results generated from computational and experimental investigations are presented in this section. Simulation results examine the contribution of the phase volume fraction on the corrosion behaviour for electrochemical input data that models ferrite-martensite and ferrite-pearlite microstructures. After presentation of the results, the different behaviour is discussed through Evans diagrams, and a mathematical model that is useful for future preliminary investigation is introduced. Experimental results explore the active and passive behaviour of ferrite-martensite and ferrite-pearlite samples with similar ferrite volume fractions. After the presentation of experimental results, the nature of the corrosion and passivity behaviour is discussed in light of microstructural features of the phases.

4.1. Simulation

The employed electrochemical finite element simulations for a ferrite-martensite and a ferrite-pearlite microstructure were modelled for different anode/cathode volume fractions. It was aimed that their behaviour would uncover the contribution of phase combinations on the electrochemical response.

Potentiodynamic polarisation behaviour of the microstructures were simulated for a group of different volume fractions. Simulated potentiodynamic polarisation Tafel plots for ferrite-martensite and ferrrite-pearlite for 50% ferrite volume fractions are presented in figures 4.1 and 4.2. As expected, the electrochemical response of the two-phase structure is in between the pure phases. Tafel plots of volume fractions that span the range of 10 to 90% ferrite volume fractions in 10% increments can be found in appendix ${\tt C}$.

The corrosion density values are calculated by Tafel slope analysis of the potentiodynamic polarisation plots. Tangents are drawn from the linear portions of the polarisation plots. These tangents intersect at the corrosion potential and corrosion current density.

Corrosion current densities calculated at different volume fractions via this pro-

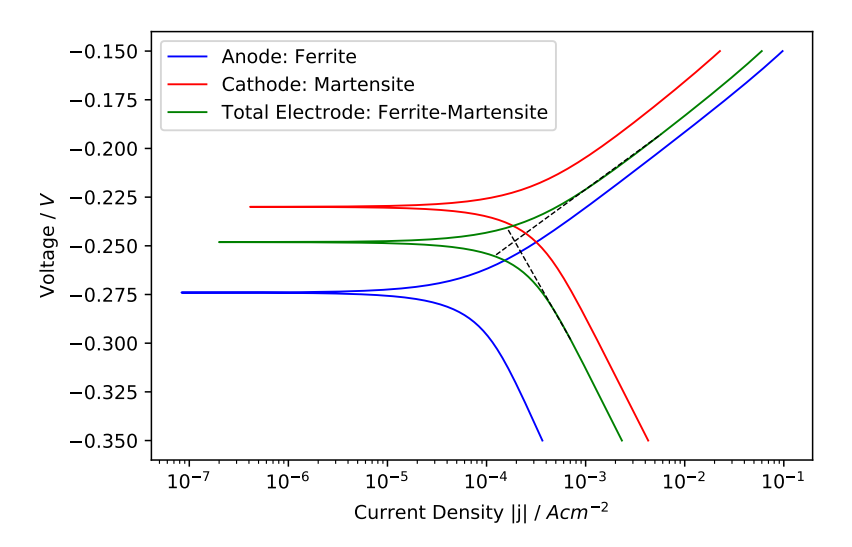


Figure 4.1: Simulated potentiodynamic polarisation curve for the 50% ferrite 50% martensite microstructure.

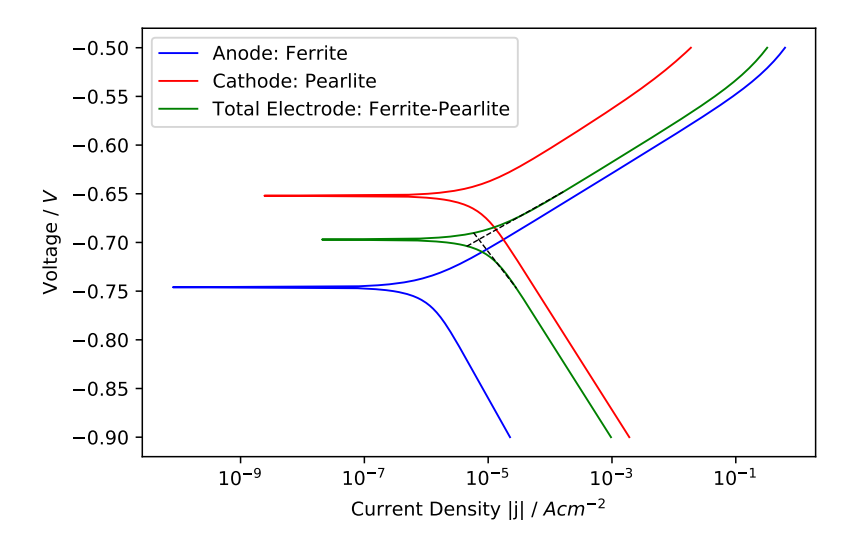


Figure 4.2: Simulated potentiodynamic polarisation curve for the 50% ferrite 50% pearlite microstructure.

4.1. Simulation 55

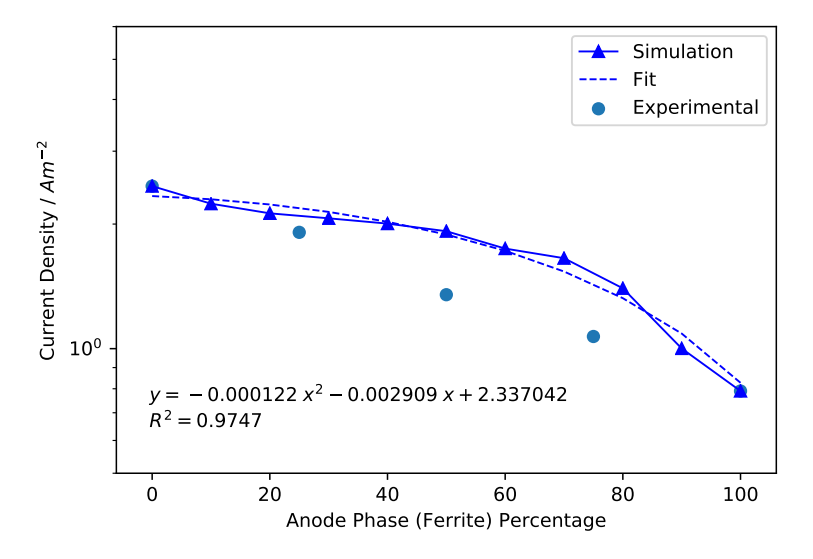


Figure 4.3: Simulated corrosion current density values for various volume fractions of ferrite-martensite microstructure. Experimental values are taken from the paper of Fushimi et al. [37].

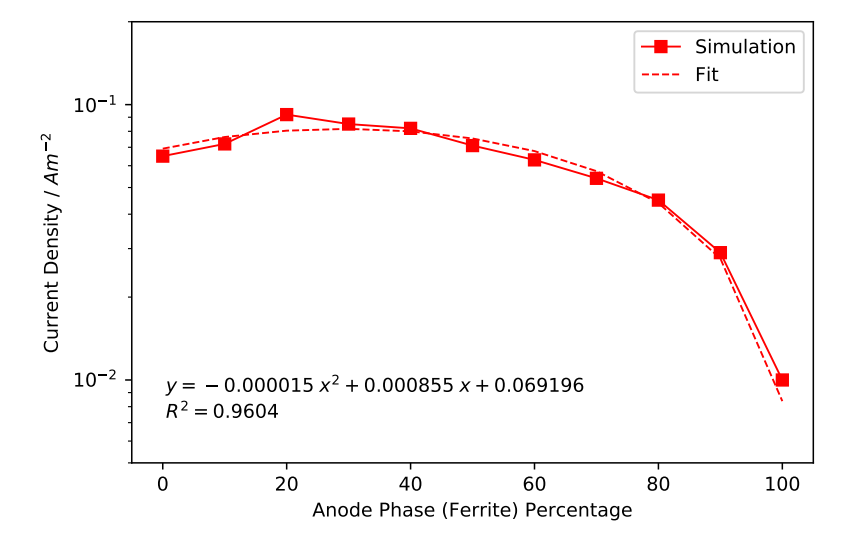


Figure 4.4: Simulated corrosion current density values for various volume fractions of ferrite-pearlite microstructure.

cedure are shown in figures 4.3 and 4.4. Figure 4.3 depicts the effect of volume fraction on corrosion current density for ferrite-martensite microstructure and compares the simulation results with the corresponding fit and experimental data. Figure 4.4 depicts the effect of volume fraction on corrosion current density for ferrite-pearlite microstructure and compares the simulation results with the corresponding fit. It is seen that quadratic polynomial fit is suitable for the simulation results of both microstructures.

4.1.1. The Behaviour of Ferrite-Martensite and Ferrite-Pearlite Microstructure

For the ferrite-martensite simulations, the corrosion current density decreases with increasing ferrite phase fraction. It is recognised that although the simulation and experimental results show the same trend, the values differ minutely. This is most likely the result of the changing microstructural features in the experiments. The finite element model only consists of the electrochemical input (i_{corr} , E_{corr} , anodic-cathodic slopes) for pure ferrite and martensite phases, and does not contain any microstructural data. In experimental studies, the heat treatments that create the various microstructures change the phase fractions as well as other microstructural features such as carbon concentration of phases and dislocation densities. On the other hand for simulations, phase fractions can be changed in an isolated manner. The difference between the results of the idealised simulations and the results of physical experiments reveal the contribution of the rest of the microstructure. Depending on the volume fraction of the phases, the variance between experimental and simulation data is up to 28%. This highlights the importance of the rest of the microstructural features.

The lack of experimental data for in between two-phase ferrite-pearlite structure prevents further comparison of the ferrite-pearlite model with real case scenarios. For the ferrite-pearlite simulations, the corrosion current density also decreases with increasing ferrite phase fraction; but the behaviour is noticeably different than the ferrite-martensite model. In the ferrite-pearlite model, the current density has a maximum around 25% ferrite volume fraction, whereas ferrite-martensite simulation demonstrated an almost linear decrease. This is resulting from the combined behaviour of i_{corr} and E_{corr} input, as they were the only changing free parameters between the two simulations. Rest of the parameters such as model geometry and Tafel slopes were identical for both models.

4.1.2. Phase Volume Fraction Relationship

The comparison of the results from both microstructure models is displayed in figure 4.5. The gap in the current densities between two microstructures is the result of the electrochemical input values that is determined by the composition of the steels and the effect of the environment, therefore it is of secondary importance. The linear regression lines show good correlation for the ferrite-martensite microstructure but a poor fit for the ferrite-pearlite microstructure. This inferior fitting stems from the aforementioned peculiar behaviour of the ferrite-pearlite microstructure. Despite this behaviour, overall decreasing trend in current density with increasing an-

4.1. Simulation 57

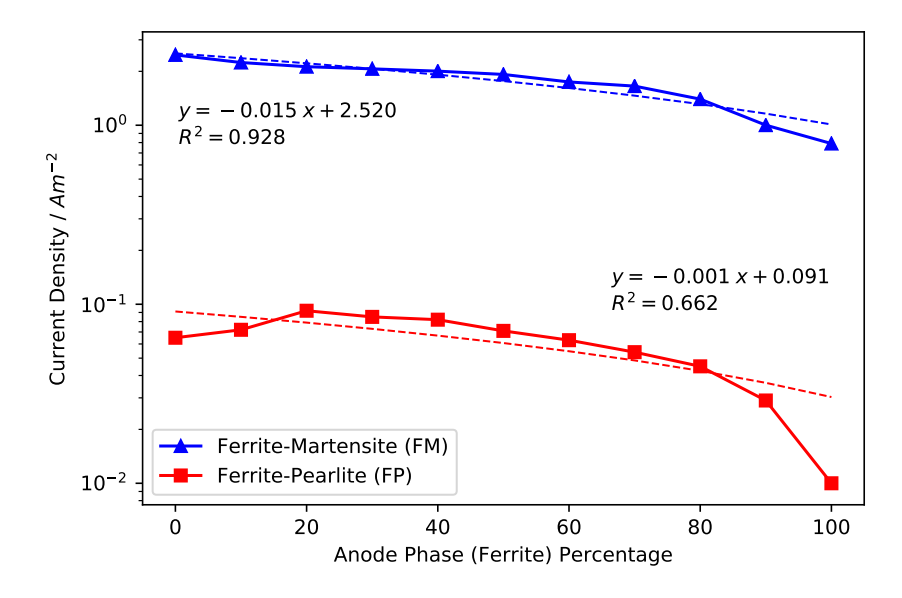


Figure 4.5: The effect of volume fraction on the corrosion current density of simulated ferrite-martensite and ferrite-pearlite microstructures. Fitting values of the linear regression lines are depicted by their R^2 values.

ode phase percentage is alike in ferrite-martensite and ferrite-pearlite simulations. The corrosion model only consists of the electrochemical input(i_{corr} , E_{corr} , anodic and cathodic Tafel slopes) for pure ferrite and martensite phases, and yet produces different volume fraction responses for ferrite-martensite and ferrite-pearlite cases. Differences arising in such an idealised simple geometry highlight the complex behaviour of corrosion.

The complex behaviour of the corrosion model can be explained with the help of a simplified Evans diagram. An Evans diagram depicts the relationship between current and potential for the oxidation and reduction reaction couple. A simplified Evans diagram for two different structures is presented in figure 4.6. Polarisation behaviour of two electrochemically different structures are depicted in blue and red curves. For two structures where ΔV , Δi , anodic and cathodic slopes are the same, their electrochemical behavior is the same - they are electrochemically identical. If the ΔV is increased, a galvanic interaction occurs between the structures and one structure gets assigned the role of the anode and the other the cathode, increasing the exchange current in the process. If Δi is also increased, exchange current increases to a greater extent as the anodic and cathodic curves of the structures intersect at a greater current value. The slopes of anodic and cathodic curves also influence the intersection point accordingly.

The same anodic and cathodic slopes were chosen for ferrite-martensite and ferrite-pearlite models, so the only difference between the simulations were i_{corr} and E_{corr} values. By influencing the exchange current density in finite element

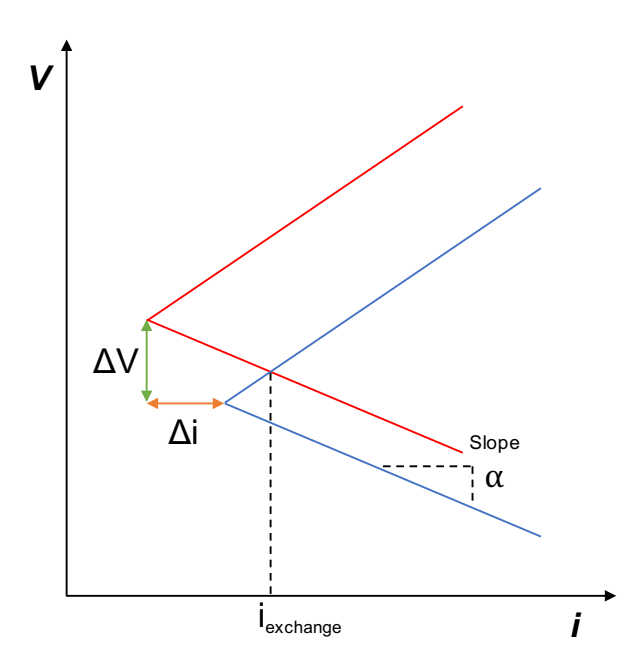


Figure 4.6: Evans diagram that shows the relationship between current and potential for a galvanic interaction between two different structures.

models, the minute changes between the electrochemical inputs evolved a clearly different relationship. Ferrite-martensite model responded to the anode phase fraction increase with an almost linear decrease in corrosion current density. On the other hand, ferrite-pearlite model had a corrosion current density peak around 25% and a relatively harsher current density decrease around 80%.

The existence of a non-linear behaviour even in such an idealised case emphasises the complexity of the corrosion phenomena once more. In the real case scenario, microstructural features complicate the electrochemical behaviour significantly. Inclusions act as local anodic/cathodic sites, the microgalvanic interactions occur in ferrite-cementite lamellar structure of pearlite, and high dislocation density zones in martensite change the electrochemical potential in the vicinity. Despite these intricacies of the real microstructure, it is shown that these simple models are a beneficial tool in creating an initial idea for preliminary analysis before starting experimental investigations.

Microgalvanic Effect Mathematical Model

The fits from the examined models can also be used to aid the preliminary experimental investigations. It is seen that the quadratic polynomial functions in the form of

$$y = A + Bx + Cx^2 \tag{4.1}$$

4.1. Simulation 59

fit the current density - volume fraction data adequately. The terms of the fit can be rearranged, resulting in

$$y = Kx(100 - x) + Mx + N (4.2)$$

where the new coefficients correspond to

$$K = C$$
 $M = B + 100C$ $N = A$ (4.3)

Analysed in this form, the coefficients of the fit gain physical meaning through interpretation of the boundary conditions. When x = 0, the model consists of 0 percent anode, meaning that it is the pure cathode phase. In this condition the first two terms are equal to zero, leaving y = N. This results in N taking the corrosion current density value of the cathode. When x = 100, the model consists of 100 percent anode, meaning that it is the pure anode phase. In this condition, the first term is equal to zero, and the polynomial function returns y = 100M + N, which is equal to the corrosion current density of the anode. In this case, M acts as a factor that connects cathode corrosion density N with anode current density 100M + N. The corrosion current densities of the anode and the cathode are linearly linked through this factor. The physical interpretation of K could be explained on the basis of the Evans diagrams used in the previous section. It is a function of i_{corr} , E_{corr} , anodic and cathodic slopes that result in the complex behaviour of the microgalvanic coupling. Exact determination of this term was out of scope, but could be illuminated with further statistical analysis of the simulations. Given enough data, a relatively simple machine learning algorithm could reveal the dependence of this term on electrochemical parameters of i_{corr} , E_{corr} , and anodic and cathodic Tafel slopes.

The combination of these three terms give the electrochemical coupling of an idealised two-phase system. If these terms could be determined through a combined experimental and modelling analysis for various microstructures, and afterwards stored in an archive; the fit functions can be used to assist experimental investigations by giving an idea about the electrochemical nature of the microstructures before the actual experiments.

Validation of the Model

The validation of the models are necessary, especially for the ferrite-pearlite microstructure where no experimental data was available for in between volume fractions. The validation could be carried out through creating microstructures with different volume fractions through careful heat treatments. If the models are validated, the electrochemical data for dual phase microstructures with different volume fractions would also act as a data archive for the proposed fit investigation mentioned in the previous section.

Provided that the model accuracy is tested by further experimental investigations, the mathematical model could aid in the investigation of the effect of volume fraction and other microstructural features on the corrosion behaviour. This could decrease time and effort spent on creating various dual phase microstructures, as it is a costly process. It would also be of paramount importance in illuminating the complex corrosion phenomena of high strength steels.

4.2. Experimental

In this section, the experimental results of two different microstructures - a ferrite-martensite and a ferrite-pearlite dual phase microstructure - with similar volume fractions are presented. After characterisation of the microstructure, electrochemical measurements for active and passive conditions are shared. The distinct corrosion responses of the samples are discussed in light of microstructural features of the phase constituents.

4.2.1. Microstructure Characterisation

In section 3.1.2 it was mentioned that 8 different heat treatments were carried out during dilatometry to create different microstructures. This section focuses on the results of 2 different heat treatment routes that generated dual phase ferritemartensite and ferrite-pearlite microstructures, as they were the samples selected for further electrochemical analysis.

Dilatometry

The heat treated samples demonstrate that annealing at $1000\,^{\circ}\text{C}$, which is a temperature significantly higher than the Ac_3 temperature of the initial DP1000 microstructure, results in a homogonised microstructure that is suitable for electrochemical experiments. It is also established that intercritical heat treatments are suitable for creation of two phase microstructures through partial austenite stabilisation into ferrite. The remaining austenite in the two phase ferrite-austenite intermediate structure is appropriate for transforming it into martensite through direct quenching, and also appropriate for pearlite generation that produces a ferrite-pearlite microstructure.

Figures 4.7 and 4.8 display the employed heat treatments and the dilatation responses of the samples. Samples demonstrate distinct dilatation behaviour arising from the created diverse microstructures.

Figure 4.7 exhibits the transformation plateaus of the intercritical heat treatments and of the isothermal holding heat treatment for the ferrite-pearlite microstructure. It is seen that after a certain amount of increase, the dilatation value reaches an equilibrium value and stops changing. This indicates that complete and stabilised transformations took place for both samples. Only grain growth continues after this phase stabilisation.

Figure 4.8 presents the dilatation behaviour with respect to the temperature more clearly. As the temperature is increased, a linear dilatation is observed due to the thermal expansion of the sample. Around 720 °C, linear dilatation is disturbed because of the phase transformation from ferrite to austenite structure - a change of crystallographic organisation from body-centred cubic (BCC) to the face-centred cubic (FCC) structure. This is observed due to the difference in the unit cell volume

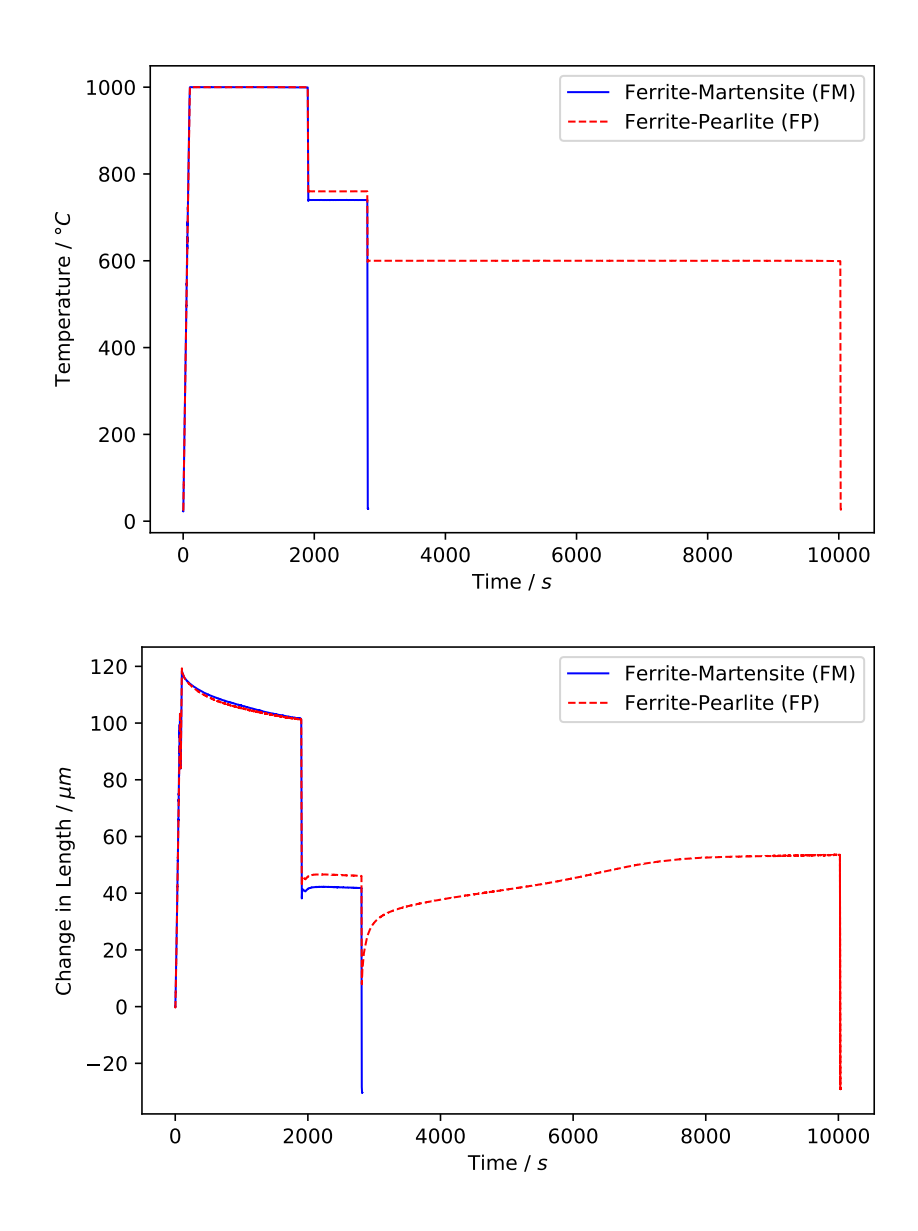


Figure 4.7: Time and temperature evolution with time for different heat treatment routes. Samples had a length of 10 mm. A heating rate of 30°C/s and a cooling rate of 10°C/s is employed during the heat treatments.

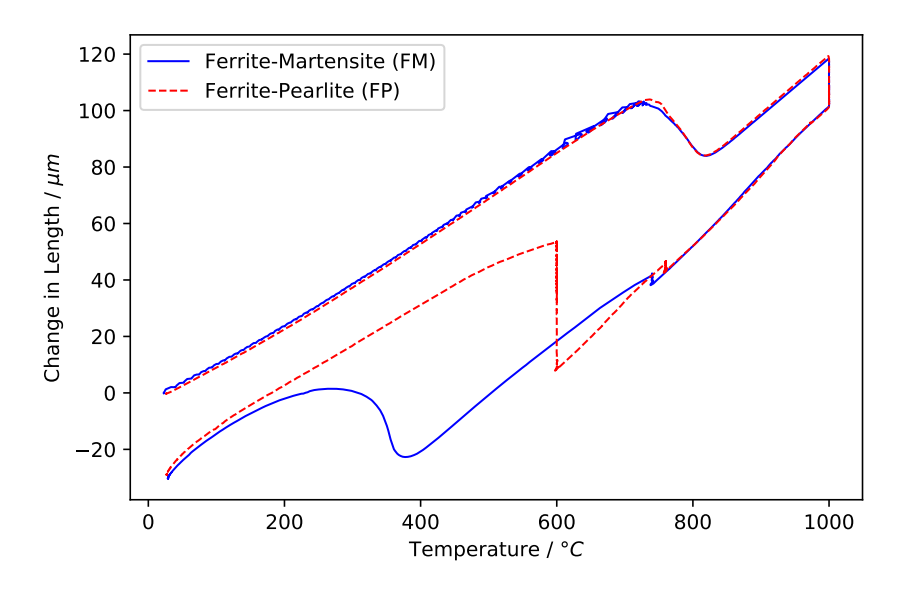


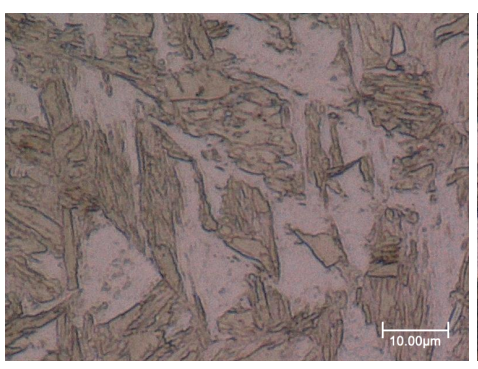
Figure 4.8: Dilatometric curves for dual phase ferrite-martensite (FM) and ferrite-pearlite (FP) microstructures. Samples had a length of 10 mm. A heating rate of 30°C/s and a cooling rate of 10°C/s is employed during the heat treatments.

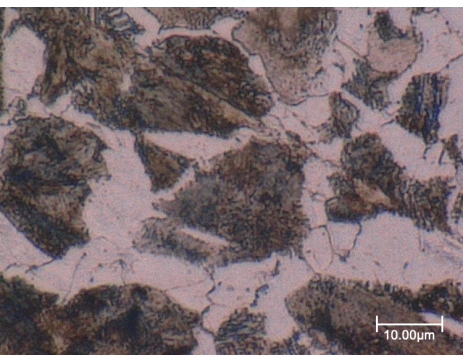
of BCC and FCC structures. Return to the linear dilatation behaviour at 840 °C indicates the completion of the austenite transformation.

As the samples are cooled down to their intercritical annealing treatment temperatures, the dilatation is seen to be linear, suggesting that the samples maintained their austenite structure. Intercritical heat treatments resulted in some dilatation, indicating a partial transformation of austenite into ferrite. Subsequent isothermal holding of ferrite-pearlite sample resulted in a comparatively greater dilatation; ferrite-pearlite sample had a dilatation around 0.5% during the 2 hour transformation at 600 °C. This is due to the diffusive transformation that occurs during the isothermal holding step, resulting in a ferrite-pearlite microstructure. On the other hand, a martensitic transformation is visible for the ferrite-martensite sample around 400 °C, which is completed around 140 °C. This displacive transformation causes FCC crystal structure of the austenite to transform into body-centred tetragonal structure due to the immobile carbon atoms trapped inside the unit cell. No martensitic transformation is seen for the ferrite-pearlite sample, which indicates that all of the previous austenite had been transformed into new structures in the isothermal holding step.

Optical Microscopy and SEM

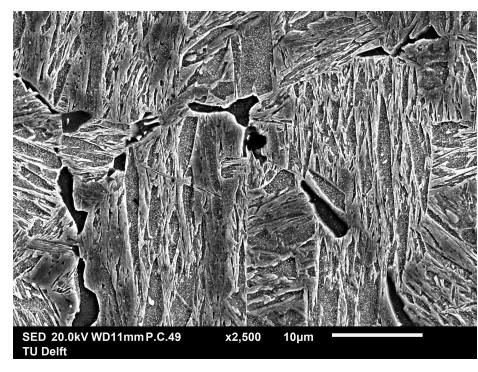
The optical microscopy and SEM images of the samples are displayed in figure 4.9. Microscopical investigations reveal that the heat treatments resulted in a ferritemartensite and a ferrite-pearlite microstructure.

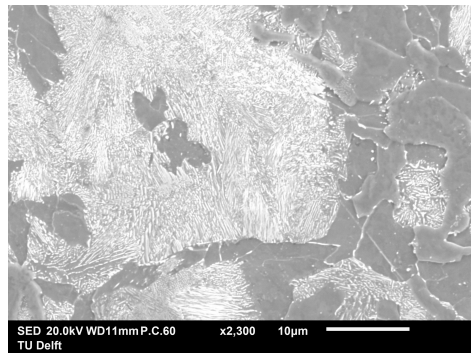




phase is displayed with a darker hue.

(a) Optical micrograph of the ferrite-martensite mi- (b) Optical micrograph of the ferrite-pearlite microstruccrostructure. Etching produces a contrast where ferrite ture. Etching produces a contrast where ferrite phase phase is displayed with a lighter shade while martensite is displayed with a lighter shade while pearlite phase is displayed with a darker hue.





(c) SEM micrograph showing the details of the secondary (d) SEM micrograph showing the details of the secondary martensite phase of the ferrite-martensite microstruc- pearlite phase of the ferrite-pearlite microstructure. ture.

Figure 4.9: Optical and SEM images taken from ferrite-martensite and ferrite-pearlite dual phase microstructures: (a) ferrite-martensite microstructure, (b) ferrite-pearlite microstructure, (c) detail from the martensite phase, (d) detail from the pearlite phase.

The ferrite-martensite and ferrite-pearlite microstructures resulting from the heat treatments in the dilatometry are presented in figures 4.9a and 4.9b respectively. Lighter phases in both micrographs show the ferrite phase, while darker coloured phases represent martensite and pearlite phases for the ferrite-martensite and ferrite-pearlite structure respectively. The samples were chosen on the basis that their secondary phases, martensite and pearlite, differed but their heat treatments resulted in similar ferrite volume fractions. Ferrite-martensite microstructure had a ferrite volume fraction of 50%, while ferrite-pearlite microstructure had a ferrite volume fraction of 56%. It is seen from the micrographs that both microstructures had similar grain sizes but ferrite-pearlite had a relatively more equiaxed grain morphology as expected.

The secondary martensite and pearlite phases are examined more thoroughly

with SEM in figures 4.9c and 4.9d. The needle-like grain features of the martensite phase and the ferrite-cementite lamellar structure of the pearlite phase is clearly visible in the micrographs. The disorderly dislocation dense structure of the martensite phase resulting from the displacive transformation is distinguishable in 4.9c. Figure 4.9d displays repeating fine ferrite and cementite lamellae of the pearlite phase.

Hardness Measurements

The hardness measurements of individual phase constituents are taken to verify the microstructure investigations. Results of the microhardness measurements are shown in table 4.1.

Table 4.1: Vickers microhardness measurements of individual phase constituents for ferrite-martensite and ferrite-pearlite microstructures at 0.01 HV scale.

| Ferrite- | Martensite | Ferrite-Pearlite | | | |
|--------------|------------|------------------|----------|--|--|
| Ferrite | Martensite | Ferrite | Pearlite | | |
| 378 ± 55 | 675 ± 98 | 296 ± 76 | 491 ± 72 | | |

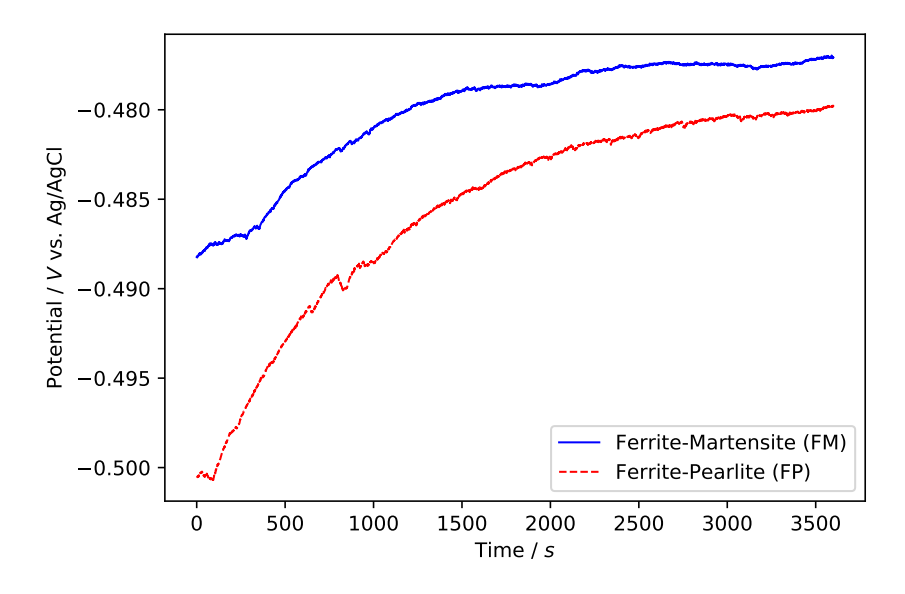
Ferrite phases displayed the softest mechanical behaviour. The difference in hardness values of the ferrite phases of different microstructures could be explained through their different heat treatments. In the ferrite-pearlite structure, 2 hours of isothermal holding would allow carbon and possibly other alloying elements to diffuse out of ferrite and into the surrounding phases. This may cause the ferrite phase of the ferrite-pearlite microstructure to be softer than the ferrite phase of the ferrite-martensite microstructure. Pearlite and martensite phases had higher hardness values than their accompanying ferrite phases. Martensite phase had the highest hardness measurement value as expected. Since microhardness measurements are localised measurements, some variance in the results is expected as local microstructural features like dislocation density and grain boundary presence would affect the measurements. The difference in hardness values matched well with results from the literature [81].

4.2.2. Electrochemical Measurements: Active Behaviour

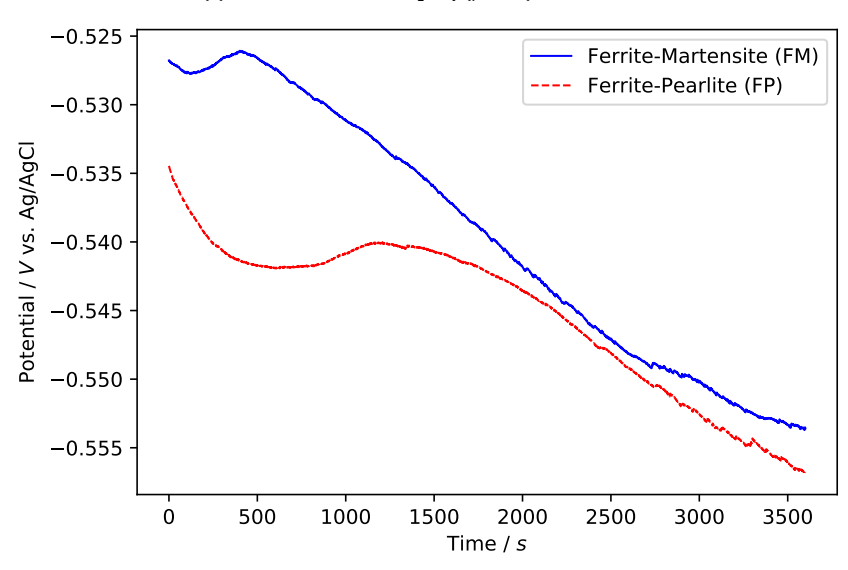
The results of the electrochemical experiments that analyse the phase contribution on the active corrosion behaviour of ferrite-martensite and ferrite-pearlite microstructures are presented in this section. Samples were first immersed in the 0.1M (pH 1.0) sulphuric acid solution for an hour for the stabilisation of the OCP. Afterwards, EIS measurements were carried out. As the last step, potentiodynamic polarisation measurements were performed. Same procedure is repeated for the diluted 0.01M (pH 1.9) sulphuric acid solution.

Open Circuit Potential

Figure 4.10 presents the OCP measurements for the active sulphuric acid environments. OCP measurements have stabilised after 1 hour.

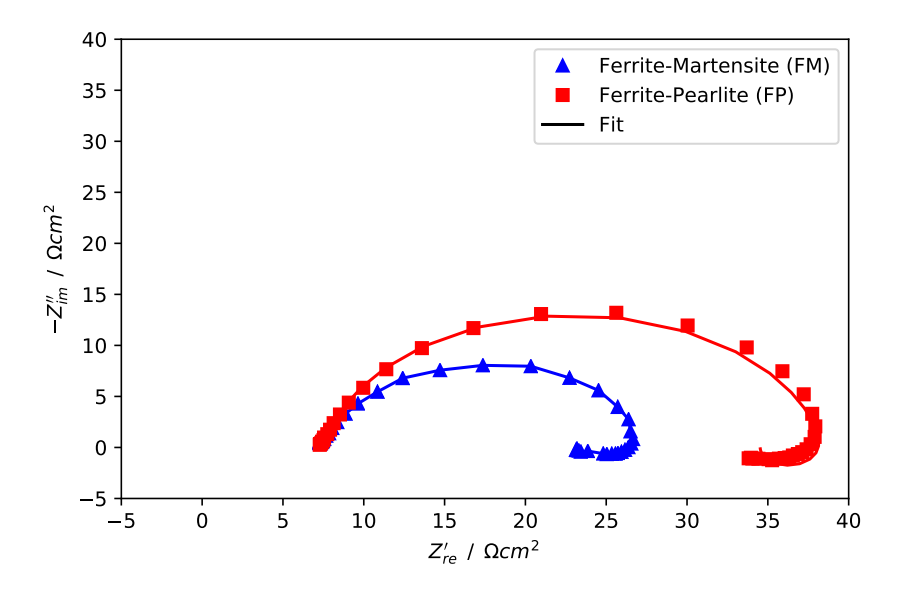


(a) OCP values for 0.1M H_2SO_4 (pH 1.0) environment.

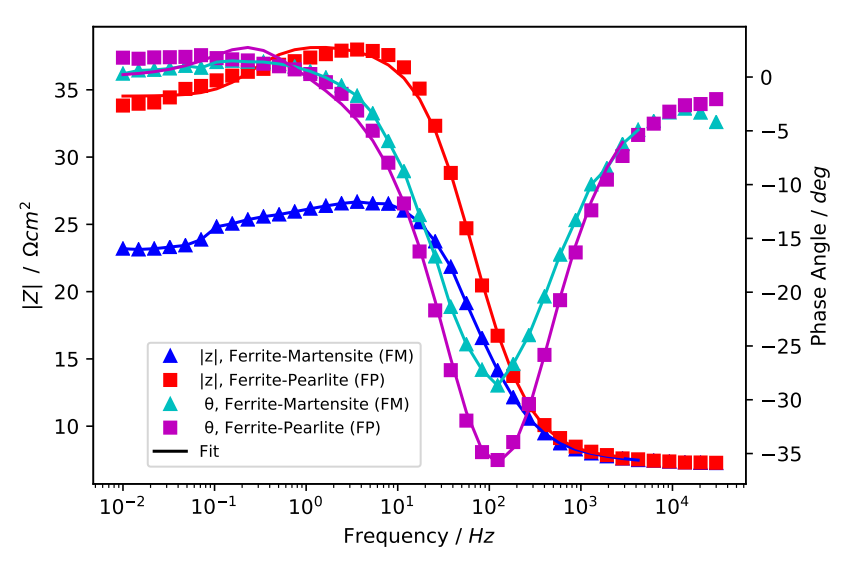


(b) OCP values for 0.01M H_2SO_4 (pH 1.9) environment.

Figure 4.10: OCP values of ferrite-martensite (FM) and ferrite-pearlite (FP) microstructures in 0.1M (pH 1.0) and 0.01M (pH 1.9) sulphuric acid environments.

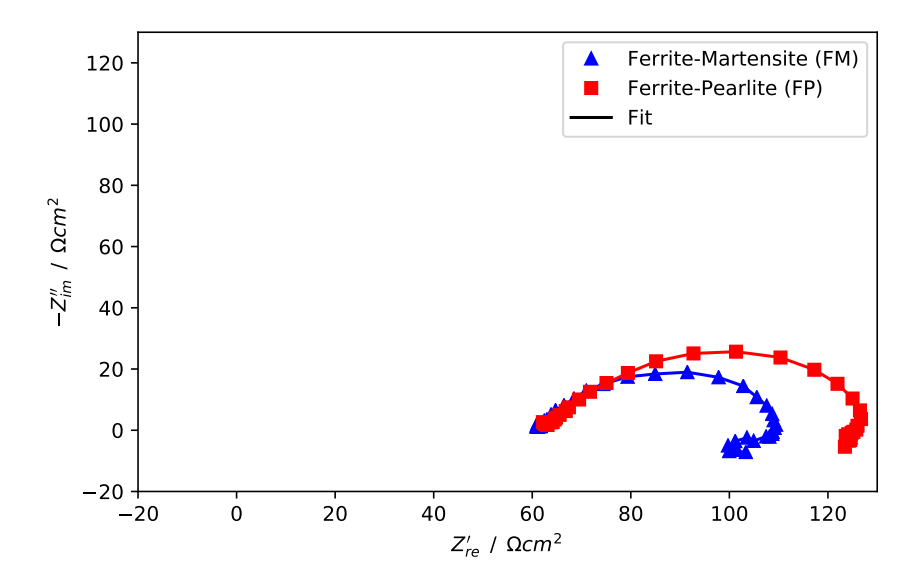


(a) Nyquist plots of ferrite-martensite (FM) and ferrite-pearlite (FP) microstructures.

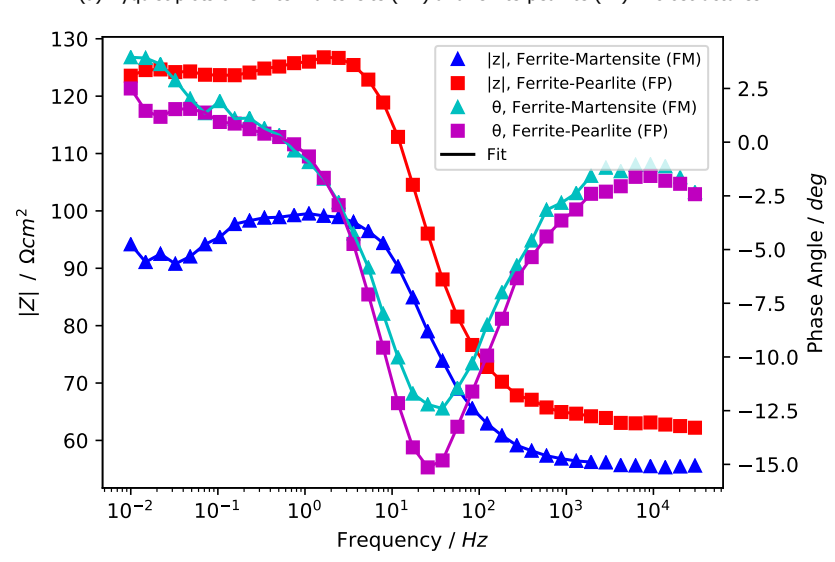


(b) Bode plots of ferrite-martensite (FM) and ferrite-pearlite (FP) microstructures.

Figure 4.11: Nyquist (a) and Bode (b) plots of dual phase ferrite-martensite and ferrite-pearlite microstructures obtained with EIS in $0.1 \text{M}~H_2SO_4$ (pH 1.0) environment.



(a) Nyquist plots of ferrite-martensite (FM) and ferrite-pearlite (FP) microstructures.



(b) Bode plots of ferrite-martensite (FM) and ferrite-pearlite (FP) microstructures.

Figure 4.12: Nyquist (a) and Bode (b) plots of dual phase ferrite-martensite and ferrite-pearlite microstructures obtained with EIS in $0.01M\ H_2SO_4$ (pH 1.9) environment.

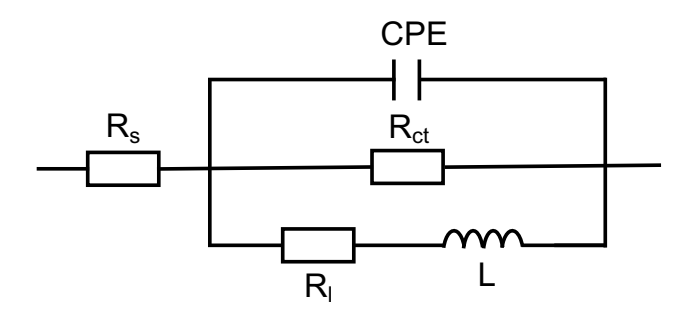


Figure 4.13: Equivalent circuit proposed for modelling the electrochemical response of dual phase ferritemartensite and ferrite-pearlite microstructures in sulphuric acid environment.

The measurements show similar potential values for ferrite-martensite and ferrite-pearlite microstructures. It is seen that the potential values drift to more positive values as the acid concentration is increased and pH is decreased.

Electrochemical Impedance Spectroscopy

Figures 4.11 and 4.12 display EIS measurement results in the form of Nyquist and Bode plots. Figure 4.11 conveys the results for the 0.1M H_2SO_4 (pH 1.0) environment while 4.12 conveys the results for the 0.01M H_2SO_4 (pH 1.9) environment.

Nyquist plots show that ferrite-pearlite sample exhibit a larger arc diameter than the ferrite-martensite sample in both concentrated and diluted acid environments. In both environments, Bode plots show a higher impedance value for the ferrite-pearlite sample at the low frequency of 10^{-2} Hz. For the concentrated environment, impedance values of ferrite-pearlite and ferrite-martensite are $33.83~\Omega cm^2$ and $23.19~\Omega cm^2$ respectively. For the diluted environment, impedance values of ferrite-pearlite and ferrite-martensite are $124.36~\Omega cm^2$ and $93.55~\Omega cm^2$ respectively. The larger arc of the Nyquist plots and the higher impedance values of the Bode plots indicate a more corrosion resistant electrochemical response for the ferrite-pearlite microstructure. The ratio of the resistance values of ferrite-pearlite and ferrite-martensite samples are 1.46~and~1.33 in concentrated and diluted conditions respectively. Higher resistance ratio of the concentrated acid environment signal the increased importance of the microstructural differences for the more aggressive (lower pH) environment.

EIS results demonstrate that an adsorption process occurs at the surface of the specimen. The positive loop seen in the low frequency range of the Nyquist plot indicates an adsorption mechanism with H^+ and HSO_4^+ ions at the surface due to the absence of oxygen in the H_2SO_4 solution [82, 83]. This phenomena has been reported on literature and supported with XPS analysis [84, 85]. Surface corrosion products included iron oxide and sulfide species such as $Fe_2(SO_4)_3$, $FeSO_4$, FeOOH, Fe_2O_3 and FeS.

A depressed semicircle and an inductive loop closing on itself indicates that the electrochemical behaviour can be represented by the equivalent circuit shown

Table 4.2: The fitting values of the equivalent circuit components for ferrite-martensite (FM) and ferrite-pearlite (FP) microstructures in 0.1M (pH 1.0) sulphuric acid environment.

| | R_s (Ωcm^2) | $R_{ct} \ (\Omega cm^2)$ | $CP \ (Fcm^{-2}x10^{-5})$ | CP - n (-) | L (Hcm ²) | R_l (Ωcm^2) | $Chi - Squared (x10^{-4})$ |
|----------|-----------------------|------------------------------|---------------------------|---------------|--------------------------------|--|-----------------------------|
| FM FP | _ | 22.22 ± 3.52 33.65 ± 3.37 | _ | | 49.29 ± 9.65 143.38 ± 47.62 | 111.87 ± 19.03 210.36 ± 49.81 | _ |

Table 4.3: The fitting values of the equivalent circuit components for ferrite-martensite (FM) and ferrite-pearlite (FP) microstructures in 0.01M (pH 1.9) sulphuric acid environment.

| | R_s (Ωcm^2) | $R_{ct} \ (\Omega cm^2)$ | CP (Fcm ⁻² x10 ⁻⁵) | CP - n (-) | L (Hcm ²) | R_l (Ωcm^2) | Chi – Squared (x10 ⁻⁴) |
|----------|---------------------------------------|--------------------------|--|------------------------------------|---|--|---------------------------------------|
| FM FP | 58.65 ± 3.40 55.46 ± 11.62 | | 2.10 ± 0.02 1.93 ± 0.35 | 0.84 ± 0.01 0.80 ± 0.03 | 1834.27 ± 1861.98 46.71 ± 14.48 | 164.97 ± 8.21 321.68 ± 125.89 | 1.70 ± 0.43 2.02 ± 1.09 |

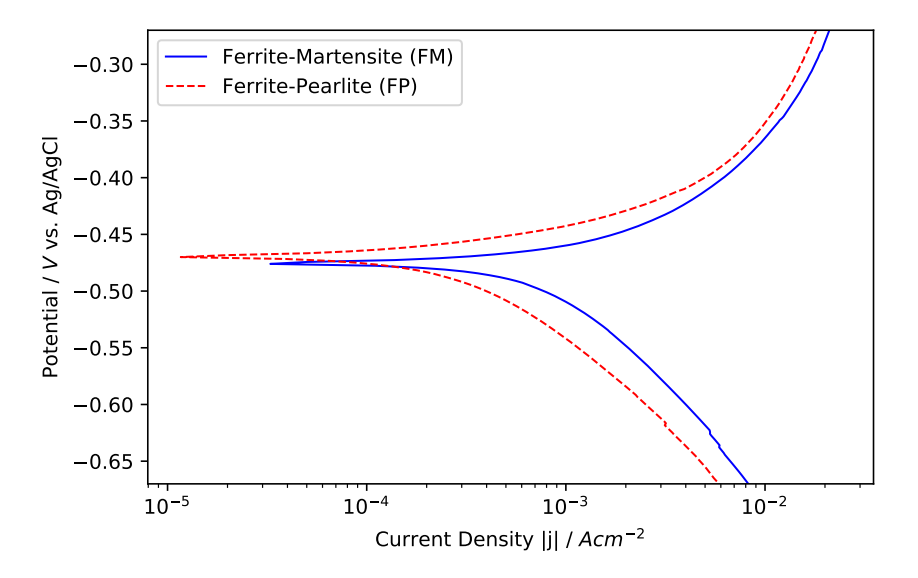
in figure 4.13. R_s represents the electrolyte resistance, R_{ct} the charge transfer resistance of the steel, CPE the constant phase element that represents the double layer capacitance, R_l and L the resistance and inductance related to the adsorbed species layer. Constant phase elements are implemented instead of capacitors due to the deviation from the ideal capacitive behaviour. Capacitance (CP) values are calculated by using the resistance and constant phase element values with the Hsu-Mansfeld approach [86]:

$$CP = R^{\frac{1-n}{n}} Q^{\frac{1}{n}} \tag{4.4}$$

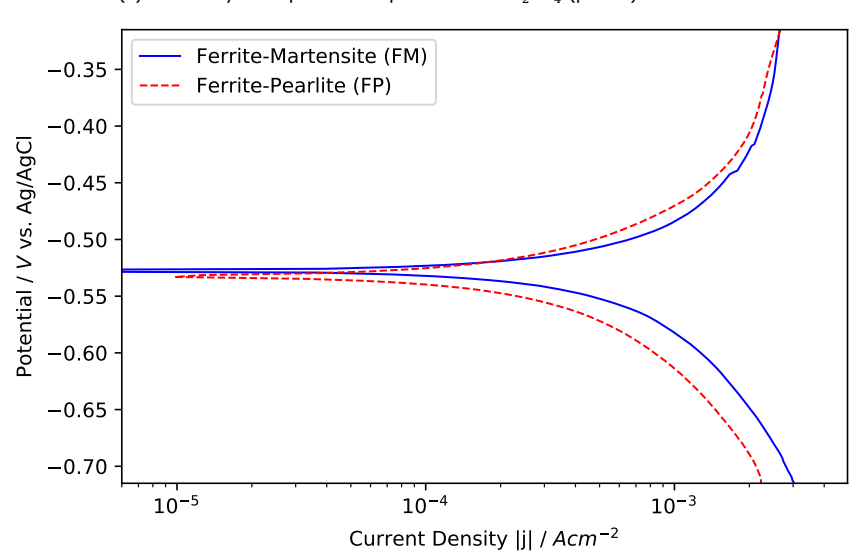
where R is the resistance, n the constant phase element coefficient, and Q the constant phase element constant. Calculated equivalent resistance, capacitance, and inductance values after the equivalent circuit fit are given in tables 4.2 and 4.3. The fit results are also displayed in figures 4.11 and 4.12.

In both concentrated and diluted sulphuric acid environments, charge transfer resistances R_{ct} of the ferrite-pearlite samples are higher than the ferrite-martensite samples. This demonstrates that the ferrite-pearlite microstructure is more resistant against corrosion. Calculated capacitance values CP are similar for all cases. CP-n values of around 0.85 represent a more capacitive behaviour for all conditions, where a value of 1 describes a perfect capacitor and a value of 0 describes a perfect resistor. Resistances of the solutions R_s become smaller as the solution becomes more concentrated - which is to be expected with increased H^+ ion concentration.

Whereas R_{ct} values of the concentrated solution match well with the resistance values directly reported from the lower frequency impedance values of the Bode plot previously, R_{ct} values of the diluted solution are much lower. Despite the good fit of the equivalent circuits with their low Chi-Squared value, this could be a fitting anomaly or an artefact of the equipment. This behaviour and the large difference between the L values of the samples with their high variance could be arising from the odd phenomena of the low frequency tail that is visible in the Nyquist plots of figure 4.12a.



(a) Potentiodynamic polarisation plots for $0.1M\ H_2SO_4$ (pH 1.0) environment.



(b) Potentiodynamic polarisation plots for 0.01M H_2SO_4 (pH 1.0) environment.

Figure 4.14: Potentiodynamic polarisation plots of dual phase ferrite-martensite and ferrite-pearlite microstructures in (a) 0.1M (pH 1.0), (b) 0.01M (pH 1.9) sulphuric acid environments.

Table 4.4: Corrosion current density (j_{corr}) and corrosion potential (E_{corr}) values of ferrite-martensite (FM) and ferrite-pearlite (FP) microstructures calculated from the potentiodynamic polarisation experiments.

| | $0.1M\ H_{2}$ | SO ₄ (pH 1.0) | 0.01M H ₂ SO ₄ (pH 1.9) | | |
|----|---|--------------------------|---|--------------------------------|--|
| | j_{corr} E_{corr} $(Acm^{-2}x10^{-4})$ $(mV \ vs. \ Ag/AgCl)$ | | $ j_{corr} $ $ (Acm^{-2}x10^{-4}) $ | E_{corr} (mV vs. $Ag/AgCl$) | |
| FM | 9.22 ± 0.98 | -470 ± 6 | 3.82 ± 0.97 | -527 ± 1 | |
| FP | 3.78 ± 0.51 | -467 ± 6 | 2.77 ± 0.28 | -534 ± 2 | |

Potentiodynamic Polarisation

Potentiodynamic polarisation plots are shown in figure 4.14 and calculated corrosion current density and corrosion potential values are presented in table 4.4.

Polarisation curves portray no passivation behaviour or significant diffusion limited current in the vicinity of the corrosion potential. This allows analysis of the full active electrochemical response of the samples. Both microstructures show similar polarisation behaviour and almost identical corrosion potentials for the concentrated and diluted acidic environments.

Results reveal that the ferrite-martensite has a higher corrosion current density than the ferrite-pearlite microstructure. The corrosion current density can be directly related to the corrosion rate with the previously mentioned Faraday relation presented in equation 1.11. Ferrite-martensite samples corrode 2.44 times faster than the ferrite-pearlite samples in the concentrated solution, and 1.38 times faster in the diluted one. This indicates that the role of the microstructure on the corrosion behaviour becomes more pronounced as the environment gets more aggressive.

Corrosion potentials of the microstructures are identical in the same environment. As the solution becomes more aggressive and pH decreases, the potentials of both microstructures become more positive. As the environment gets more aggressive, ferrite-martensite sample corrodes 2.41 times faster. Meanwhile ferrite-pearlite corrosion becomes only 1.36 times faster, demonstrating that its corrosion resistance is superior in increasingly acidic environments.

It is seen that the potentiodynamic polarisation measurements fit well with the results of the EIS experiments.

4.2.3. Electrochemical Measurements: Passive Behaviour

The results of the electrochemical experiments that analyse the phase contribution on the passive layer properties of ferrite-martensite and ferrite-pearlite microstructures are presented in this section. The influence of the phase constituents on passive film development is analysed by OCP, potentiostatic polarisation, EIS and capacitance measurements.

Open Circuit Potential

Figure 4.15 presents the OCP measurements for the passive environment. OCP measurements have stabilised after 1 hour. The measurements show almost iden-

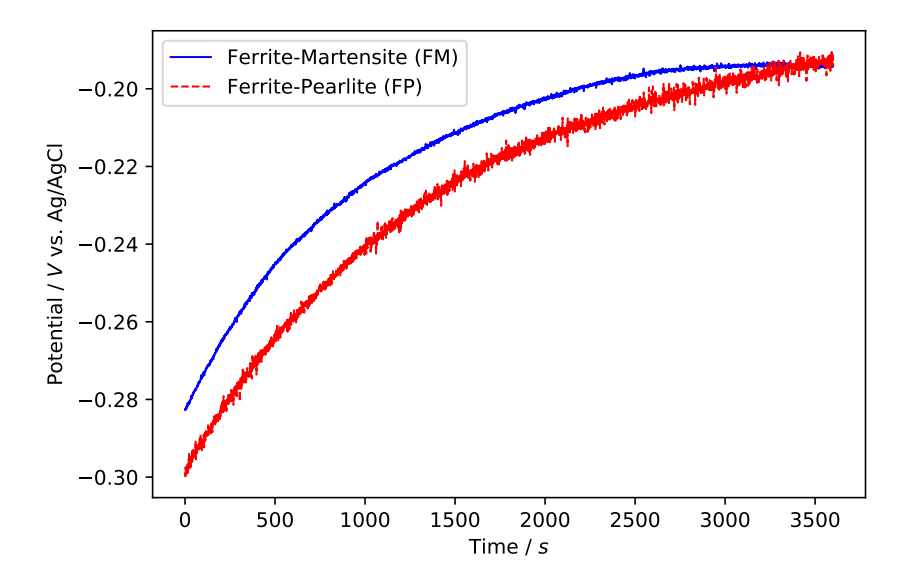


Figure 4.15: OCP values of ferrite-martensite (FM) and ferrite-pearlite (FP) microstructures in 0.1M sodium hydroxide (pH 12.6) environment.

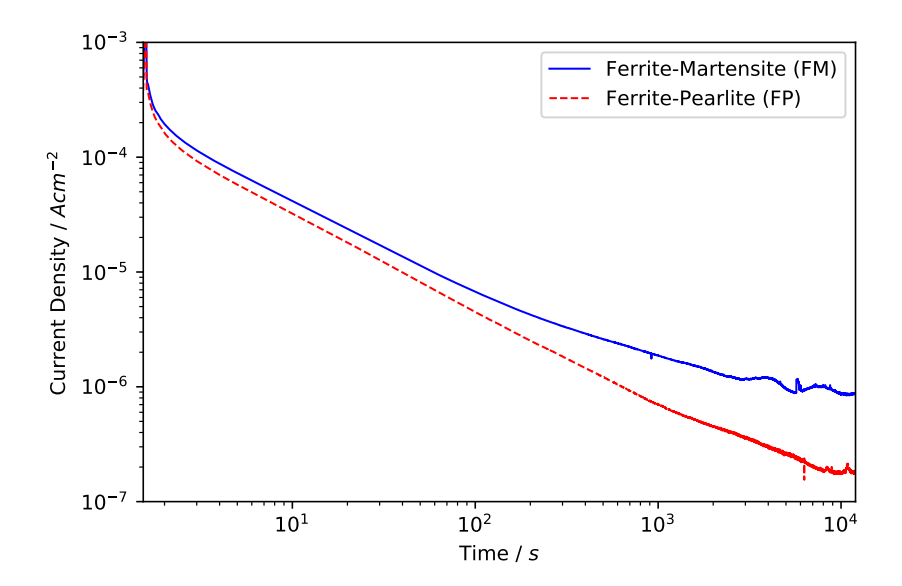


Figure 4.16: Twin logarithmic time-current density plots of ferrite-martensite and ferrite-pearlite microstructures during potentiostatic polarisation at 0.2 V in 0.1M NaOH (pH 12.6) environment.

tical potential values for the ferrite-martensite and ferrite-pearlite microstructures.

Potentiostatic Polarisation

Potentiostatic polarisation of the samples for 6 hours at $0.2\ V$ in 0.1M NaOH (pH 12.6) environment resulted in the formation of stable passive layers on the samples. The evolution of the current density in time during the potentiostatic polarisation experiments is displayed in figure 4.16.

In the initial stage, the current density of both microstructures decrease exponentially due to the rapid formation of an insulating passive layer. Following the initial sharp drop, until around 100 seconds into the potentiostatic polarisation, the ferrite-martensite and ferrite-pearlite samples respectively had logarithmic slope $(-\partial log|j|/\partial logt)$ values of 0.87 and 0.82, which further decreased with the ongoing potentiostatic polarisation. Under a strong electric field with negligible dissolution reactions of the passive layer, in an environment such as the concentrated sodium hydroxide solution, the slope of unity specifies a perfect anodic passive film growth [63]. Therefore it can be hypothesised that the passive layers of both samples grew without dissolution in the beginning by using a substantial part of the current for passive layer growth. Subsequently, the current was dispersed to other processes and reactions such as contributing to the aging of the oxide by transformation of ferrous oxides into ferric oxides.

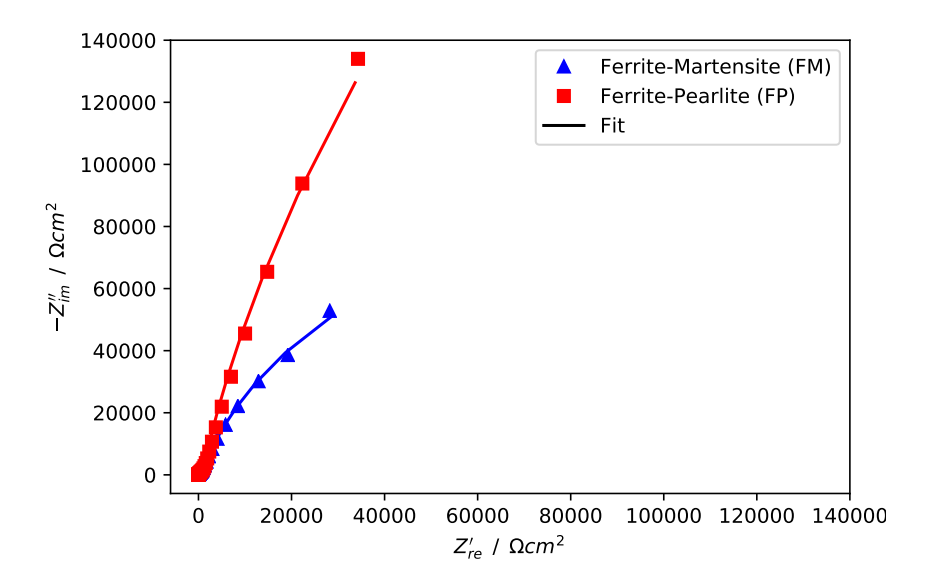
The steady-state current density values of the ferrite-martensite and ferrite-pearlite microstructures are determined to be $1.10\pm0.04~Acm^{-2}$ and $0.17\pm0.02~Acm^{-2}$ respectively. The passive film layer developed on the ferrite-martensite microstructure was 6.5 times more conductive than the passive layer of ferrite-pearlite. Lower passive current density demonstrates the lower conductivity of the (hydr)oxide layer formed on the ferrite-pearlite microstructure. Therefore, ferrite-pearlite microstructure shows a superior passivity behaviour.

Electrochemical Impedance Spectroscopy

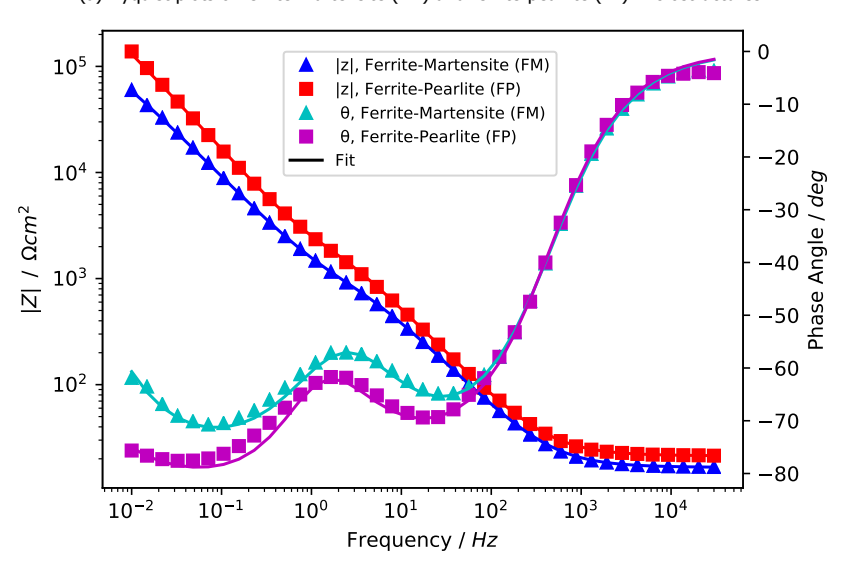
Figure 4.17 displays the EIS measurement results in the form of Nyquist and Bode plots.

Nyquist plots show that the ferrite-pearlite microstructure exhibits a larger arc diameter than the ferrite-martensite sample in the 0.1M NaOH (pH 12.6) environment. Bode plots show a higher impedance value for the ferrite-pearlite sample at the low frequency of 10^{-2} Hz; the ferrite-martensite sample has an impedance value of $59.88~k\Omega cm^2$ while the ferrite-pearlite sample has an impedance value of $138.31~k\Omega cm^2$. The higher impedance and arc diameter values indicate that the passive film layer of the ferrite-pearlite microstructure has better barrier properties. This is in correlation with the steady-state current density values observed during the potentiostatic polarisation experiments.

Dual valleys are observed in Bode phase angle plots of figure 4.17b, suggesting an electrochemical system with two time constants. The EIS results are compared quantitatively by fitting them into an equivalent electrical circuit with two time constant shown in figure 4.18. The chosen equivalent circuit has been previously used in literature to fit the EIS data of low carbon steels in NaOH environments [87, 88]. R_s represents the electrolyte resistance, R_1 the resistance of the double layer, CPE_1



(a) Nyquist plots of ferrite-martensite (FM) and ferrite-pearlite (FP) microstructures.



(b) Bode plots of ferrite-martensite (FM) and ferrite-pearlite (FP) microstructures.

Figure 4.17: Nyquist (a) and Bode (b) plots of dual phase ferrite-martensite and ferrite-pearlite microstructures obtained with EIS in 0.1M NaOH (pH 12.6) environment.

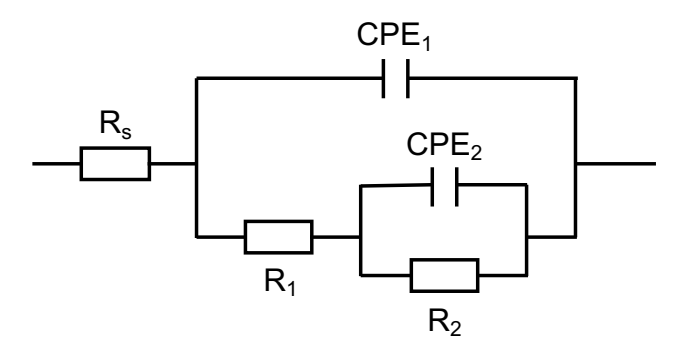


Figure 4.18: Equivalent circuit proposed for modelling the electrochemical response of dual phase ferritemartensite and ferrite-pearlite microstructures in alkaline sodium hydroxide environment.

Table 4.5: The fitting values of the equivalent circuit components for ferrite-martensite (FM) and ferrite-pearlite (FP) microstructures in 0.1M (pH 12.6) sodium hydroxide environment.

| R_s (Ωcm^2) | $R_1 \ (\Omega cm^2)$ | $CP1 \ (Fcm^{-2}x10^{-5})$ | CP1 - n (-) | $R_2 \over (\Omega cm^2 x 10^5)$ | $CP2 \ (Fcm^{-2}x10^{-5})$ | CP2 - n (-) | Chi – Squared (x10 ⁻⁴) |
|-----------------------|------------------------------------|----------------------------|----------------|----------------------------------|----------------------------|----------------|---------------------------------------|
| | 138.83 ± 123.56 370.88 ± 283.05 | | | 1.91 ± 0.27 11.04 ± 3.02 | _ | _ | 3.40 ± 2.23 4.11 ± 2.32 |

the capacitance of the double layer, R_2 the passive film layer resistance, CPE_2 the passive film layer capacitance. Constant phase elements are implemented instead of capacitors due to the deviation from the ideal capacitive behaviour. Capacitance values are calculated from the Hsu-Mansfeld approach previously mentioned as equation 4.4. Calculated equivalent resistance (R) and capacitance (CP) values after the equivalent circuit fit are given in table 4.5.

The equivalent resistance value of the passive film layer R_2 is significantly higher for the ferrite-pearlite microstructure. Passive layer generated on the ferrite-pearlite microstructure is 5.78 times more resistant than the one generated on the ferrite-martensite. This behaviour suggests that the secondary pearlite phase contributes in the formation of a better passive film layer. Calculated CP values are similar for both microstructures. CP-n values of both microstructures show a similar capacitive behaviour of around 0.86, where a value of 1 describes a perfect capacitor and a value of 0 describes a perfect resistor.

Capacitance Measurements

The electronic properties of the passive films are analysed through Mott-Schottky analysis. Figure 4.19 displays the Mott-Schottky plots of the passive film layers. Positive slopes of the samples indicate an n-type semiconductor properties of the passive films, in accordance with the previously reported value for iron in the literature [58]. The slope of the Mott-Schottky plot is inversely correlated with the defect density of the passive films.

A semiconductor-electrolyte interface consists of charged layers both on the semiconductor and electrolyte side, as depicted in an example solution at figure

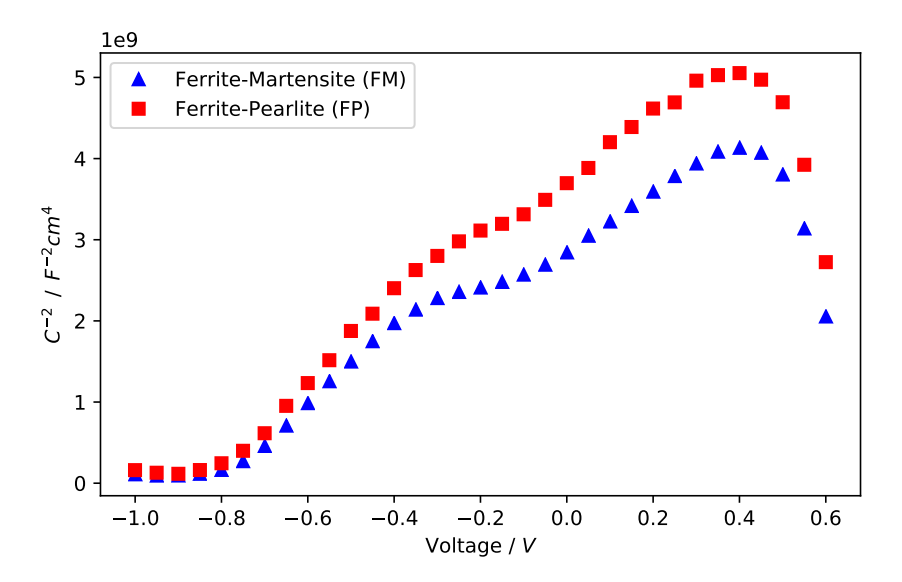


Figure 4.19: Mott–Schottky plots for the passive film formed on dual phase ferrite-martensite and ferrite-pearlite microstructures in 0.1M (pH 12.6) NaOH solutions.

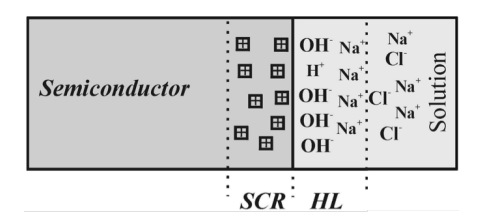


Figure 4.20: Space charge region (SCR) and Helmholtz (HL) double layers at the semiconductorelectrolyte interface.

4.20. Passive film capacitance is influenced by the space charge region of the semiconductor and Helmholtz layer of the electrolyte. The capacitance of the passive film is created by the combined capacitances of space charge region and the Helmholtz layer connected in series.

In the case of the passive film, the capacitance of the space charge region is much lower and the total capacitance can be regarded as the capacitance of the space charge region. For such a case, the donor density of the passive layer can be analysed through the Mott-Schottky relationship:

$$C^{-2} = \frac{2(E - E_{FB} - \frac{kT}{e})}{\varepsilon \varepsilon_0 e N_d} \tag{4.5}$$

where N_d is the donor density, C the capacitance, E_{FB} the flat band potential, k the Boltzmann constant, T the temperature, e the electron charge, ε_0 the permittivity of

vacuum, $\varepsilon = 40$ [89] the dielectric constant of the passive films formed on carbon steels and N_d is the donor density. The derivative with respect to the potential:

$$\frac{\mathrm{d}C^{-2}}{\mathrm{d}E} = \frac{2}{\varepsilon \varepsilon_0 e N_d} \tag{4.6}$$

can be used to calculate the donor densities from the linear part of the Mott-Schottky slopes. The donor densities of the ferrite-martensite and ferrite-pearlite microstructures are calculated to be $2.38 \pm 0.26~x~10^{21}cm^{-3}$ and $1.49 \pm 0.08~x~10^{21}cm^{-3}$ respectively. The ferrite-martensite microstructure is particularly more defective - its donor density value is 1.6 times the value of the ferrite-pearlite sample.

The flatband potential of the samples are also calculated from the x-axis intercept of the Mott-Schottky plots. Ferrite-martensite microstructure had a value of 0.73 ± 0.02 V while ferrite-pearlite microstructure had a value of 0.81 ± 0.01 V. The differences in the flatband potentials indicate a different passive film composition. The iron hydr(oxide) volume fractions of the passive films must be different, as reported in the literature previously [49].

4.2.4. Phase Dependency of Corrosion and Passivity

This section discusses the results of microstructure characterisation (presented in section 4.2.1) and electrochemical experiments (presented in sections 4.2.2 and 4.2.3) in the context of the theoretical background (presented in chapter 1).

Identification of the true effect of phases on the electrochemical properties of the multi-phase advanced high strength steels is particularly important due to their growing use in many industries. To understand the electrochemical behaviour of such steels in active and passive states, studies on simplified model alloys are of utmost importance. This experimental study attempts illuminating the contribution of the phase constituents through a controlled design of dual phase ferrite-martensite and ferrite-pearlite microstructures with same ferrite volume fractions. The changes have been limited to phase differences, and the contribution of other microstructural features (phase volume fraction, dislocation density, chemical composition, crystallographic orientation, grain size, inclusions) have been minimised so that the interaction between them would be kept to a minimum.

For this analysis, heat treatments that span 8 different combinations of intercritical annealing and quench/isothermal holding treatments were designed. The extensive microstructure creation allowed the procurement of two distinct dual phase microstructures that share a similar ferrite volume fraction but different secondary phases - a martensite and a pearlite phase constituent. Chemical composition of the substrate material limited the formation of inclusions. The size of the ferrite grains were similar in both samples. Therefore, the impact of additional microstructural features were kept to a minimum, allowing the phase combinations to play the dominant role on electrochemical responses.

The differences in the hardness values of ferrite phases of the ferrite-martensite and ferrite-pearlite could be related to the diffusion of the alloying elements. The softer ferrite of the ferrite-pearlite microstructure indicates a more lightly alloyed

phase. This change in phase compositions could alter the electrochemical potentials of the phases. Since the composition of the steel is lightly alloyed, it is assumed that this won't have a significant influence on the overall electrochemical response.

Even when final microstructures are the same, it must be highlighted that processing and design of the heat treatments are extremely important for the morphological feature details arising from the differences in microstructure formation mechanisms. In the case of this study, full austenisation prior to the subsequent intercritical annealing let ferrite grains nucleate at the austenite grain boundaries and grow into the austenite grains during the intercritical annealing heat treatment. However, if the austenisation step was skipped and heat treatments were to directly start with an intercritical annealing step, martensite phases of the prior microstructure would have transformed into austenite which would've preferably nucleated on the ferrite-martensite and martensite-martensite boundaries. Such details would've formed different structure morphologies which would've affected the microgalvanic coupling occurring between the final dual phase microstructures. The electrochemical responses of the samples in such cases might be notably different due to the different microstructure formation mechanisms, potentially changing corrosion and passivity behaviour significantly. Different formation mechanisms of the same microstructures are in fact have been found to impact the corrosion behaviour [90], highlighting the importance of nuances during microstructure generation processes. A detailed understanding of heat treatments and their relation to the resulting corrosion properties are key in comprehending the corrosion phenomena of HSLA steels, and the influence of processing must be further investigated by creating similar microstructures with different formation mechanisms.

Electrochemical experiments reveal that the ferrite-pearlite microstructure has a superior electrochemical response in both acidic and alkaline environments. Not only the ferrite-pearlite structure corrodes slower in aggressive conditions, but the passive layer formed on it during suitable circumstances also has more protective barrier layer properties that is more resistant against corrosion.

In active sulphuric acid conditions, the corrosion of the steel is maintained through the self corrosion of the phases and the microgalvanic coupling that results in the preferential dissolution of the more anodic phase. Literature agrees that for both ferrite-martensite and ferrite-pearlite cases, ferrite acts as the anodic phase. By keeping the ferrite volume fraction constant, the contribution of the self corrosion of the ferrite phases to the overall corrosion rate is kept constant. Therefore the differences in corrosion behaviour must be arising from the microgalvanic coupling of the ferrite-martensite ferrite-pearlite phases and the self corrosion of the martensite or pearlite phase constituents.

The corrosion is expected to occur through the anodic dissolution of the steel, and cathodic hydrogen evolution reactions. The thermodynamics and kinetics of the anodic and cathodic reactions are directly influenced by the differences between phases. Different adsorption capacities of hydrogen on the surface, differences in factors such as electronic properties and surface roughnesses result in distinct metal/electrolyte interfaces and electric double layers.

The higher corrosion rate and the lower corrosion resistance of the ferrite-

martensite microstructure is tied to the electronic properties of the substrate and the formed double layer. The influence of the pH demonstrates that microstructural differences become more important with increased solution concentration. This makes sense as the electric field generated by the double layer would become larger with increased dissolved species (H^+) , making the differences in surface properties become more pronounced.

The martensite phase structure has high residual stresses due to the its substantial dislocation density resulting from the entrapped carbon during the diffusionless transformation. Carbon trapped in the crystal lattice during the martensitic transformation strains the microstructure. Increased strain and dislocation density accelerate the corrosion rate by decreasing the activation energy in the vicinity of the dislocations. This modification in surface energy impacts the chemical reactions by facilitating atomic and/or ionic transport. Furthermore, the needle-like morphology of the martensite phase gives rise to higher ferrite-martensite surface boundary area, increasing microgalvanic coupling between the anodic ferrite and cathodic martensite zones. In summary, the stressed structure creates a less dense and more active surface, exacerbating the corrosion by facilitating cathodic surface reactions for galvanic corrosion, and by increasing the self corrosion rate in comparison with the more relaxed ferrite phase.

In comparison, the pearlite phase is generated by a diffusive transformation. As the austenite to pearlite transformation progresses, carbon diffuses out of the newly formed ferrite and forms cementite plates next to the ferrite structure. The lamellar structure of the pearlite phase originated by this transformation could possibly cause a weaker microgalvanic interaction with the bulk ferrite phases because of pearlite phase's microgalvanic interaction in its own self. The microgalvanic coupling between ferrite and cementite lamellae inside the pearlite phase might be competing with the microgalvanic interaction between the larger pearlite and ferrite phases. Localised electrochemical experiments such as scanning Kelvin probe force microscopy could reveal the local microgalvanic coupling of the phases of different microstructures and explain the reason behind the different responses more clearly.

In passive sodium hydroxide environment, the passive film layer of the ferrite-martensite microstructure has less protective barrier properties. The inferior barrier properties of the ferrite-martensite microstructure is related to the more defective passive film formed on the substrate microstructure. The defective passive film layer contains a higher donor density.

The donor density is important in determining the ionic and electronic conductivity of the passive film layer. Increased defect concentration facilitates ionic penetration through the passive layer, thereby allowing a higher ionic current [49]. On the other hand, a higher donor density assists the transfer of electrons by decreasing the band gap of the semiconductor layer, giving rise to a higher electronic conductivity [91]. Consequently, both the ionic and electronic resistivities of the passive film depreciate.

The relative defectiveness of the ferrite-martensite passive film can be explained on the basis of the properties of the substrate martensite microstructure. The

distorted dislocation dense surface of the martensite structure is the result of the displacive transformation. As a result of this transformation, ferrite-martensite grain boundaries contain a significant amount of lattice mismatch. Both these high energy grain boundaries and dislocation zones result in high surface energies. Dislocations, intricate lath and grain boundaries prevent an oxide layer growth in an epitaxial manner. The disturbed growth of the covering film results in a more defective passive film layer. Previous research has similarly demonstrated the harmful effect of martensite on passivity, where the donor density of pure martensite phase is shown to be higher than of ferrite-martensite and of pure ferrite phase [49].

A more defective structure could also be creating a more conductive passive layer by promoting the formation of Fe_3O_4 with higher oxygen vacancy concentrations. As mentioned in section 1.5.3, the electronic resistance of bulk Fe_3O_4 is considerably lower than Fe_2O_3 - a difference of up to $10^{16}~\Omega~m$ [59] with a significant difference in bandgap: 0.1 eV for Fe_3O_4 [92] and 2.3 eV for Fe_2O_3 [93]. Furthermore, corrosive species such as oxygen can easily penetrate the passive film in open porous structures such as FeO(OH) [48].

Electronic conductance is influenced also by the aging of the oxide, where processes such as conversion between Fe^{+2} - Fe^{+3} species and improvement in the crystallinity of the oxide occurs [63]. The difference in slopes of the potentiostatic experiments suggests that a larger part of the current of the ferrite-martensite sample is directed towards such processes instead of creating a more robust oxide layer.

The relative hydr(oxide) fractions of the passive layer and their crystallinity without a doubt influences the protective properties of the barrier film. The difference in flatband potential indicates different hydr(oxide) compositions for the ferrite-pearlite and ferrite-martensite microstructures. X-ray photoelectron spectroscopy (XPS) experiments would reveal the composition of the passive films and illuminate the difference in passivity behaviour between the microstructures.

In conclusion, a clear phase dependency is recognised for both active and passive states. For the active behaviour, the influence of the phase constituents became more important in concentrated solutions. For the passive behaviour, defectivity and composition of the passive film played an important role. The differences of ferrite-martensite and ferrite-pearlite microstructures boiled down to their core displacive and diffusive transformation mechanisms.

Conclusions and Recommendations

5.1. Conclusions

This thesis investigated the role of phase combinations on the corrosion and passivity behaviour of high strength steels. Understanding the effect of microstructure on the electrochemical response of HSLA steels is critical, but unfortunately coupling of the individual microstructural features prevent a clear understanding of the subject. The modification of one microstructural feature is accompanied by several others during heat and thermomechanical treatments, so it is highly important to understand the entire influence of the production processes.

The literature does not have one common paradigm that explains the impact of microstructure on corrosion behaviour. The overall trends indicate that:

- The competition between self-corrosion and galvanic corrosion is important in the determination of corrosion activity.
- Smaller, acicular grains with excessive residual stresses have increased surface reactivities that result in inferior active corrosion resistance but superior passive layer properties.
- Grain size, grain morphology, residual stresses, crystallographic orientation, compositional differences in between the grains, segregation at and misorientation of the grain boundaries, different phase constituents, nature of inclusions, passive oxide layer structure, chemical composition plays a role in the corrosion of steels.
- The effect of crystallographic orientation on corrosion is significant but still vague. Research on pure iron is insightful and lays the foundation but detailed work with steels is lacking.

- Pearlite, bainite and martensite have different dominant microstructural features that determine the active corrosion and passivity. A common behaviour is that more uniform structures tend to decrease the corrosion rate.
- Compactness of the oxide layer is one of the main factors that determine the corrosion protection. Homogeneity and porosity of the oxide layer combined with its electrochemical properties have a huge impact on the corrosion response.

The entanglement of microstructural features prevent the deduction of the actual corrosion controlling element. Careful consideration is required to isolate the coupled microstructural features during experiments. This is only possible by accurate understanding of the processes in which microstructure is created, and careful elimination of free parameters that may have an effect on corrosion behaviour during electrochemical experiments.

The large scatter of data from different electrochemical experiments in the literature indicates the need for a more formal straightforward testing methodology for microstructural corrosion experimentation. In the current state, a rigorous comparison between papers is not possible as each researcher does experiments in a different way and reports different details of the microstructure - some disclose processes and some the parts of microstructure itself. It is believed that the isolation of free parameters by careful microstructure design, in combination with a more streamlined corrosion experimentation method will reduce the contrasting results in literature, thereby illustrating the clear effect of microstructure on the corrosion phenomena.

To tackle this problem, this thesis combined electrochemical modelling, microstructure design and electrochemical experimentation of model alloys in acidic and alkaline environmental conditions. The focus was to demonstrate the effect of phase constituents on the overall corrosion response of the system. Martensitic and pearlitic dual phase steel alloys were selected as target because of their wide use in the industry.

On the computational side, ferrite-martensite and ferrite-pearlite dual phase microstructures were modelled through finite element simulations. This thesis determined finite element modelling to be a promising method suitable for analysing the complex multiphysics problem of corrosion electrochemistry. The phase volume fraction investigation revealed that corrosion current density increases with the increasing cathode volume fraction for both microstructures. However, even in these idealised models, the anode volume fraction versus corrosion current density relationship is non-linear and microstructures have distinct behaviours: the ferrite-martensite model shows a direct decrease in corrosion current density while the ferrite-pearlite model shows a peak around 25% anode volume fraction. A comparison of the ferrite-martensite model with experimental data shows up to 28% corrosion current density difference between idealised models and real microstructures. This highlights the nuances in the actual microstructure creation process. The models created through only electrochemical properties of pure phases may not be enough to capture these nuances, and details from microstructures could

5.1. Conclusions 83

improve future electrochemical models.

Experimental investigations started with the design of the microstructure. Eight different heat treatments were employed to create two different dual phase microstructures with same ferrite volume fractions but distinct phase combinations: a ferrite-martensite and a ferrite-pearlite microstructure. The microstructures were created in a way that the influence of dislocation density, chemical composition, primary phase (ferrite) volume fraction, inclusions, grain size would be minimised and the feature governing the electrochemical properties would be the secondary martensite/pearlite phase contribution.

Electrochemical experiments carried out in 0.1 and 0.01M H_2SO_4 concluded that the ferrite-martensite microstructure had worse corrosion properties in active conditions than the ferrite-pearlite microstructure:

- Potentiodynamic polarisation measurements show that microstructures have almost identical corrosion potentials but ferrite-martensite structure has a significantly higher corrosion current density.
- Electrochemical impedance spectroscopy experiments reveal that both microstructures have similar capacitive behaviour but ferrite-pearlite microstructure has a higher charge transfer resistance. Both microstructures also display an inductive behaviour resulting from the corrosion products.
- The effect of the microstructure becomes more pronounced with more aggressive environments.

The experiments with steels passivated in $0.1M\ NaOH$ environment demonstrated better barrier properties for the ferrite-pearlite microstructures:

- Potentiostatic polarisation measurements reveal a higher current density for the ferrite-martensite microstructure. Evaluation of the logarithmic slopes of the time - current density plots indicate that larger amount of ferric-ferrous oxide transformation resulted in a more disorderly passive film layer.
- Electrochemical impedance spectroscopy experiments show that the passive layers of the microstructures have similar capacitive behaviour with two time constants but the passivation of the ferrite-pearlite substrate resulted in a significantly more resistive passive layer response.
- The difference between the passive layers was attributed to the higher donor density of the ferrite-martensite film, which develops a more defective structure.

The presented results indicate that active and passive electrochemical behaviour is strongly dependent on the phase constituents of the microstructure. Inferior corrosion properties of the ferrite-martensite microstructure is attributed to the disordered structure of the secondary martensite phase. The increased surface energy facilitates corrosion and results in a more defective barrier film. In contrast, the diffusive transformation of the pearlite phase develops a more relaxed structure that has better corrosion and passivity properties.

5.2. Recommendations

Recommendations for future research can be summarised as:

- The computational models can be checked through collection of experimental data for different phase volume fractions. This would help validate the simulation and the mathematical microgalvanic model.
- The geometry used during the electrochemical simulations can be generated through actual micrographs. The comparison between these more realistic model geometries and idealised cases used in this thesis can give insight into the influence of microstructure morphology on electrochemical behaviour and local microgalvanic coupling of the phases.
- The analysis of same dual phase microstructures created through different heat treatments can give insight into the influence of the formation mechanisms. An example would be to compare the heat treatments used in this study with heat treatments that skip the initial austenisation step and start from the intercritical annealing step. Minute differences between similar microstructures can aid in the investigation of the effect of individual microstructural features on corrosion and passivity.
- The analysis of phases with localised electrochemical experiments such as scanning Kelvin probe force microscopy could explain the differences between microgalvanic coupling behaviour of ferrite-martensite and ferrite-pearlite phases more clearly.
- The differences between the passive film layers could be analysed more in depth through X-ray photoelectron spectroscopy. X-ray photoelectron spectroscopy experiments would uncover the compositions and relative hydr(oxide) fractions of the passive films of ferrite-martensite and ferrite-pearlite microstructures.

References 85

References

[1] B. N. Popov, *Corrosion engineering: principles and solved problems* (Elsevier, 2015).

- [2] G. Koch, J. Varney, N. Thopson, O. Moghissi, M. Gould, and J. Payer, *International Measures of Prevention , Application , and Economics of Corrosion Technologies Study*, NACE International , 1 (2016).
- [3] J. Sietsma, *Physical modelling the microstructure formation in advanced high-strength steels*, in *Materials Science Forum*, Vol. 762 (2013) pp. 194–209.
- [4] Wikimedia Commons, Elcap, *Potential distribution in a helmholtz double-layer*, (2013), [Online; accessed June 6, 2020].
- [5] Wikimedia Commons, Larryisgood, *A diagram of the electrical double layer that forms at the surface of a charged particle,* (2011), [Online; accessed June 6, 2020].
- [6] A. J. Bard, L. R. Faulkner, J. Leddy, and C. G. Zoski, *Electrochemical methods:* fundamentals and applications, Vol. 2 (wiley New York, 1980).
- [7] E. McCafferty, *Introduction to corrosion science* (Springer Science & Business Media, 2010).
- [8] J. Ning, Y. Zheng, B. Brown, D. Young, and S. Nešić, *A thermodynamic model for the prediction of mild steel corrosion products in an aqueous hydrogen sulfide environment*, Corrosion **71**, 945 (2015).
- [9] H. Bhadeshia and R. Honeycombe, *Steels: Microstructure and Properties, Fourth Edition* (Elsevier, 2017).
- [10] Wikimedia Commons, AG Caesar, *Iron carbon phase diagram*, (2013), [Online; accessed July 23, 2020].
- [11] D. A. Porter, K. E. Easterling, and M. Y. Sherif, *Phase Transformations in Metals and Alloys, Third Edition* (CRC Press, 2009) p. 536.
- [12] W. R. Osório, L. C. Peixoto, L. R. Garcia, and A. Garcia, *Electrochemical corrosion response of a low carbon heat treated steel in a NaCl solution*, Materials and Corrosion **60**, 804 (2009).
- [13] P. P. Sarkar, P. Kumar, M. K. Manna, and P. C. Chakraborti, *Microstructural influence on the electrochemical corrosion behaviour of dual-phase steels in* 3.5% NaCl solution, Materials Letters **59**, 2488 (2005).
- [14] A. Schreiber, J. W. Schultze, M. M. Lohrengel, F. Kármán, and E. Kálmán, *Grain dependent electrochemical investigations on pure iron in acetate buffer pH 6.0*, Electrochimica Acta **51**, 2625 (2006).

86 References

[15] Y. Kayali and B. Anaturk, *Investigation of electrochemical corrosion behavior in a 3.5wt.% NaCl solution of boronized dual-phase steel*, Materials and Design **46**, 776 (2013).

- [16] E. Salamci, S. Candan, and F. Kabakci, *Effect of microstructure on corrosion behavior of dual-phase steels*, Kovove Materialy **55**, 133 (2017).
- [17] J. L. Dossett and H. E. Boyer, *Practical heat treating* (Asm International, 2006).
- [18] J. I. Barraza-Fierro, B. Campillo-Illanes, X. Li, and H. Castaneda, Steel microstructure effect on mechanical properties and corrosion behavior of high strength low carbon steel, Metallurgical and Materials Transactions A: Physical Metallurgy and Materials Science 45, 3981 (2014).
- [19] M. Kadowaki, I. Muto, Y. Sugawara, T. Doi, K. Kawano, and N. Hara, Pitting corrosion resistance of martensite of AISI 1045 steel and the beneficial role of interstitial carbon, Journal of the Electrochemical Society 164, C962 (2017).
- [20] S. Kumar, A. Kumar, Vinaya, R. Madhusudhan, R. Sah, and S. Manjini, Mechanical and Electrochemical Behavior of Dual-Phase Steels Having Varying Ferrite—Martensite Volume Fractions, Journal of Materials Engineering and Performance 28, 3600 (2019).
- [21] V. A. Esin, B. Denand, Q. Le Bihan, M. Dehmas, J. Teixeira, G. Geandier, S. Denis, T. Sourmail, and E. Aeby-Gautier, *In situ synchrotron x-ray diffraction and dilatometric study of austenite formation in a multi-component steel:*Influence of initial microstructure and heating rate, Acta materialia **80**, 118 (2014).
- [22] L. Onyeji and G. Kale, *Preliminary Investigation of the Corrosion Behavior of Proprietary Micro-alloyed Steels in Aerated and Deaerated Brine Solutions*, Journal of Materials Engineering and Performance **26**, 5741 (2017).
- [23] Y. bing Guo, C. Li, Y. chang Liu, L. ming Yu, Z. qing Ma, C. xi Liu, and H. jun Li, Effect of microstructure variation on the corrosion behavior of high-strength low-alloy steel in 3.5wt% NaCl solution, International Journal of Minerals, Metallurgy and Materials 22, 604 (2015).
- [24] T. Mehner, R. Morgenstern, P. Frint, I. Scharf, M. F. Wagner, and T. Lampke, Corrosion characteristics of a quenching and partitioning steel determined by electrochemical impedance spectroscopy, IOP Conference Series: Materials Science and Engineering 373 (2018).
- [25] M. Mandel, F. Böhme, M. Hauser, M. Wendler, F. Tuchscheerer, and L. Krüger, The Influence of Plastic Deformation on the Corrosion Behavior of a Cast High-Alloy CrMnNi TRIP Steel, Steel Research International 87, 1105 (2016).
- [26] V. Rault, V. Vignal, H. Krawiec, and O. Tadjoa, *Corrosion behaviour of heavily deformed pearlitic and brass-coated pearlitic steels in sodium chloride solutions*, Corrosion Science **86**, 275 (2014).

References 87

[27] S. Zhang, X. Pang, Y. Wang, and K. Gao, *Corrosion behavior of steel with different microstructures under various elastic loading conditions*, Corrosion Science **75**, 293 (2013).

- [28] K. Ralston and N. Birbilis, *Effect of grain size on corrosion: a review,* Corrosion **66**, 075005 (2010).
- [29] G. Aydin and A. Yazici, Effect of quenching and tempering temperature on corrosion behavior of boron steels in 3.5 wt.% NaCl solution, International Journal of Electrochemical Science 14, 2126 (2019).
- [30] M. Soleimani, H. Mirzadeh, and C. Dehghanian, *Processing Route Effects on the Mechanical and Corrosion Properties of Dual Phase Steel*, Metals and Materials International (2019).
- [31] K. chang Shen, G. hua Li, Y. min Sun, Y. gang Wang, Y. jie Li, G. hui Cao, and W. min Wang, Linking anisotropy with Fe3C distribution in AISI 1045 steel, International Journal of Minerals, Metallurgy and Materials 22, 1293 (2015).
- [32] K. Fushimi, R. Nakagawa, Y. Kitagawa, and Y. Hasegawa, *Micro- And nano-scopic aspects of passive surface on pearlite structure of carbon steel in pH 8.4 boric acid-borate buffer,* Journal of the Electrochemical Society **166**, C3409 (2019).
- [33] P. K. Katiyar, S. Misra, and K. Mondal, Effect of Different Cooling Rates on the Corrosion Behavior of High-Carbon Pearlitic Steel, Journal of Materials Engineering and Performance 27, 1753 (2018).
- [34] C. Yu, X. Gao, and P. Wang, *Electrochemical corrosion performance of low alloy steel in acid sodium chloride solution*, *Electrochemistry* **83**, 406 (2015).
- [35] M. Shahzad, Q. Tayyaba, T. Manzoor, R. Ud-Din, T. Subhani, and A. H. Qureshi, The effects of martensite morphology on mechanical properties, corrosion behavior and hydrogen assisted cracking in A516 grade steel, Materials Research Express 5 (2018).
- [36] R. Nadlene, H. Esah, S. Norliana, and M. A. Mohd Irwan, *Study on the effect of volume fraction of dual phase steel to corrosion behaviour and hardness,* World Academy of Science, Engineering and Technology **50**, 564 (2011).
- [37] K. Fushimi, K. Yanagisawa, T. Nakanishi, Y. Hasegawa, T. Kawano, and M. Kimura, *Microelectrochemistry of dual-phase steel corroding in 0.1 M sul-furic acid*, Electrochimica Acta 114, 83 (2013).
- [38] J. Guo, S. Yang, C. Shang, Y. Wang, and X. He, *Influence of carbon content and microstructure on corrosion behaviour of low alloy steels in a Cl- containing environment*, Corrosion Science **51**, 242 (2009).

- [39] L. Lapeire, E. M. Lombardia, K. Verbeken, I. De Graeve, L. Kestens, and H. Terryn, *Effect of neighboring grains on the microscopic corrosion behavior of a grain in polycrystalline copper*, Corrosion Science **67**, 179 (2013).
- [40] E. Martinez-Lombardia, Y. Gonzalez-Garcia, L. Lapeire, I. De Graeve, K. Verbeken, L. Kestens, J. M. Mol, and H. Terryn, Scanning electrochemical microscopy to study the effect of crystallographic orientation on the electrochemical activity of pure copper, Electrochimica Acta 116, 89 (2014).
- [41] K. Fushimi, K. Miyamoto, and H. Konno, *Anisotropic corrosion of iron in pH 1 sulphuric acid*, Electrochimica Acta **55**, 7322 (2010).
- [42] Z. Wang, P. Li, Y. Guan, Q. Chen, and S. Pu, *The corrosion resistance of ultra-low carbon bainitic steel,* Corrosion Science **51**, 954 (2009).
- [43] Y. Si, *Investigation of Galvanic Corrosion Behavior of Dual Phase Steel,* ECS Transactions **72**, 13 (2016).
- [44] W. Handoko, F. Pahlevani, and V. Sahajwalla, *The effect of low-quantity Cr addition on the corrosion behaviour of dual-phase high carbon Steel,* Metals **8**, 2 (2018).
- [45] W. Handoko, F. Pahlevani, and V. Sahajwalla, *Corrosion Behaviour of Dual-Phase High Carbon Steel—Microstructure Influence*, Journal of Manufacturing and Materials Processing **1**, 21 (2017).
- [46] T. Haisch, E. J. Mittemeijer, and J. W. Schultze, *On the influence of microstructure and carbide content of steels on the electrochemical dissolution process in aqueous NaCl-electrolytes,* Materials and Corrosion **53**, 740 (2002).
- [47] S. Qu, X. Pang, Y. Wang, and K. Gao, Corrosion behavior of each phase in low carbon microalloyed ferrite-bainite dual-phase steel: Experiments and modeling, Corrosion Science **75**, 67 (2013).
- [48] A. P. Moon, S. Sangal, S. Layek, S. Giribaskar, and K. Mondal, Corrosion Behavior of High-Strength Bainitic Rail Steels, Metallurgical and Materials Transactions A: Physical Metallurgy and Materials Science 46, 1500 (2015).
- [49] K. Yanagisawa, T. Nakanishi, Y. Hasegawa, and K. Fushimi, *Passivity of dual-phase carbon steel with ferrite and martensite phases in pH 8.4 boric acid-borate buffer solution,* Journal of the Electrochemical Society **162**, C322 (2015).
- [50] J. Wei, J. Dong, Y. Zhou, X. He, C. Wang, and W. Ke, Influence of the secondary phase on micro galvanic corrosion of low carbon bainitic steel in NaCl solution, Materials Characterization 139, 401 (2018).
- [51] T. V. Shibaeva, V. K. Laurinavichyute, G. A. Tsirlina, A. M. Arsenkin, and K. V. Grigorovich, The effect of microstructure and non-metallic inclusions on corrosion behavior of low carbon steel in chloride containing solutions, Corrosion Science 80, 299 (2014).

References 89

[52] L. R. Bhagavathi, G. Chaudhari, and S. Nath, *Mechanical and corrosion behavior of plain low carbon dual-phase steels*, Materials & Design **32**, 433 (2011).

- [53] A. M. Ramirez-Arteaga, J. G. Gonzalez-Rodriguez, B. Campillo, C. Gaona-Tiburcio, G. Dominguez-Patiño, L. Leduc Lezama, J. G. Chacon-Nava, M. A. Neri-Flores, and A. Martinez-Villafañe, An electrochemical study of the corrosion behavior of a dual phase steel in 0.5m H2SO4, International Journal of Electrochemical Science 5, 1786 (2010).
- [54] L. yun Zhang, D. Wu, and Z. Li, *Influence of Alloying Elements on Mechanical Properties and Corrosion Resistance of Cold Rolled C-Mn-Si TRIP Steels*, Journal of Iron and Steel Research International **19**, 42 (2012).
- [55] I. J. Park, S. M. Lee, M. Kang, S. Lee, and Y. K. Lee, *Pitting corrosion behavior in advanced high strength steels*, Journal of Alloys and Compounds 619, 205 (2015).
- [56] J. G. Speer, F. C. R. Assunção, D. K. Matlock, and D. V. Edmonds, *The "quenching and partitioning" process: background and recent progress,* Materials Research **8**, 417 (2005).
- [57] M. Santofimia, C. Kwakernaak, W. Sloof, L. Zhao, and J. Sietsma, Experimental study of the distribution of alloying elements after the formation of epitaxial ferrite upon cooling in a low-carbon steel, Materials Characterization 61, 937 (2010).
- [58] Y. Takabatake, K. Fushimi, T. Nakanishi, and Y. Hasegawa, Grain-dependent passivation of iron in sulfuric acid solution, Journal of the Electrochemical Society 161, C594 (2014).
- [59] Y. Takabatake, Y. Kitagawa, T. Nakanishi, Y. Hasegawa, and K. Fushimi, Heterogeneity of a thermal oxide film formed on polycrystalline iron observed by two-dimensional ellipsometry, Journal of the Electrochemical Society 163, C815 (2016).
- [60] Z. fen Wang, F. xing Yin, L. xin Wu, Y. qiang Sun, and W. lin Zhang, Corrosion Resistance on High Strength Bainitic Steel and 09CuPCrNi After Wet-Dry Cyclic Conditions, Journal of Iron and Steel Research International 20, 72 (2013).
- [61] R. V. Morris, H. V. Lauer Jr., C. A. Lawson, E. K. Gibson Jr., G. A. Nace, and C. Stewart, Spectral and other physicochemical properties of submicron powders of hematite, mghemite, magnetite, goethite, and lepidocrocite, J. Geophys. Res. 90, 3126 (1985).
- [62] D. D. MacDonald, The history of the Point Defect Model for the passive state: A brief review of film growth aspects, Electrochimica Acta **56**, 1761 (2011).
- [63] Y. Takabatake, Y. Kitagawa, T. Nakanishi, Y. Hasegawa, and K. Fushimi, *Grain dependency of a passive film formed on polycrystalline iron in pH 8.4 borate solution*, Journal of the Electrochemical Society **164**, C349 (2017).

- [64] H. Gerengi, N. Sen, I. Uygur, and E. Kaya, *Corrosion behavior of dual phase* 600 and 800 steels in 3.5 wt.% NaCl environment, Journal of Adhesion Science and Technology, 1 (2019).
- [65] M. Ferhat, A. Benchettara, S. Amara, and D. Najjar, *Corrosion behaviour of fe-c alloys in a sulfuric medium,* J. Mater. Environ. Sci **5**, 1059 (2014).
- [66] J. W. Wilder, C. Clemons, D. Golovaty, K. L. Kreider, G. W. Young, and R. S. Lillard, *An adaptive level set approach for modeling damage due to galvanic corrosion*, Journal of Engineering Mathematics **91**, 121 (2015).
- [67] D. Höche and J. Isakovic, *Level-Set modelling of galvanic corrosion of Magnesium*, Conference Paper (2012).
- [68] R. Radouani, Y. Echcharqy, and M. Essahli, *Numerical Simulation of Galvanic Corrosion between Carbon Steel and Low Alloy Steel in a Bolted Joint,* International Journal of Corrosion **2017** (2017).
- [69] J. X. Jia, A. Atrens, G. Song, and T. H. Muster, Simulation of galvanic corrosion of magnesium coupled to a steel fastener in NaCI solution, Materials and Corrosion 56, 468 (2005).
- [70] L. A. Shaik and S. K. Thamida, Surface evolution of a corroding metal as a moving boundary problem by random assignment of anodic and cathodic sites, Journal of Electroanalytical Chemistry **780**, 264 (2016).
- [71] L. A. Shaik and S. K. Thamida, Simulation of corrosion of a dual phase alloy steel based on its constituent phase polarization properties, Materialia 2, 183 (2018).
- [72] K. B. Deshpande, *Numerical modeling of micro-galvanic corrosion*, Electrochimica Acta **56**, 1737 (2011).
- [73] L. Yin, Y. Jin, C. Leygraf, and J. Pan, A FEM model for investigation of micro-galvanic corrosion of Al alloys and effects of deposition of corrosion products, Electrochimica Acta 192, 310 (2016).
- [74] O. Guseva, J. A. Derose, and P. Schmutz, *Modelling the early stage time dependence of localised corrosion in aluminium alloys,* Electrochimica Acta 88, 821 (2013).
- [75] L. C. Abodi, J. A. Derose, S. Van Damme, A. Demeter, T. Suter, and J. Deconinck, *Modeling localized aluminum alloy corrosion in chloride solutions under non-equilibrium conditions: Steps toward understanding pitting initiation*, Electrochimica Acta **63**, 169 (2012).
- [76] J. Xiao and S. Chaudhuri, *Predictive modeling of localized corrosion: An application to aluminum alloys*, Electrochimica Acta **56**, 5630 (2011).

References 91

[77] P. T. Brewick, N. Kota, A. C. Lewis, V. G. DeGiorgi, A. B. Geltmacher, and S. M. Qidwai, *Microstructure-sensitive modeling of pitting corrosion: Effect of the crystallographic orientation*, Corrosion Science 129, 54 (2017).

- [78] N. Kota, S. M. Qidwai, A. C. Lewis, and V. G. DeGiorgi, *Microstructure-Based Numerical Modeling of Pitting Corrosion in 316 Stainless Steel, ECS Transactions* **50**, 155 (2013).
- [79] I. S. Cole, T. H. Muster, N. S. Azmat, M. S. Venkatraman, and A. Cook, *Multiscale modelling of the corrosion of metals under atmospheric corrosion*, Electrochimica Acta **56**, 1856 (2011).
- [80] Q. Zhang, Z. Ye, Z. Zhu, X. Liu, J. Zhang, and F. Cao, Separation and kinetic study of iron corrosion in acidic solution via a modified tip generation/substrate collection mode by SECM, Corrosion Science **139**, 403 (2018).
- [81] S. Das Bakshi, P. H. Shipway, and H. K. Bhadeshia, *Three-body abrasive wear of fine pearlite, nanostructured bainite and martensite*, Wear (2013).
- [82] K. H. Kim, S. H. Lee, N. D. Nam, and J. G. Kim, Effect of cobalt on the corrosion resistance of low alloy steel in sulfuric acid solution, Corrosion Science (2011).
- [83] Z. Panossian, N. L. de Almeida, R. M. F. de Sousa, G. d. S. Pimenta, and L. B. S. Marques, *Corrosion of carbon steel pipes and tanks by concentrated sulfuric acid: A review, Corrosion Science* (2012).
- [84] L. Jinlong and L. Hongyun, *The effects of cold rolling temperature on corrosion resistance of pure iron,* Applied Surface Science (2014).
- [85] X. Q. Cheng, F. L. Sun, S. J. Lv, and X. G. Li, *A new steel with good low-temperature sulfuric acid dew point corrosion resistance*, Materials and Corrosion (2012).
- [86] C. H. Hsu and F. Mansfeld, Concerning the conversion of the constant phase element parameter Y0 into a capacitance, Corrosion (2001).
- [87] L. Freire, X. R. Nóvoa, M. F. Montemor, and M. J. Carmezim, Study of passive films formed on mild steel in alkaline media by the application of anodic potentials, Materials Chemistry and Physics 114, 962 (2009).
- [88] S. Joiret, M. Keddam, X. R. Nóvoa, M. C. Pérez, C. Rangel, and H. Takenouti, Use of EIS, ring-disk electrode, EQCM and Raman spectroscopy to study the film of oxides formed on iron in 1 M NaOH, Cement and Concrete Composites (2002).
- [89] K. Azumi, T. Ohtsuka, and N. Sato, *Mott Schottky Plot of the Passive Film Formed on Iron in Neutral Borate and Phosphate Solutions, Journal of The Electrochemical Society* **134**, 1352 (1987).

92 References

[90] A. Kalhor, M. Soleimani, H. Mirzadeh, and V. Uthaisangsuk, *A review of recent progress in mechanical and corrosion properties of dual phase steels,* Archives of Civil and Mechanical Engineering **20** (2020).

- [91] J. Wang, Z. Wang, B. Huang, Y. Ma, Y. Liu, X. Qin, X. Zhang, and Y. Dai, Oxygen vacancy induced band-gap narrowing and enhanced visible light photocatalytic activity of ZnO, ACS Applied Materials and Interfaces (2012).
- [92] E. Paterson, *The Iron Oxides. Structure, Properties, Reactions, Occurrences and Uses,* Clay Minerals (1999).
- [93] L. Hamadou, A. Kadri, and N. Benbrahim, *Characterisation of passive films formed on low carbon steel in borate buffer solution (pH 9.2) by electrochemical impedance spectroscopy*, Applied Surface Science (2005).



Polarisation Data

This section presents the corrosion data collected from the literature. It contains active corrosion behaviour for different microstructure and processing conditions.

Table A.1: Polarisation data collected from the literature.

| Research | Processing | Microstructure Details | Volume Fraction | Carbon Content (wt.%) | Environment | $\mathbf{E}_{\mathrm{corr}}$ (V) vs. SHE | $i_{\rm corr} (\mu A/cm^2)$ |
|--|---------------------------|--|---|-----------------------|---------------|--|-----------------------------|
| Sarkar et al. | Annealing | Ferrite-pearlite | 0.27 pearlite | 0.20 | 3.5wt.% NaCl | -0.244 | 19.14 |
| (2005) [13] 1 | | Ferrite-chain martensite | 0.33 martensite | 0.20 | | -0.284 | 32.29 |
| | | | 0.46 martensite | 0.20 | | -0.228 | 50.26 |
| | | Uniform fine fibrous ferrite-martensite | 0.36 martensite | 0.20 | | -0.291 | 63.36 |
| | | Uniform fibrous ferrite-martensite | 0.47 martensite | 0.20 | | -0.285 | 73.60 |
| | | Island martensite in continuous ferrite matrix | 0.48 martensite | 0.20 | | -0.273 | 46.06 |
| Qu et al. | Annealing | Bainite | | 0.08 | 3.5wt.% NaCl | | |
| $(2013)[47]^{2}$ | | Ferrite-bainite (resembles island morphology) | 1 | 0.08 | | | |
| Fushimi et al. | Hot rolling, | Ferrite | | 0.01 | $0.1MH_2SO_4$ | -0.278 | 79 |
| $(2013)[37]^3$ | cold rolling, | Ferrite-martensite (75% ferrite) | 0.79 ferrite | 0.01 | | -0.267 | 107 |
| | annealing | Ferrite-martensite (50% ferrite) | 0.54 ferrite | 0.20 | | -0.252 | 135 |
| | | Ferrite-martensite (25% ferrite) Martensite | 0.25 ferrite | 0.31 0.41 | | -0.238 -0.230 | 191 247 |
| Barraza-Fiero et | Hot rolling and | Martensite-bainite | 0.56 martensite 0.32 bai- | 0.03 | NS4, 3.5wt.% | | |
| al. | annealing | | nite | | NaCl, 0.1M- | | |
| (2014) [18] ⁴ | | Bainite-martensite/austenite | 0.98 bainite 0.02 marten- | 0.02 | $3MH_2SO_4$ | | |
| | | | site/austenite | | | | |
| | | Ferrite-martensite/austenite | 0.95 ferrite 0.03 marten- site/austenite | 0.03 | | | |
| Guo et al. | Annealing | Polygonal ferrite-pearlite (cooling rate: 0.1°C/s) | | 0.09 | 3.5wt.% NaCl | -0.364 -0.339 | 6.89 |
| | | Martensite (cooling rate: 50° C/s) | | 0.09 | | -0.408 | 7.08 |
| Yu et. al | Annealing | Acicular ferrite (cooling rate: 10.4°C/s) | | 60.0 | 10wt.% NaCl | -0.254 | 86.4 |
| (2015) [34] ⁵ | | Acicular ferrite (cooling rate: 12.8°C/s) | | 60.0 | (pH 0.85, HCl | -0.234 | 76.9 |
| | | 등 | | 0.09 | modified) | -0.232 | 58.8 |
| Salamci et al. (2017) [16] ⁶ | Hot rolling and annealing | Martensite-ferrite | 0.25 martensite 0.0 epi- taxial ferrite | 60.0 | 3.5wt.% NaCl | -0.491 | 2.11 |
| |) | Martensite-ferrite | 0.25 martensite 0.1 epi- | 0.09 | | 0.052 | 2.39 |
| | | | taxial territe | | | 1 | |
| | | Martensite-Territe | 0.35 martensite 0.0 epi- taxial ferrite | 60.0 | | 0.0/3 | 14.5 |
| | | Martensite-ferrite | 0.37 martensite 0.15 epi- taxial ferrite | 0.09 | | 0.613 | 3.11 |
| Moon et al. | Hot rolling | Pearlite (coarser) (conventional C-Mn) | | 0.71 | 0.6M NaCl | -0.311 | 14.8 |
| (2015)[48] ⁷ | and annealing | Pearlite (finer) (Cr-Cu-Ni microalloyed) | | 0.71 | | -0.282 | 17.7 |
| | | | | | | | |

All E_{corr} results were positive in the original paper, results are probably missing a minus sign so all of them are treated as negative.

In this paper, the carbon content of each phase was aimed to be the same in different volume fractions of phases to cancel the effect of this parameter, no matter the chemical composition ²The behaviour of polarisation curves makes it harder to generate corrosion data in an approximate manner. Polarisation graphs are found on Fig.4 of the original paper.

Polarisation measurements are found on Fig.8 of the original paper. Corrosion behaviour changed minimally with different microstructures. That doesn't mean corrosion is not contolled by microstructure, the different strains during thermomechanical treatments and different cooling rates hinder isolating individual causes behind the corrosion response. in every sample: expected carbon content in ferrite is 0.015, in martensite 0.41.

Apart from acicular ferrite; quasi-polygonal ferrite, granular ferrite and bainite ferrite were also part of the microstructure.

Samples are immersed for 60 minutes before polarisation measurements, it could be the reason for positive E_{corr} and low i_{corr} results.

First sample have conventional C-Mn composition, rest are microalloyed with Cr-Cu-Ni.

| ŏ |
|----------|
| ā |
| ᅀ |
| 2 |
| ₹ |
| 2 |
| 8 |
| 2 |
| σ |
| _ |
| 5 |
| ≅ |
| - |
| 찡 |
| = |
| = |
| ≣ |
| Ξ |
| Ö |
| o |
| ∹ |
| ⋖ |
| a) |
| ÷. |
| 윤 |
| <u> </u> |
| |

| Research | Processing | Microstructure Details | Volume Fraction | Carbon Content (wt.%) | Environment | $\mathbf{E}_{\mathrm{corr}}$ (V) vs. SHE | $i_{corr} (\mu A/cm^2)$ |
|-------------------------------|------------------------------|---|--|-----------------------|---------------------|--|-------------------------|
| | | Bainite (Cr-Cu-Ni microalloyed) (soaked at 900°C 10 | | 0.71 | | -0.428 | 17.4 |
| | | niii.) Bainite (Cr-Cu-Ni microalloyed) (soaked at 900°C 30 min) | | 0.71 | | -0.453 | 19.2 |
| | | Bainite (Cr-Cu-Ni microalloyed) (soaked at 900°C 60 | | 0.71 | | -0.446 | 13.8 |
| | | min) Bainite (Cr-Cu-Ni microalloyed) (soaked at 900°C 120 min) | | 0.71 | | -0.469 | 19.5 |
| Handoko et al. (2018) | 1 1 | Martensite-austenite (chromium 0.1-0.18%) Martensite-austenite (chromium 0.6-0.8%) Martensite-austenite (chromium 1.0-0.8%) | 0.5 retained austenite 0.5 retained austenite | 1.00 | 0.1M NaCl | -0.454 -0.436 | 9.92 9.84 |
| [44] | - | allice | o.o retained austeriite | 1.00 | | -0.350 | 2.90 |
| Katiyar et al. (2018) [33] | Annealing | Pearlite (coarse) Pearlite (medium) | | 0.70 0.70 | 3.5wt.% NaCl | -0.402 -0.406 | 14.55 9.04 |
| | | Pearlite (fine) | | 0.70 | | -0.475 | 4.75 |
| | | Pearlite (very fine) | | 0.70 | | -0.488 | 6.28 |
| Zhang et al. | Hot rolling | Bainitic (granular bainite + quasi-polygonal ferrite) (no load) | | 0.08 | 3.5wt.% NaCl | -0.446 | 10.40 |
| (2013) [27] ⁸ | and annealing | Baintic (granular bainite + quasi-polygonal ferrite) (0.7 | | 0.08 | | -0.454 | 12.95 |
| | | or yietu suess uyrianını todu). Bainitic (granular bainite + quasi-polygonal ferrite) (0.7 of yield stress constant load). | | 0.08 | | -0.467 | 14.77 |
| Osorio et al. (2009) [12] | Hot rolling | Pearlite - ferrite (as received/hot rolling) (mean grain size: 55 µm) | 0.27 pearlite | 0.19 | 0.5M NaCl (pH | -0.462 | 10.5 |
| []() | Normalising | Peraite (normalising) (mean grain size: 35 μm) (cooling: air 5°C/min) | 0.23 pearlite | 0.19 | (5:5) | -0.347 | 7.5 |
| | Annealing | Pearlite - ferrite (annealing) (mean grain size: 70 µm) (cooling - firmace 200/h) | 0.25 pearlite | 0.19 | | -0.439 | 12.8 |
| | Intercritical An- nealing | Martensite - ferrite (intercritical annealing) (cooling: ice water quenching, 380°C/s) | 0.54 martensite | 0.19 | | -0.416 | 11.0 |
| Shahzad et al. (2018) | Annealing | Martensite - ferrite (bulk martensite morphology) (martensite Content: 0.3) | 0.5 martensite | 0.20 | Boric Acid (pH 5.5) | -0.398 | 8.130 |
| [35] | | Martensite - ferrite (fibrous martensite morphology) | 0.5 martensite | 0.20 | | -0.336 | 19.10 |
| | | (martensite C content: 0.25) Pearlite - ferrite (mean ferrite grain size: 25 μm) | 0.4 pearlite | 0.20 | | -0.388 | 12.40 |
| Kayali et al. | Annealing | Ferrite-pearlite | | 0.15 | 3.5wt.% NaCl | -0.460 | 2.424 |
| $(2013)[15]^{10}$ | | Ferrite-chain martensite (boronised) | 0.32 martensite | 0.15 | | -0.498 | 3.664 |
| | | island marcensite in continuous remite matrix (boro-nised) | סיסד ווומן נבווצונב | O.13 | | .0.33 | 5.0.5 |
| | | Island ferrite in continuous martensite matrix (boro- | 0.81 martensite | 0.15 | | -0.525 | 5.946 |
| | | niseu) Ferrite-chain martensite (normal) | 0.32 martensite | 0.15 | | -0.476 | 6.738 |
| | | | | | | | |

⁸i_{corr} values on the polarisation curve and table were inconsistent. A calculation mistake must've occurred on the source paper when carrying data from the curve to the table; a correction that matches the polarisation curve is applied. For more information check Fig. 6 and Table 5 of the paper. ⁹Polarisation equipment is not mentioned. It is assumed that SCE is used.

¹⁰In the source paper the values given were around thousands, for instance i_{corr} of the first sample was 2424 $\mu A/cm^2$. This is probably an error caused by misreading of a comma, so results given here are one thousandth of the results given in the original paper.

| a) |
|----------|
| Ď |
| w. |
| 12 |
| ч |
| S |
| === |
| _ |
| 0 |
| • |
| 2 |
| a) |
| _ |
| ≏ |
| = |
| = |
| ± |
| 0 |
| |
| - |
| 8 |
| T) |
| ≝ |
| _ |
| _ |
| Ξ. |
| Ξ |
| ⋤ |
| 0 |
| o |
| ٠. |
| - |
| • |
| ⋖ |
| |
| <u>•</u> |
| ⇁ |
| ₽ |
| σ. |
| _ |

| | | | office of the control | | | | |
|------------------------------|----------------------------|---|--|-----------------------|-----------------|--|------------------------------|
| Research | Processing | Microstructure Details | Volume Fraction | Carbon Content (wt.%) | Environment | $\mathbf{E}_{\mathrm{corr}}$ (V) vs. SHE | $_{(\mu A/cm^2)}^{i_{corr}}$ |
| | | Island martensite in continuous ferrite matrix (normal) | 0.61 martensite | 0.15 | | -0.482 | 12.118 |
| | | [] | 0.01 Illaltelisite | 0.13 | | -0.43J | 17.007 |
| Nadlene et al. (2011) | Hot rolling and | Ferrite-martensite Ferrite-martensite | 0.1545 martensite 0.245 martensite | 0.23 | 5wt.% NaCl | | 11.1 |
| [36] | intercritical | Ferrite-martensite | 0.47 martensite | 0.23 | | | 16.8 |
| | annealing | Ferrite-martensite | 0.58 martensite | 0.23 | | | 21.9 |
| |) | Ferrite-martensite | 0.74 martensite | 0.23 | | | 22.3 |
| | | | 0.9345 martensite | 0.23 | | 1 | 22.5 |
| Kumar et al. | Annealing | Ferrite-pearlite (as rolled) | | 0.16 | 3.5wt.% NaCl | -0.419 | 7.68 |
| (2019) [<mark>20</mark>] | | Ferrite-martensite (intercritical annealing temperature: 760°C) | 0.32 martensite | 0.16 | | -0.386 | 98'9 |
| | | Ferrite-martensite (intercritical annealing temperature: 780°C) | 0.41 martensite | 0.16 | | -0.416 | 7.15 |
| | | Ferrite-martensite (intercritical annealing temperature: 800°C) | 0.49 martensite | 0.16 | | -0.394 | 7.95 |
| | | Ferrite-martensite (intercritical annealing temperature: 820°C) | 0.63 martensite | 0.16 | | -0.417 | 7.2 |
| | | Ferrite-martensite (intercritical annealing temperature: 840°C) | 0.81 martensite | 0.16 | | -0.396 | 7.37 |
| | | Ferrite-martensite (intercritical annealing temperature: 860°C) | fully martensite | 0.16 | | -0.397 | 7.69 |
| | | Ferrite-martensite (intercritical annealing temperature: 880°C) | fully martensite | 0.16 | | -0.407 | 7.27 |
| Ling-Yun et al. (2012) | Hot rolling, cold rolling, | Polygonal ferrite-granular bainite-retained austen- ite(conventional TRIP steel) | | 0.11 | 3.5wt.% NaCl | -0.359 | 40 |
| [54] ¹¹ | intercritical | Pearlite-ferrite (conventional weathering steel) | | 0.08 | | -0.459 | 10 |
| | allicallig | Frankphase su ducture: Terrine marix wurd a dispersion or abanite, mestancher er terrine daustenite, martensite (conventional TRIP steel with Al, Cu, Cr, Mo, Ni) | | 0.10 | | 6000 | o |
| Onyeji et al. (2017) [22] | | Ferrite-pearlite (Average grain size: 68.5 μm) Ferrite-pearlite (Average grain size: 46.6 μm) | 63.6 ferrite 57.5 ferrite | 0.12 0.12 | 3.5wt.% NaCl | -0.391 -0.381 | 21 21.5 |
| | 1 1 | Ferrite-pearlite (Average grain size: 20.6 µm) Bainite with evenly distributed acicular ferrite (Average | 48.2 ferrite - | 0.22 0.25 | | -0.392 -0.382 | 24 28 |
| 10 10 10 10 10 | | grain size: 14.7 µm) | | 0.17 | O Evet 07 Nin C | 0.215 | 13 |
| (2019) [64] | | DP-600 | | 0.09 | 3.3WL. % IVdCI | -0.433 | 17 |
| | | | | | | | |

¹¹Data manually generated from polarisation curves in an approximate manner. Polarisation measurements are found on Fig.4 of the original paper.

B

Model Input Parameters

The tables in this section contain input values used to model micro-galvanic corrosion for different volume fractions. Table B.1 contains the values used to simulate ferrite-martensite microstructure while table B.2 contains the values used to simulate ferrite-pearlite microstructure.

Table B.1: Input parameters for the ferrite-martensite microstructure simulation.

| Name | Value | Description |
|--------------------|--------------------|---|
| sigma | 5 [S/m] | 0.1M sulfuric acid conductivity |
| E_eq_anode | -0.274 [V] | Equilibrium potential for the anode - ferrite |
| i_eq_anode | $0.79 [A/m^2]$ | Exchange current density for the anode - ferrite |
| a_anodic_anode | 39 [mV] | Anodic tafel slope for the iron dissolution reaction - ferrite |
| a_cathodic_anode | -113.8 [mV] | Cathodic tafel slope for the iron dissolution reaction - ferrite |
| E_eq_cathode | -0.230 [V] | Equilibrium potential for the cathode - martensite |
| i_eq_cathode | $2.74 [A/m^2]$ | Exchange current density for the cathode - martensite |
| a_anodic_cathode | 40.4 [mV] | Anodic tafel slope for the iron dissolution reaction - martensite |
| a_cathodic_cathode | -100.4 [mV] | Cathodic tafel slope for the iron dissolution reaction - martensite |
| external_V | 0 [V] ¹ | External electric potential applied during potential sweep |

Table B.2: Input parameters for the ferrite-pearlite microstructure simulation.

| Name | Value | Description |
|--------------------|--------------------|---|
| sigma | 5 [S/m] | 0.1M sulfuric acid conductivity |
| E_eq_anode | -0.746 [V] | Equilibrium potential for the anode - ferrite |
| i_eq_anode | $0.01 [A/m^2]$ | Exchange current density for the anode - ferrite |
| a_anodic_anode | 39 [mV] | Anodic tafel slope for the iron dissolution reaction - ferrite |
| a_cathodic_anode | -113.8 [mV] | Cathodic tafel slope for the iron dissolution reaction - ferrite |
| E_eq_cathode | -0.652 [V] | Equilibrium potential for the cathode - pearlite |
| i_eq_cathode | $0.06 [A/m^2]$ | Exchange current density for the cathode - pearlite |
| a_anodic_cathode | 40.4 [mV] | Anodic tafel slope for the iron dissolution reaction - pearlite |
| a_cathodic_cathode | -100.4 [mV] | Cathodic tafel slope for the iron dissolution reaction - pearlite |
| external_V | 0 [V] ² | External electric potential applied during potential sweep |

 $^{^{1}}$ Potential is sweeped from -0.4 V to -0.1 V.

 $^{^{2}}$ Potential is sweeped from -0.9 V to -0.5 V.



Simulated Potentiodynamic Polarisation Plots

The simulated potentiodynamic polarisation plots for different volume fractions and phase constituents are presented in this section.

C.1. Ferrite-Martensite Microstructure Simulated Potentiodynamic Polarisation Plots

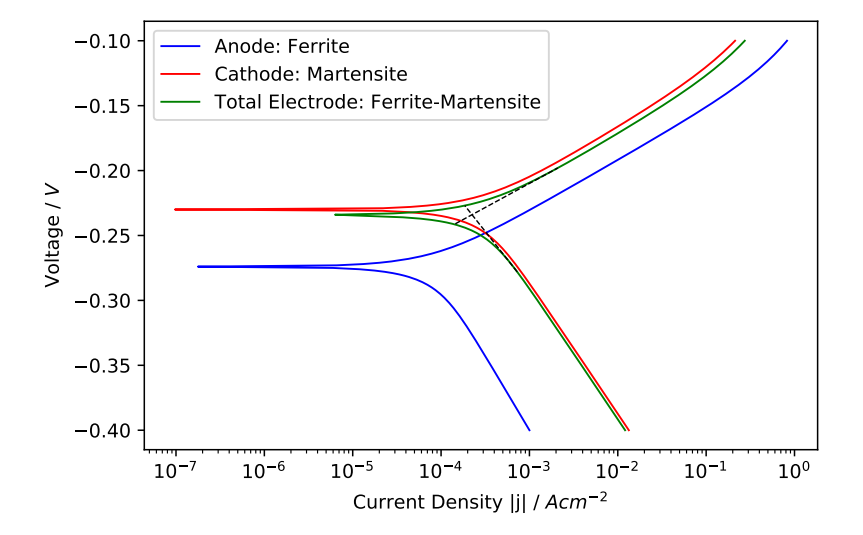


Figure C.1: Simulated potentiodynamic polarisation curve for the 10% ferrite 90% martensite microstructure.

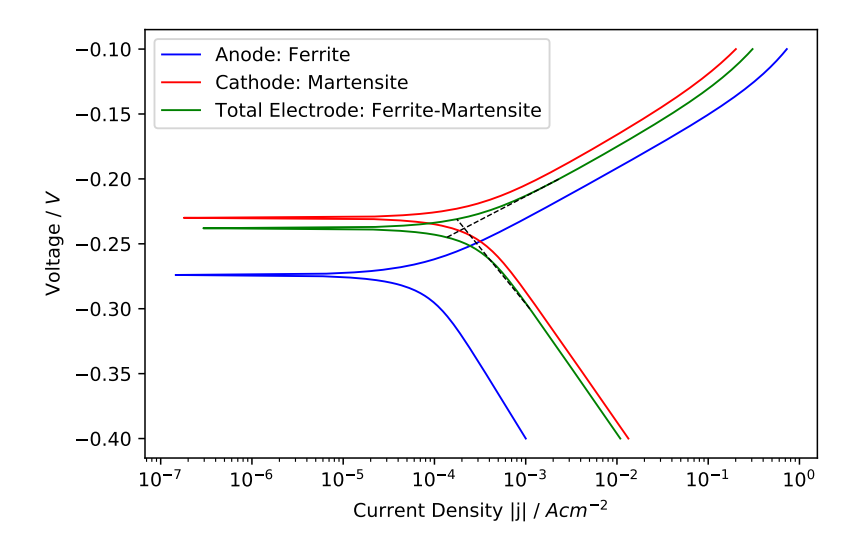


Figure C.2: Simulated potentiodynamic polarisation curve for the 20% ferrite 80% martensite microstructure.

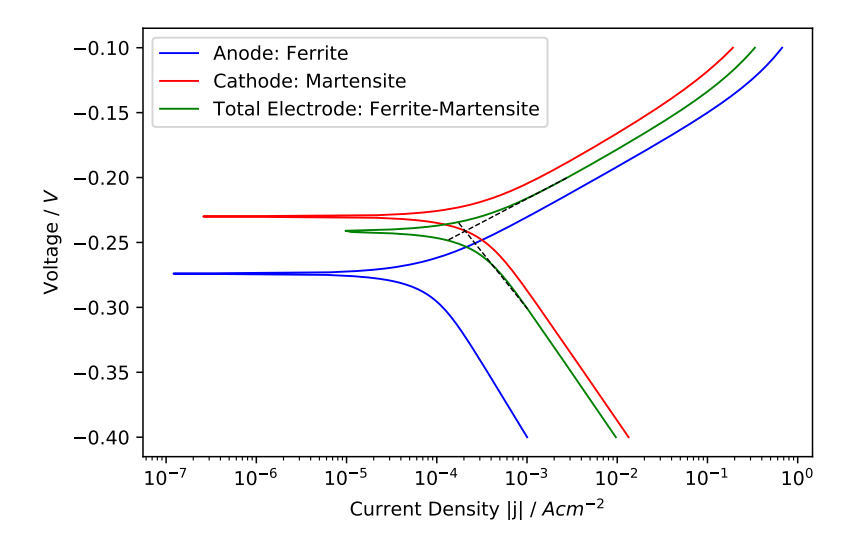


Figure C.3: Simulated potentiodynamic polarisation curve for the 30% ferrite 70% martensite microstructure.

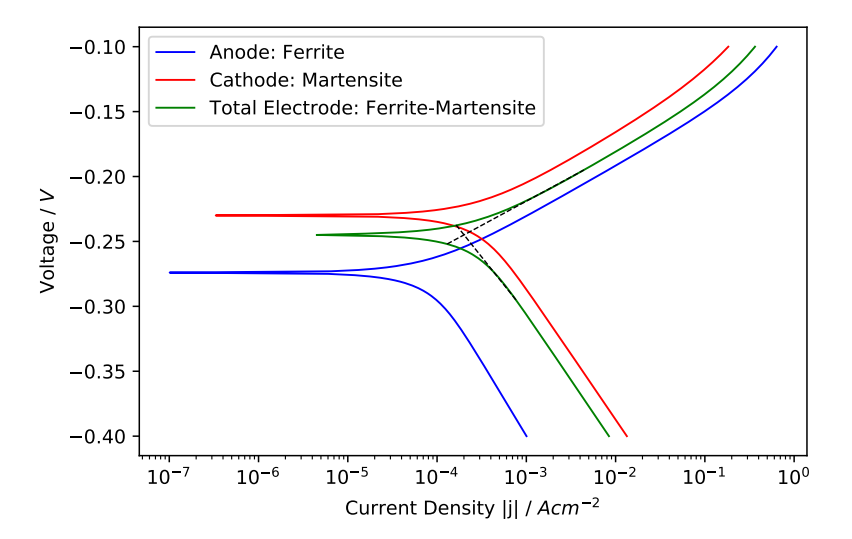


Figure C.4: Simulated potentiodynamic polarisation curve for the 40% ferrite 60% martensite microstructure.

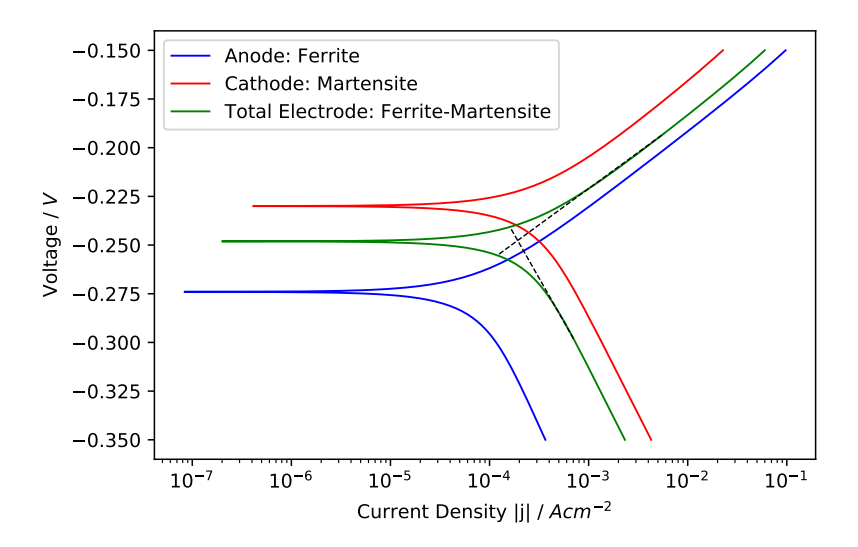


Figure C.5: Simulated potentiodynamic polarisation curve for the 50% ferrite 50% martensite microstructure.

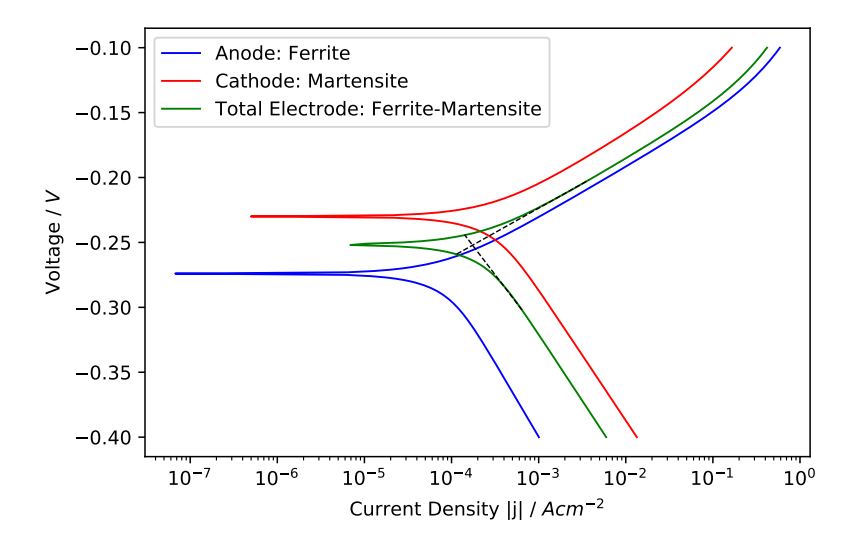


Figure C.6: Simulated potentiodynamic polarisation curve for the 60% ferrite 40% martensite microstructure.

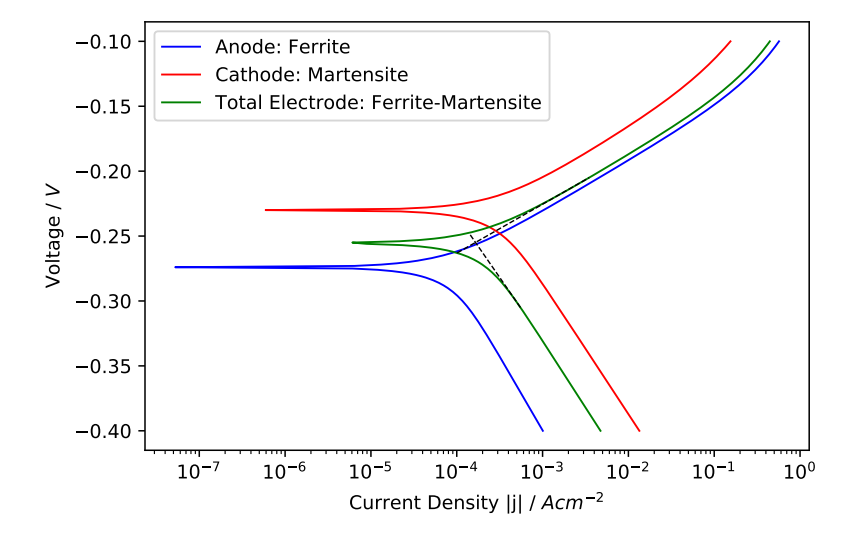


Figure C.7: Simulated potentiodynamic polarisation curve for the 70% ferrite 30% martensite microstructure.

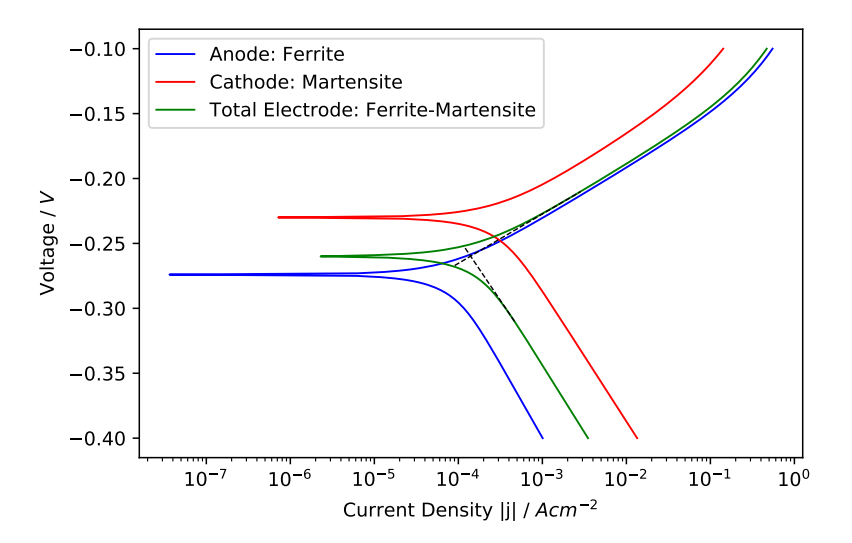


Figure C.8: Simulated potentiodynamic polarisation curve for the 80% ferrite 20% martensite microstructure.

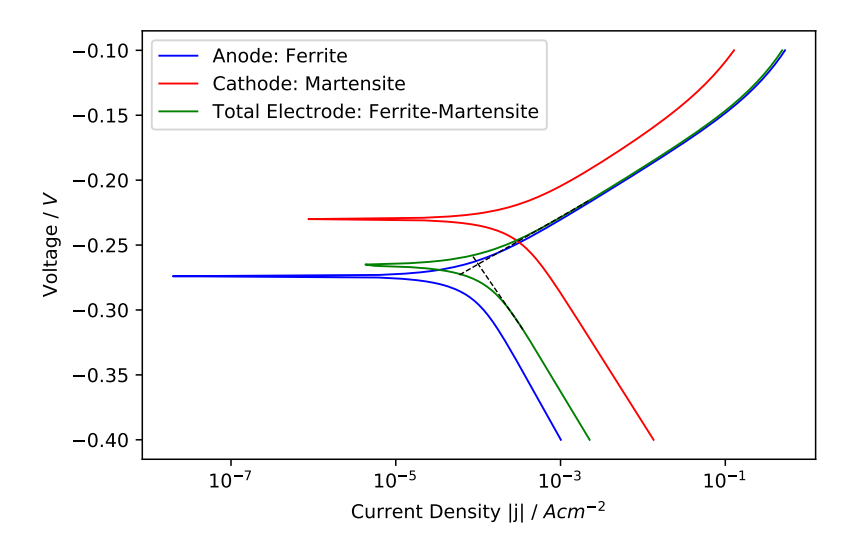


Figure C.9: Simulated potentiodynamic polarisation curve for the 90% ferrite 10% martensite microstructure.

C.2. Ferrite-Pearlite Microstructure Simulated Potentiodynamic Polarisation Plots

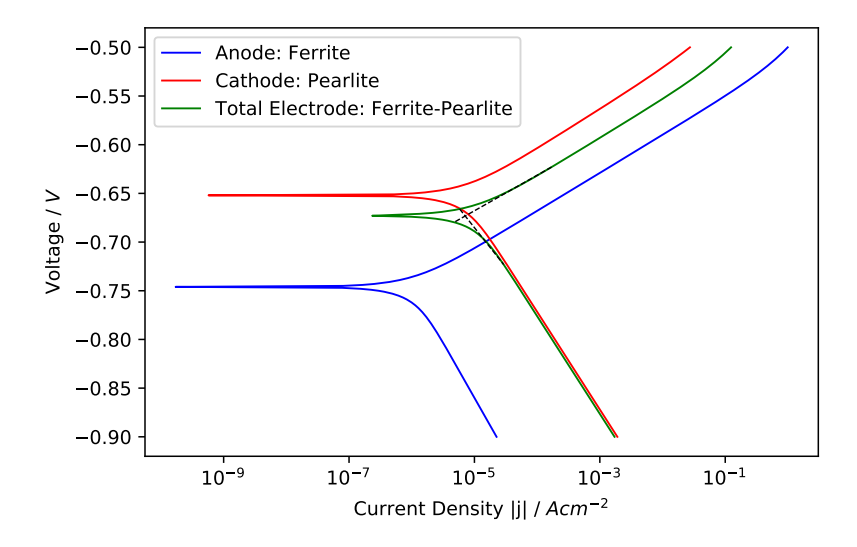


Figure C.10: Simulated potentiodynamic polarisation curve for the 10% ferrite 90% pearlite microstructure.

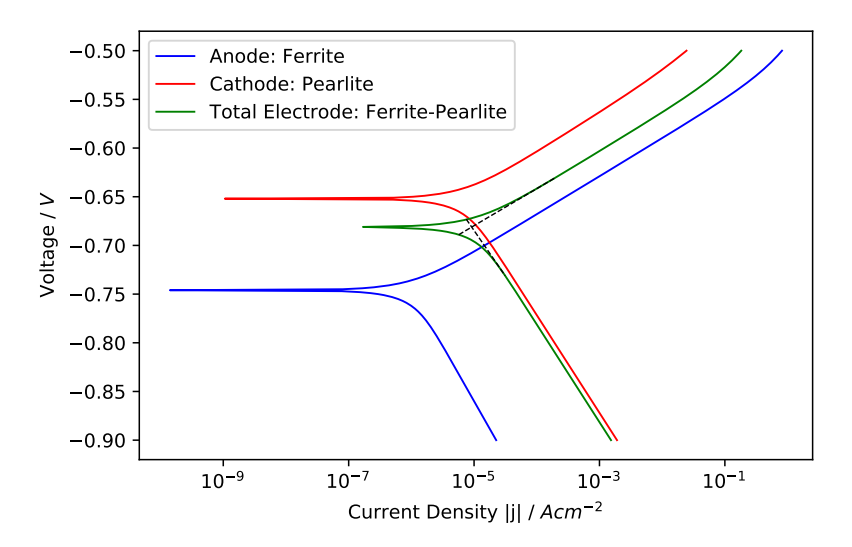


Figure C.11: Simulated potentiodynamic polarisation curve for the 20% ferrite 80% pearlite microstructure.

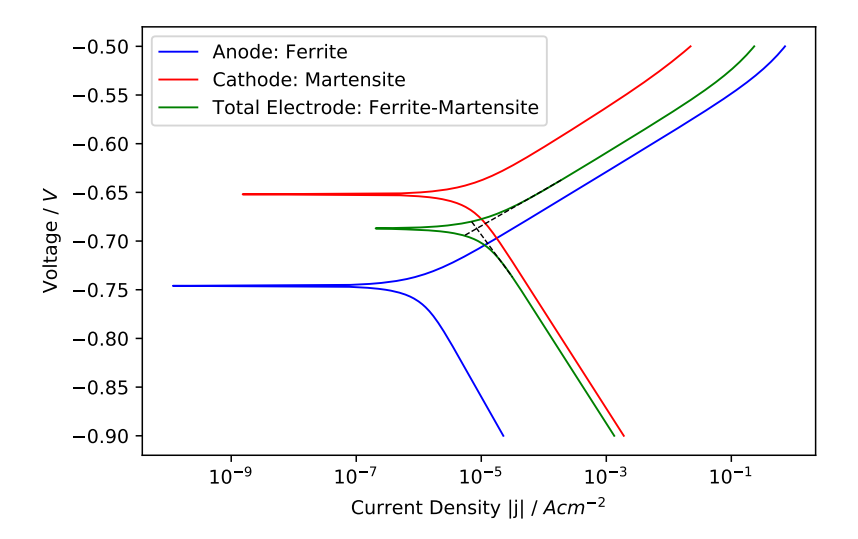


Figure C.12: Simulated potentiodynamic polarisation curve for the 30% ferrite 70% pearlite microstructure.

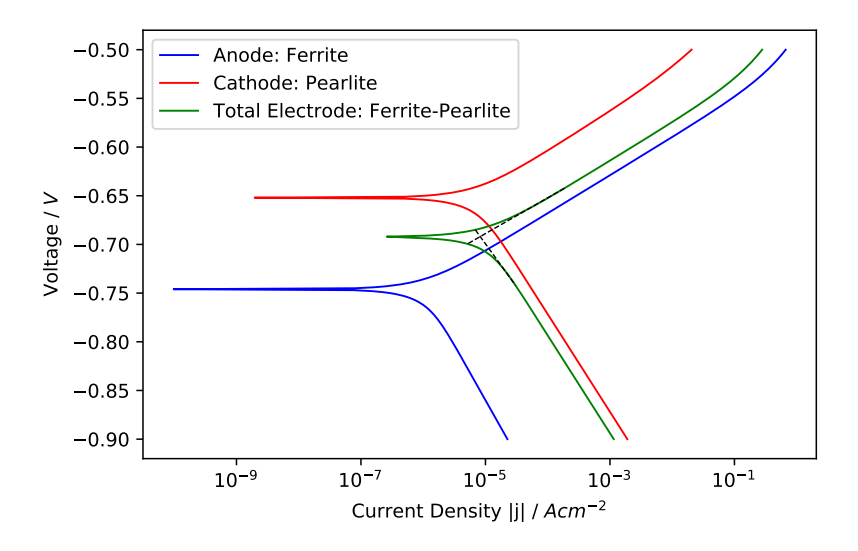


Figure C.13: Simulated potentiodynamic polarisation curve for the 40% ferrite 60% pearlite microstructure.

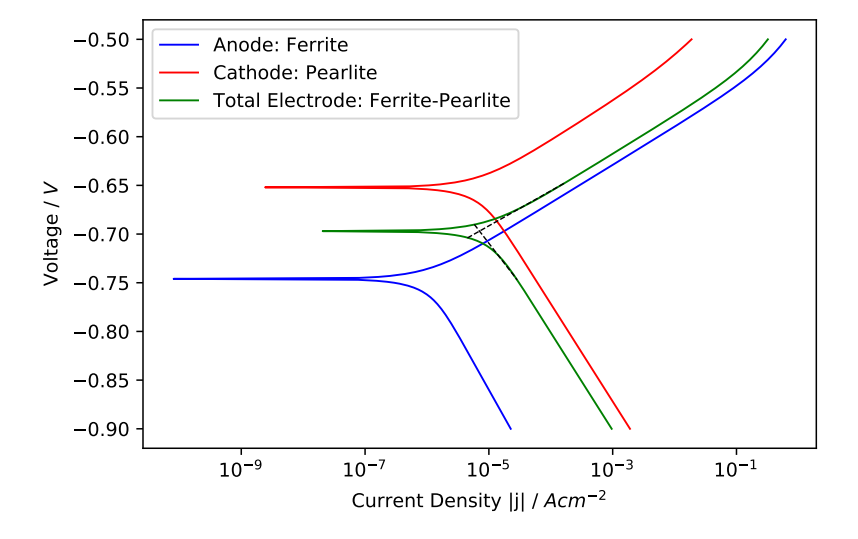


Figure C.14: Simulated potentiodynamic polarisation curve for the 50% ferrite 50% pearlite microstructure.

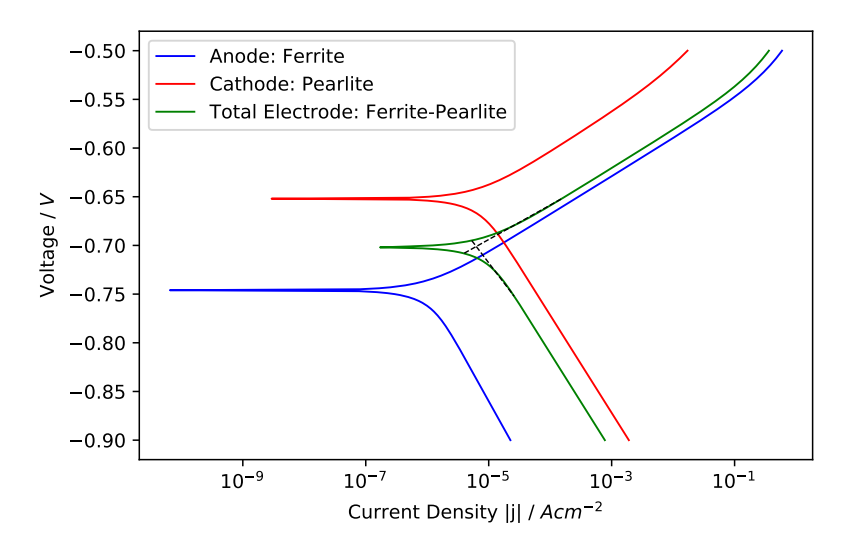


Figure C.15: Simulated potentiodynamic polarisation curve for the 60% ferrite 40% pearlite microstructure.

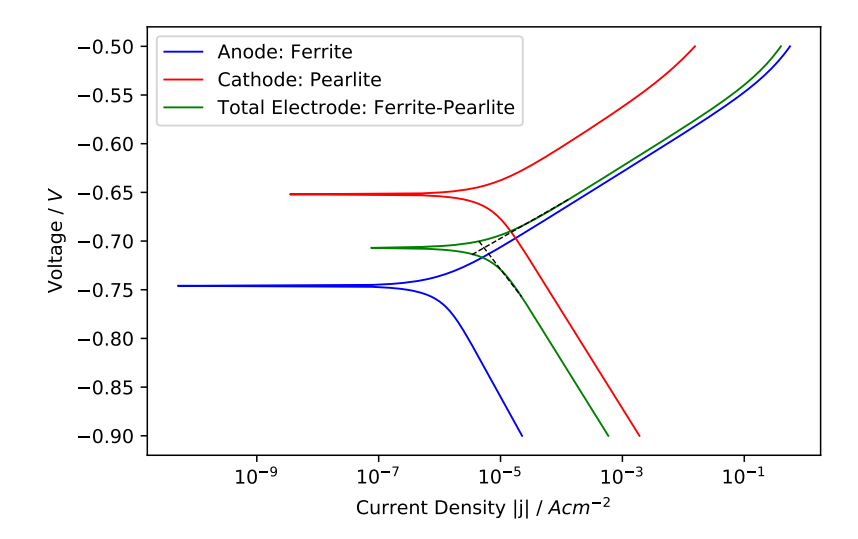


Figure C.16: Simulated potentiodynamic polarisation curve for the 70% ferrite 30% pearlite microstructure.

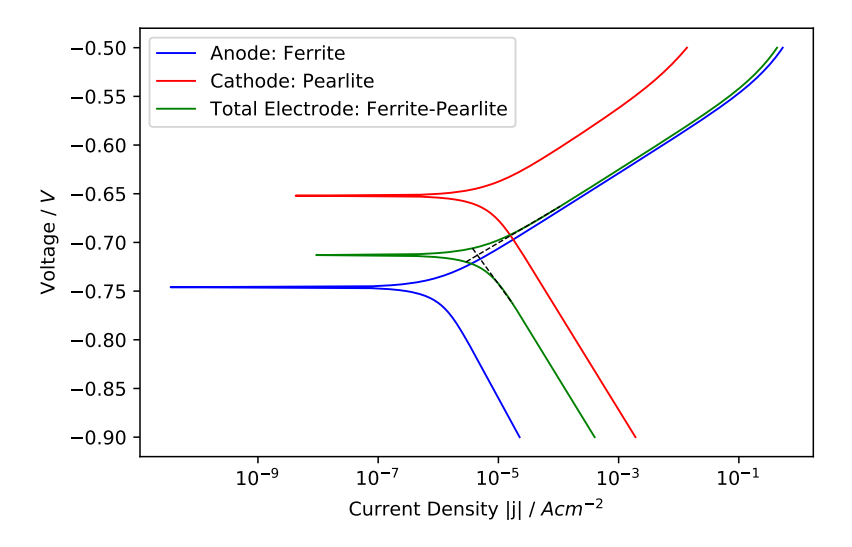


Figure C.17: Simulated potentiodynamic polarisation curve for the 80% ferrite 20% pearlite microstructure.

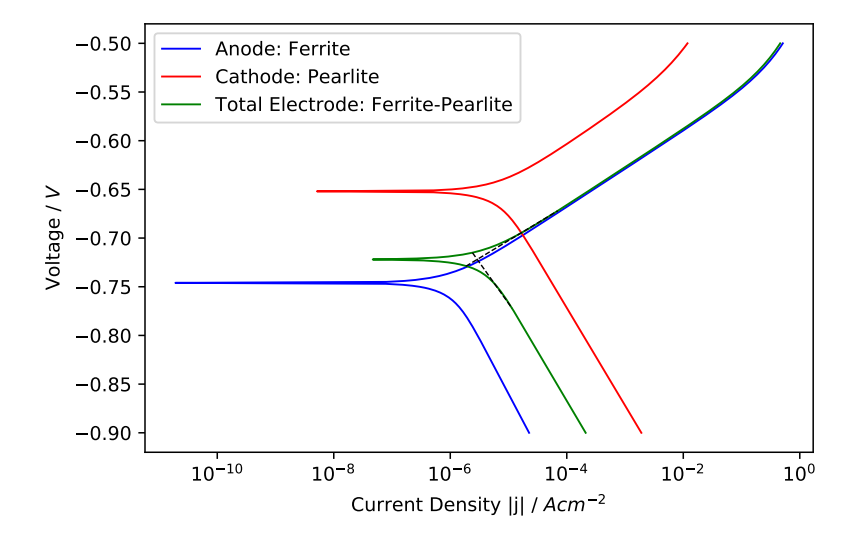


Figure C.18: Simulated potentiodynamic polarisation curve for the 90% ferrite 10% pearlite microstructure.